THESE

présentée à

L'UNIVERSITE DES SCIENCES ET TECHNOLOGIES DE LILLE

pour obtenir le titre de

DOCTEUR

Spécialité SCIENCES DES MATERIAUX

par

Stéphanie JUMEL

SUJET :

RPV-1 : A FIRST VIRTUAL REACTOR TO SIMULATE IRRADIATION EFFECTS IN LIGHT WATER REACTOR PRESSURE VESSEL STEELS

RPV-1 : UN PREMIER REACTEUR VIRTUEL POUR SIMULER LES EFFETS D'IRRADIATION DANS LES ACIERS DE CUVE DES REACTEURS A EAU LEGERE

Soutenue le 28 Janvier 2005 devant la commission d'examen

Professeur J. FOCT	Président
Professeur J.C. VAN DUYSEN	Directeur de thèse
Professeur G.R. ODETTE	Rapporteur
Professeur D.J. BACON	Rapporteur
Professeur M. PERLADO	Rapporteur
Professeur P.L. VIOLLET	Examinateur

TABLE OF CONTENTS

INTRODUCTION

Many key components in commercial nuclear reactors are subject to neutron irradiation which modifies their mechanical properties. So far, the prediction of the in-service behavior and lifetime of these components has required irradiations in so-called "Experimental Test Reactors". The use of these research facilities is becoming more and more problematic, in particular due to the decreasing number of reactors and post-irradiation characterization facilities, as well as significant constraints related to increasing costs and environmental safety regulations.

One way of partially mitigating these problems is to complement the empirical approach by developing tools for numerical simulation of irradiation effects in materials. The development of such tools, also called Virtual Test Reactors (VTRs), was made possible thanks to continuous progress in computer technology and physical understanding of irradiation damage. These tools are not meant to replace test reactors, but rather to complement them. For example, physically-based simulations could be used to:

- help guide the design and analysis of experimental irradiation programs;
- explore conditions outside the existing databases, such as very long time and high fluence, which are important for lifetime extension;
- systematically evaluate the individual and combined influence of the multitude of material variables (composition and microstructure) and irradiation service conditions (temperature, flux, spectrum, etc.) that may exceed the capacity of any practical test program;
- help design advanced materials for future fission and fusion reactors.

On the other hand, experimental test reactors are obviously necessary to calibrate numerical models and to perform the last qualification of industrial choices by validating numerical predictions.

It should also be mentioned that tools for numerical simulation of irradiation effects may represent a key added-value:

- in the global optimization of the nuclear industry's resources (analytical, irradiated materials testing, etc) necessary to study irradiation effects;
- for the training activities of young researchers and professionals in the nuclear field; a domain where knowledge management is becoming more and more crucial due to the retirement of the generation of nuclear engineers and scientists who participated to the building of reactors currently in service;
- to maintain operational a large amount of existing codes which tend to sink into oblivion;

- to contribute to reduce the production of radioactive samples, radioactive waste and radiation exposure of workers associated to irradiation programs.

The devising of VTRs started in the framework of the REVE Project (REactor for Virtual Experiments), launched by Electricité de France in 2000 (e.g. [1, 2, 3]) and relies on the huge previous effort in modeling (e.g. [4, 5]) and physically-based data correlations carried out by the RPV community (e.g. [6]). The REVE project is a joint effort between Europe, the United States and Japan aimed at building VTRs able to simulate irradiation effects in pressure vessel steels and internal structures of LWRs. The European team has already built a first VTR, called RPV-1, devised for pressure vessel steels. A part of the codes and data it uses, has been provided by the American and Japanese teams (led respectively by Professor G.R. Odette from University of California at Santa Barbara and Dr N. Soneda from the Central Research Institute of Electric Power Industry).

RPV-1 relies on many simplifications and approximations and has to be considered as a prototype aimed at clearing the way. Long-term efforts will be required to complete it and to build successive generations of more and more sophisticated versions. This improvement has been engaged in the framework of the PERFECT project supported by the European Commission (started in 2004). However, RPV-1 can already be used for many applications (understanding of experimental results, assessment of effects of material and irradiation conditions …). Its inputs and outputs are similar to those of experimental irradiation programs carried out to assess the in-service behavior of reactor pressure vessels.

To be as quantitative as possible, RPV-1 has to be able to simulate irradiation effects from the primary events resulting from the interactions between neutrons and atoms (displacement cascades), up to the assessment of the ensuing evolution of the steel mechanical properties. It therefore has to rely on a multi-scale approach ranging from the atomic level (nanometer and picosecond scales) up to the grain level (micrometer and year scales) and finally to the macroscopic level (centimeter and year scales), while retaining all the relevant information when linking successive levels. Such a complex simulation can only be done by modeling the involved physical phenomena, which requires simplifications and approximations. The main challenge of the work described hereafter was to simplify and approximate enough to succeed in the building of a first VTR, but not too much so as to keep a reasonable physical description of the involved phenomena. It has to be emphasized that the main objective was to build a first tool and to demonstrate its potentialities so as to initiate the development and use of improved versions.

The work carried out in the framework of the presented thesis was aimed at building RPV-1 It was made of two activities: a first activity consisted in developing the model used to simulate irradiation effects in RPV steels, defining the architecture of RPV-1, developing the

models required to build-up and parameterize two missing codes (INCAS and DUPAIR) and validating RPV-1. A second activity consisted in participating to the development of a rate theory code (MFVISC) with A. Ponçot (EDF), V. Duwig (EDF) and A. Barbu (Commissariat à l'Energie Atomique), to the programming of RPV-1 with C. Domain (EDF) and Y. Souffez (EDF), to the definition of an experimental validation program led by E. van Walle and L. Malerba (Centre d'Etudes Nucléaires de Mol) and to the setting up of the PERFECT proposal led by J.C. van-Duysen. Only the first activity of this work is presented in the present document.

The first chapter is dedicated to the description of the current knowledge on irradiation effects in RPV steels. This knowledge was used to determine the most important phenomena to be taken into account to simulate irradiation effects in RPV-1. The architecture of RPV-1, including the description of the codes and models it is made of, is provided in the second chapter. The third and fourth chapters give a precise description of the two missing codes INCAS and DUPAIR, with their parameterization and validation. Sensitivity studies as well as quantitative validations of RPV-1 are presented in the fifth chapter. Finally, two applications of RPV-1 are proposed in the sixth chapter so as to show the ability of VTRs to answer questions of interest to the "RPV community".

References

1 Jumel, S., Domain, C., Ruste, J., van Duysen, J.C., Becquart, C., Legris, A., Pareige, P., Barbu, A., Van Walle E., Chaouadi, R., Hou, M., Odette, G. R., Stoller, R. E., Wirth, B. D., ASTM-STP 1405, (2000).

2 Jumel, S., Domain, C., Ruste, J., van Duysen, J.C., Becquart, C., Legris, A., Pareige, P., Barbu, A., Van Walle, E., Chaouadi, R., Hou, M., Odette, G.R., Stoller, R., Wirth, B.D., Journal of Testing and Evaluation, vol. 30, (2002), p. 37.

3 Malerba, L., Van Walle, E., Domain, C., Jumel, S., van Duysen, J.C., Proceedings of ICONE-10: 10th International Conference on Nuclear Engineering, Arlington, USA, (2002).

4 Odette, G.R., Scripta Metallurgica, vol. 11, (1983), p. 1183.

5 Lucas, G., E., Odette, G. R., Lombrozo, P. M., J. W., Sheckherd, ASTM-STP 870, (1985), p. 900.

6 Eason, E. D., Wrigth, J. E., Odette, G. R., "Improved Corrrelations for Reactor Pressure Steels, NUREG/CR-6551, (1998).

CHAPTER I

Literature survey on irradiation effects in Light Water Reactors pressure vessel steels

The literature survey given in this chapter was extracted from a larger document under publication by the International Atomic Energy Agency [1].

Vessels of Light Water Reactors (LWRs) are made of low-alloyed ferritic steels. During operation, these steels experience neutron irradiation which may produce changes in their mechanical properties. Thanks to many experimental programs, such changes could be anticipated, quantified and taken into account in the design and definition of operating conditions of the reactors currently in service. They are now systematically followed-up by Pressure Vessel Surveillance Programs (e.g. [2]), which validate the forecasts in most of the cases.

In parallel to this mechanical testing approach, a large effort was made in many countries to characterize the irradiation-induced damage in RPV steels (e.g. [3, 4, 5, 6, 7]) as well as to understand and model the mechanisms governing this damage (e.g. [8, 9, 10, 11]). The obtained results were used to successfully support forecasts of in-service steel behavior on a physical basis (e.g. US-NRC regulatory Guide 1.99, revision 2 [12]); they can now be used to build numerical tools aimed at simulating irradiation effects (e.g. [13, 14]).

The aim of the present chapter is to describe the current knowledge on irradiation-induced damage in Western-type RPV steels (nature of defects, involved mechanisms,…). In this field, ideas have evolved a lot with the passing years and many interpretations, mechanisms, models,… have been put forward to explain experimental data. An extended revue of these ideas is given in [1], here the current understanding is provided.

In Paragraph I, some information on RPV steels and their in-service conditions are reminded. Paragraph II provides experimental results concerning the influence of steel chemistry and microstructure as well as irradiation conditions on the irradiation-induced evolution of mechanical properties. Paragraph III is dedicated to the description of the irradiation-induced defects.

Chemical compositions are expressed in weight percent (% or wt%), except in some cases for which the atomic concentration was used (at %).

I - Reactor Pressure Vessels

1.1 - Pressure vessel steels

Vessels of current Western-type Light Water Reactors (LWRs) were built with welded plates or shells made of high toughness quenched and tempered low-alloyed ferritic steels (e.g. [15]). During the vessel manufacturing, base metals and welds underwent several stress-relief heat treatments (T ≈ 550 – 610°C) which have fashioned their microstructure (carbides, chemical content of solid solution,…).

Base metals: most of the base metals are low-alloyed NiMnMo ferritic steels, typically A533B Class 1 and its forging equivalent A508 Class 3 (corresponding to 16MND5 French standard). A typical chemical composition specification is given in Table I.

A533B and A508-type steels have a tempered bainitic structure in which prior austenitic grains have a size of about 30 µm. Transmission Electron Microscopy observations reveal (Figure 1) that the bainitic grains contain a pretty high density of dislocations, mostly organized in sub-boundaries and small $(Fe,Mn)_3C$ and $(Fe,Mo)_2C$-type carbides (≈ 40 to 500 nm) (e.g. [16, 17]). The typical width of the bainitic laths is about 1-2 µm.

Welded joints: a typical example of chemical composition of welded joint is given in Table I [2]. It is noteworthy that the carbon content is lower than in base metal. In general, welded joints have a bainito-martensite structure with a very fine carbide distribution.

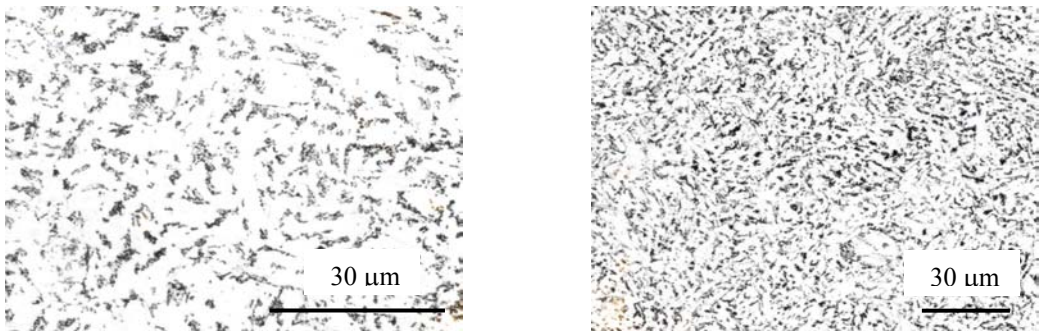

Figure 1: light optical micrographs - typical structure of a A508B - Class 3 steel [18].

Table I: examples of specification for some LWR pressure vessel steels (RCC-MR: Règles de Conception et de Construction des matériels mécaniques des îlots nucléaires. Tome Matériaux)

	Alloying elements						Residual elements			
	C	Mn	Mo	Ni	Cr	Si	P	Cu	V	S
16 MND5	≤ 0.22	1.15-1.60	0.43-0.57	0.50-0.80	≤ 0.25	0.10-0.30	≤ 0.008	≤ 0.08	≤ 0.01	≤ 0.008
Welding	≤ 0.1	0.80-1.80	0.35-0.65	≤ 1.20	≤ 0.30	0.15-0.60	≤ 0.010	≤ 0.07	≤ 0.022	≤ 0.025

1.2 - In-service conditions

Most of the Western-type reactor pressure vessels operate at temperatures ranging from about 270 to 330°C. They are subject to neutron irradiation, with the peak located at the core mid-plane (beltline region).

A typical neutron spectrum on the inner surface of a LWR vessel is given in Figure 2, almost all the neutron have an energy lower than 3 MeV. The total number of neutrons with an energy higher than 1 MeV received per time unit (so-called the neutron flux) at the peak location is typically around 10^{10} n.cm^{-2}.s^{-1} (Cf § 2.3). Such a flux leads to a fluence of some 10^{19} n.cm^{-2} and a dose of some hundredths of dpa for 32 years full power operation (for typical French LWRs, flux of about 6 10^{10} n.cm^{-2} s^{-1}, fluence of about 6 10^{19} n.cm^{-2} and dose of about 0.1 dpa). Such values are rather low compared to what is experienced by other reactor components (e.g. typical flux on internal structures is about 6 10^{13} n.cm^{-2}.s^{-1}). However, they are high enough for the irradiation to induce changes in the properties of ferritic steels.

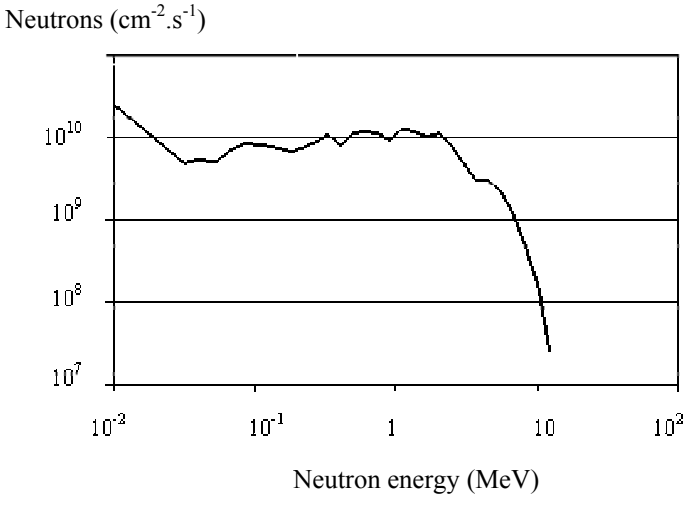

Figure 2: typical neutron spectrum on the inner surface of a LWR vessel.

II - Irradiation effects in RPV steels

2.1 - Effects on mechanical properties

Irradiation introduces changes in the mechanical properties of RPV steels (e.g. [19, 20, 21]). Typically, increase of tensile yield stress (Figure 3), ultimate strength, hardness and Ductile Brittle Transition Temperature (DBTT) (e.g. [22]) as well as decrease of ductility and toughness (e.g. [23, 24, 25]) are observed. Irradiation reduces also strain ageing sensitivity (e.g. [26]) and internal friction peaks of RPV steels (e.g. [27, 28, 29]).

For some properties, empirical correlations were established; the most commonly used are :

- $\Delta R_{P0.2} \approx 3.4\ \Delta Hv$ [30]
- $\Delta DBTT \approx 0.68\ \Delta R_{P0.2}$ (at 20°C, without intergranular rupture) [31]
- $\Delta DBTT \approx \Delta K_{IC}$ [32]
- $\Delta R_m \approx \Delta R_{P0.2}$ [33]

where $\Delta R_{P0.2}$, ΔR_m, ΔHv , $\Delta DBTT$, ΔK_{IC} are respectively the increase of yield stress, ultimate strength, hardness, Charpy DBTT and stress intensity factor.

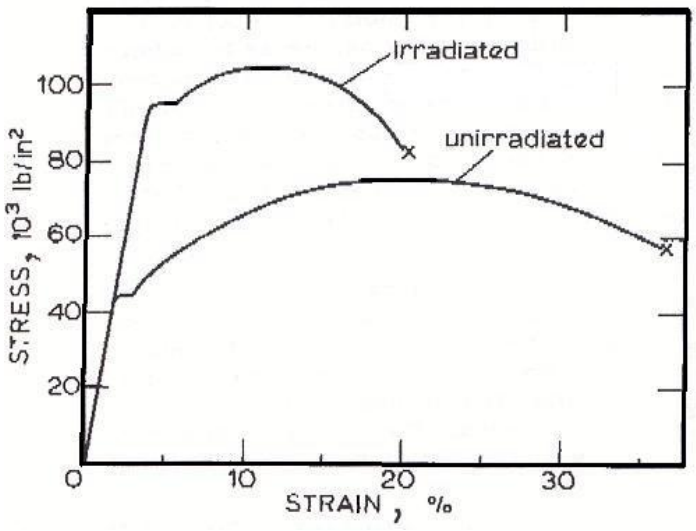

Figure 3: evolution of a stress-strain curve after irradiation to 9.5 10^{18} n.cm^{-2} (E>1MeV) at 300°C [34].

2.2 - Influence of RPV steel parameters

Significant variations in embrittlement response between different types of steel, different heats of the same steel and different forms of steel (plate, weld and Heat Affected Zone) were observed for the first time at the end of the 60's (e.g. [35, 36]). This has suggested effects of chemical composition and structure on irradiation embrittlement sensitivity of RPV steels (e.g. [37, 38, 39, 40]). Since then, many studies have been carried out to assess these effects. Their main results are summarized in this paragraph, complementary information can be found for example in references [1, 7, 8, 41].

a) Chemical composition

Impurities: effects of impurities on the sensitivity of RPV steels to irradiation embrittlement were shown experimentally for the first time in 1967 (Figure 4) on a laboratory A302-B heat [37, 38, 39], confirmed on commercial A333-B heats in 1970 [40] and then extensively studied until the mid 90s. Analysis of the produced results has to be based on the concentrations of impurities in solid solution. These concentrations may indeed largely differ from nominal ones since such elements can intensively precipitate or segregate during the steel making or heat treatments prior to irradiation. As an example, in welds with nominal copper content of about 0.2 at%, Miller and al. [42, 43, 44] measured bulk copper levels of about 0.14 at% in as-received conditions (stress-relief heat treatment at about 600°C); similar results are also available for nitrogen [29]. The solubility limit of each element depends on the whole chemistry of the steel; as first approximation, Table II gives some examples in pure iron at 575°C and 290°C.

- Copper is one of the elements which have the most deleterious effect on the irradiation-induced embrittlement of RPV steels (e.g. [40]). This effect appears from a copper content of about 0.04% (e.g. [45]) and becomes very strong above 0.1% [46]. Available experimental databases exhibit a pretty high variability in the DBTT copper dependence; this dependence seems to be of the order of some hundreds of °C per %Cu. From the 70s, the total copper content in RPV steels and their welds has been limited to a maximal value of 0.1%, and then, even to lower values, in most of the Western countries (e.g. 0.07% in France).

  Copper contents in recent RPV steels are lower than the solubility limit of this element in iron at the temperature of stress-relief heat treatment (≈ 0.17% in pure iron) (e.g. [47, 48, 49]). Thus, it can be expected that in such steels a large part of copper atoms is in solid solution when the vessel is commissioned (a part may have precipitated during the cooling following the last stress-relief treatment). As the copper solubility limit at the irradiation temperature is very low (≈

0.007% in pure iron [48]), copper atoms tend to form precipitates or clusters in RPV steels in operation.

• Phosphorus has a well known deleterious effect on thermal ageing of ferritic steels due to its propensity to intergranular segregation [38, 50, 51, 52, 53, 54, 55]. Experimental programs showed that for concentrations higher than about 0.015%, the irradiation-induced shift of the Charpy transition curve was also strongly reinforced as the phosphorus content increased. No clear effect on hardness and yield stress was reported (e.g. [56]). However, it was suggested that the phosphorus effect could decrease with increasing copper content [57]; this trend has not been clearly confirmed subsequently.

From the beginning of the 70's, the phosphorus concentration in RPV steels and their welds has been limited to a maximum value of 0.015%, and then even lower values (e.g. 0.008% in France), in most of the Western countries. Such contents are much lower than the solubility limits of this element in iron at the temperatures of stress-relief heat treatment (> 0.27% in pure iron [10, 47]) and irradiation [10]. Thus, it can be expected that in RPV steels a large part of phosphorus atoms is in solid solution when the vessel is commissioned and that these atoms have a low tendency to precipitate or cluster in operation. However, they may segregate into grain boundaries (which reduces the solubility limit to negligible level) and weaken them.

• Nitrogen : several studies showed that nitrogen has a low influence on the irradiation sensitivity of RPV steels at temperature higher than 250°C (Figure 5). At lower temperature, it may have a major influence [8, 27, 29, 58].

The free nitrogen content is negligible in aluminum grain size controlled steels [29], and seems to be around some tens of ppm (20-30 ppm) in Si-killed steels [27], which is much lower than nitrogen solubility limit in iron at the operation conditions (≈ 400 ppm [10]). It can be considered that nitrogen has a low propensity to precipitate or cluster in service conditions.

• Tin and arsenic: it was found that tin makes a small contribution to irradiation embrittlement of RPV steels [59]. The same result was obtained for arsenic in the range of contents extending from 42 to 480 ppm [59].

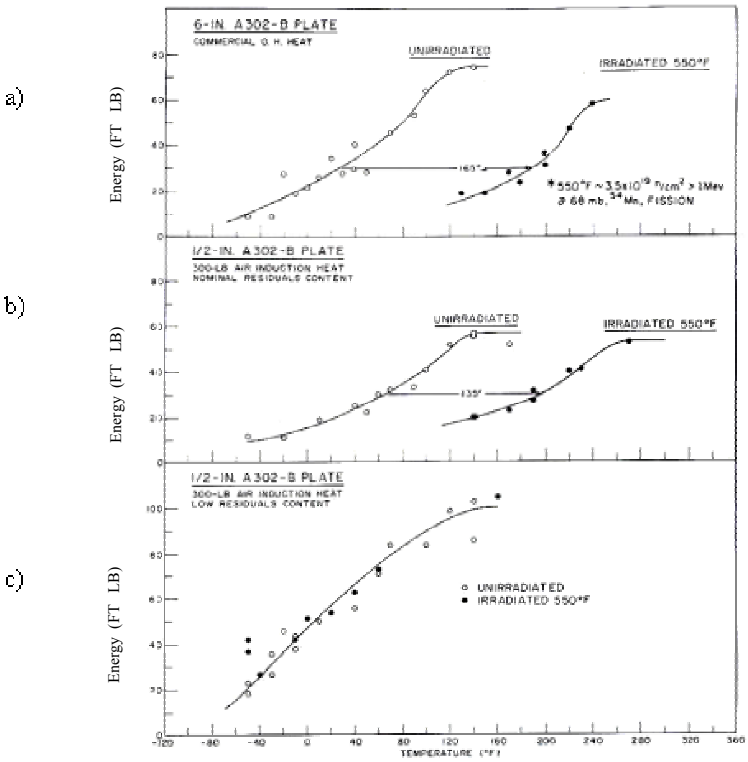

Figure 4: comparison of irradiation embrittlement sensitivities at about 288°C (as measured by changes in the Charpy-V notch DBTT) of a large commercial heat (a) and two air induction heats of A302-B steels with nominal (b) and residual low elements (c) [39]; fluence ≈ 3.5 10^{19} n.cm^{-2} (E > 1MeV).

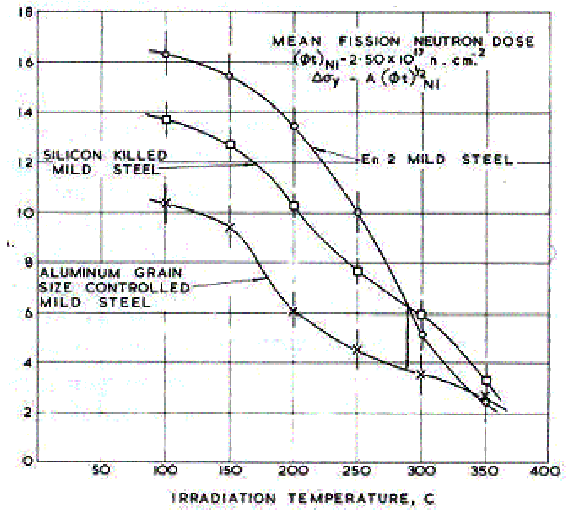

Figure 5: effect of nitrogen in irradiation-induced embrittlement of RPV steels [58].

Alloying atoms: alloying atoms have also been targeted by research programs to characterize their effect on irradiation-induced embrittlement of RPV steels. Most of the efforts were focused on Ni, some ideas were also put forward for Mn.

• Nickel effect has been extensively studied since the beginning of the 80s. This element has a strong, and so far not fully explained, deleterious impact on irradiation-induced embrittlement of RPV steels (e.g. [23, 60, 61, 62, 63, 64, 65]). This impact may become very high for nickel contents higher than about 1 or 1.2% and increases with the copper content in a synergetic way. However, it was also reported that 3.3% Ni steels do not show enhanced irradiation-induced embrittlement compared to low Ni steels [64].

Nickel contents in RPV steels were expected to be lower than the solubility limits of this element at temperatures of stress-relief heat treatment and irradiation (respectively about 5.4% and 4.2% in pure iron). However, experimental and thermodynamic studies [66, 67] have shown that, in operation, nickel can integrate copper-rich defects in RPV steels. In addition, the thermodynamics approach reveals that nickel could also participate in nickel manganese-rich phases containing a small amount of copper (late blooming phases [66]). Theses phases are assumed to be promoted by high nickel and manganese contents, high fluences as well as by low copper content and low temperature. Their kinetics of precipitation is supposed to be controlled by the nucleation rate (copper is believed to be needed to catalyze the nucleation). The presence of late blooming phases was recently proven by experimental analysis [68].

• Manganese has not been yet the subject of dedicated experimental study. Consequently, its impact on the irradiation-induced embrittlement is not well known.

Manganese contents in RPV steels were expected to be lower than the solubility limits of this element at temperatures of stress-relief heat treatment and irradiation (respectively about 2.8% and 3% in pure iron). However, as mentioned above, thermodynamics and experimental studies have shown that in operation manganese can integrate copper rich precipitates. It may also participate in Ni-Mn-rich late blooming phases [66, 69].

Table II : solubility limits of some chemical elements in α iron.

	Cu	P	N	Mn	Ni
At 575°C (wt%)	≈ 0.17*	≈ 0.27*	≈ 0.12*	≈ 2.8*	≈ 5.4*
At 290°C (wt%)	≈ 0.007**	≈ 0.05***	≈ 0.04***	≈ 3*	≈ 4.2*

* [47], ** [48], *** [10]

b) Metallurgical structure

In principle, the structure (grain size, density of carbides, density of dislocations, ..) does play a role in RPV steel irradiation response by setting the types and quantities of sinks for point defects. It also influences the hardening by superposing the effect of pre-existing carbides to that of the irradiation-induced defects [66].

Some experimental studies were performed to quantify these roles. In particular, Vacek [70] carried out a comprehensive study on this topic. By appropriate heat treatments, he prepared products with different structures from the same heat, and irradiated them at 285 ± 10°C with a fluence of about 7.3 10^{19} n.cm^{-2} (E > 1 MeV). He reported that the irradiation-induced hardening and embrittlement are almost independent of the structure.

Some statistical analysis of experimental results lead to the separation of weld and base metal behaviors (e.g. [71, 72]) and even the ones of welds, plates and forgings [73]. For given irradiation conditions and chemical composition, regressions forecast that the embrittlement of welds and plates are similar and slightly higher than that of forgings. However, the differences of behavior are small, which confirms that the structure has not a major effect on the irradiation response of RPV steels.

2.3 - Irradiation parameters

Temperature: temperature has a strong influence on irradiation embrittlement of RPV steels, the level of embrittlement being reduced by increasing temperature. Some results showed that this influence depends on the steel chemistry (Figure 6) and irradiation conditions (e.g. [74]). In the ranges of temperature, fluence and chemical composition of interest for LWRs, the shift of DBTT and increase of yield stress are around 1.0 ± 0.6 °C/°C and 1.5 ± 1.0 MPa/°C respectively [33, 74, 75, 76, 77]. As a rule of thumb, values of 1°C and 1.5 MPa per degree Celsius are commonly used.

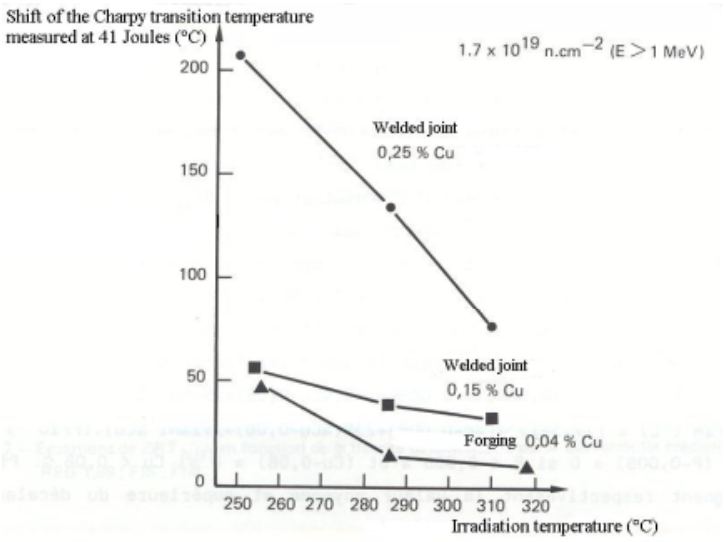

Figure 6: effect of irradiation temperature on Charpy V-notch DBTT shift [74].

Spectrum: several experiments (e.g. [78, 79, 55, 80, 81]) were performed to assess the spectrum effect on RPV steel embrittlement. A recent study (French ESTEREL program [79]) was carried out with an extreme care to compare the effects of two neutron spectra on the embrittlement of a medium and a low irradiation-sensitivity steel. No significant spectrum effect has been revealed (this program is presented in details in Chapter VI).

Irradiations carried out in reactors with very different spectra from those of LWRs showed that thermal neutrons may have a significant effect on embrittlement as soon as the ratio thermal to fast neutron fluxes is higher than 10: i.e. $\frac{\Phi_{th}}{\Phi_f} \geq 10$ [82, 83, 84]. Thermal neutrons induce atomic displacements from their collisions with atoms but also from lower energy recoils (of about 500 eV) associated with the Fe^{56} (n, γ) reaction and from the B^{10} (n, α) reaction producing Li^7 and He^4 transmutation products with energies 0.87 MeV and 1.53 MeV respectively. For strongly thermalised neutron spectra, the determination of the irradiation dose may require to take into account the three contributions: $dpa = dpa_{NRT} + dpa_{Fe}^{56}(n, \gamma) + dpa_{B}^{10}(n, \alpha)$ [85, 86, 87].

Flux: many experiments were carried out to assess the flux effect on irradiation-induced embrittlement of RPV steels (e.g. [5, 88, 89, 90]). However, the interpretation of available data is not straightforward due to a large variety of experimental conditions (ranges of flux, chemical composition, ….). At the end of the 70s, Petrequin and al. proposed a sketch of flux effects (Figure 7) summarizing French experimental results [19, 88]. More recently, EPRI-CRIEPI gathered experts for a workshop aimed at analyzing and synthesizing the main

results available at the international scale [91]. For steels containing a low level of copper (Cu lower than about 0.1%), it was concluded that for irradiation temperatures between 150 and 300°C, there is no significant flux effect in a range of flux below a threshold value (about 10^{12} $n.cm^{-2}.s^{-1}$ E> 1MeV at 290°C).

Fluence: optimum regressions fitted to a wide body of experimental data suggest that irradiation embrittlement increases with increasing neutron fluence according to a law of the form: $(fluence)^n$. Most of the proposed values for the exponent n range from 0.3 to 0.5 (e.g. [21, 92, 93, 94]).

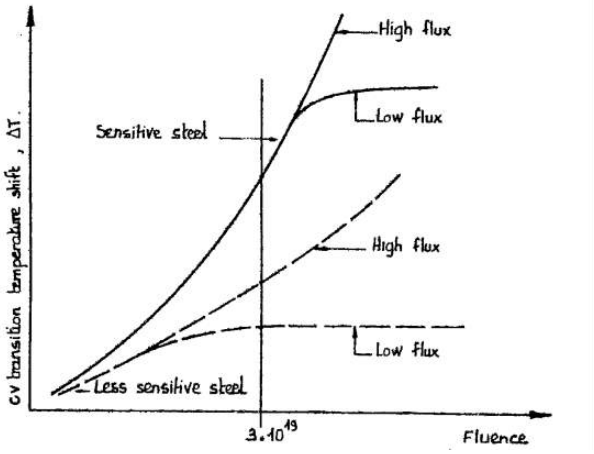

Figure 7: sketch of the flux effect from French experimental results [19, 88].

2.4 - Characterization of irradiation-induced defects

Since the first microstructural studies on irradiated low-alloyed ferritic steels in the early 70s (e.g. [95, 96]), a huge effort has been devoted to characterize the irradiation-induced damage in LWR pressure vessel steels (e.g. [4, 5, 6]).

This effort showed that neutron irradiation induces the formation of, at least, four types of hardening defects in RPV steels:

- copper-rich precipitates also containing Mn, Ni and Si;
- vacancy-solute atoms (Cu, Mn, Ni, Si) clusters;
- self-interstitial atom clusters (SIA clusters) and dislocation loops (SIA loops);
- vacancy clusters.

Experimental studies showed that the presence of copper is required for the formation of precipitates and vacancy-solute clusters (e.g. [66, 69, 97, 108]). It was also

noticed that some of the hardening defects are unstable (i.e. they have a lifetime [48, 98]) at the RPV irradiation temperature (about 290°C). They exist with a high number density thanks to a dynamical equilibrium state imposed by the irradiation.

- **Copper rich precipitates**: copper-rich precipitates were revealed by several techniques (HREM[1], STEM[2], AP[3]) in irradiated high copper iron based alloys. In particular Tomographic Atom Probe experiments [99] carried out on binary alloys (Fe-0.7%Cu, Fe-1.4%Cu) irradiated with electrons or neutrons at about 288°C gave a rather precise description of the morphology of irradiation-induced "pure" copper precipitates in iron at this temperature. Such precipitates can be described as a core zone, with a diameter of about 1nm, containing about 80% of copper (thus 20% of iron) and surrounded by a diffuse interface with the matrix.

The existence of copper-rich precipitate was also proven by combinations of several characterization techniques (SANS[4], EXAFS[5],…) in low copper iron based alloys [100]. In RPV steels, their number density range is about 10^{24} m^{-3} for a fluence of some 10^{19} $n.cm^{-2}$. Thermodynamics-based calculations or numerical simulations showed that they should contain Mn, Ni and Si [66, 67]. There are also some experimental (e.g. [99]) or modeling [101] evidences showing these three elements mainly concentrate at their interface with the matrix.

- **Vacancy-solute clusters**: solute atom clusters were clearly revealed by AP studies (e.g. [102, 103, 104]). They are composed of Cu, Mn, Ni, Si and Fe atoms (Figure 8 a). The threshold irradiation dose from which these defects are detected seems to decrease as the steel copper content increases (Figure 9). Whatever the fluence and steel chemical composition, their radius is about 1.5 nm and they mainly contain iron atoms (about 85%). Composition profiles revealed that the manganese, nickel and silicon atoms seem to concentrate at the interface with the matrix [67, 103]; their spatial extends are generally slightly larger than that of copper enrichment (Figure 8b). Due to their low concentration in solute atoms [1], the solute atoms clusters are often called "atmospheres" or "clouds" [102]. The reason why such defects keep a dilute morphology and do not collapse in real precipitates is an issue which is still under discussion. A possible explanation may be the presence of a high concentration of vacancies within the defects. This explanation is supported by numerical simulation. Indeed, Domain [105] simulated the growth of vacancy-copper clusters using Monte Carlo simulation methods. The irradiation was reproduced in the simulation by introducing a constant flux of vacancies and SIAs in the material. The simulation leads to the

[1] **H**igh **R**esolution **E**lectron **M**icroscopy
[2] **S**canning **T**ransmission **E**lectron **M**icroscopy
[3] **A**tom **P**robe
[4] **S**mall **A**ngle **N**eutron **S**cattering
[5] **E**xtended **X**-ray **A**bsorption **F**ine **S**tructure

growth of a 3-D vacancy-copper cluster (Figure 10) containing similar numbers of vacancies and copper atoms. Due to the presence of vacancies, copper atoms do not form a single compact precipitate. The expected presence of vacancies in the solute atoms clusters is at the origin of their name: copper-vacancy clusters. The existence of such defects was first suggested by Odette [106].

Experimental and simulation studies showed that, among the solute atoms in the clusters or precipitates, copper invariably has the highest enrichment factor over the matrix level. That explains the significant depletion of the copper content measured in the matrix; this content tends to a lower limit of about 0.03 - 0.04 % (e.g. [48]). For steels with a copper content of about 0.1 - 0.15 %, this limit is reached at a fluence of about 2 10^{19} n.cm^{-2}. No significant depletion was measured for Ni, Mn and Si in the matrix.

The number density of vacancy-solute clusters increases with the copper and nickel contents of the steel as well as with the fluence. As an example, number densities of 3.3, 5.7 and 9 10^{17} cm^{-3} were measured with an Atom Probe in a 0.08% Cu steel irradiated at 275°C with fluences of 2.5, 6.6 and 12 10^{19} n.cm^{-2} (E > 1MeV), respectively (see a review in [1]).

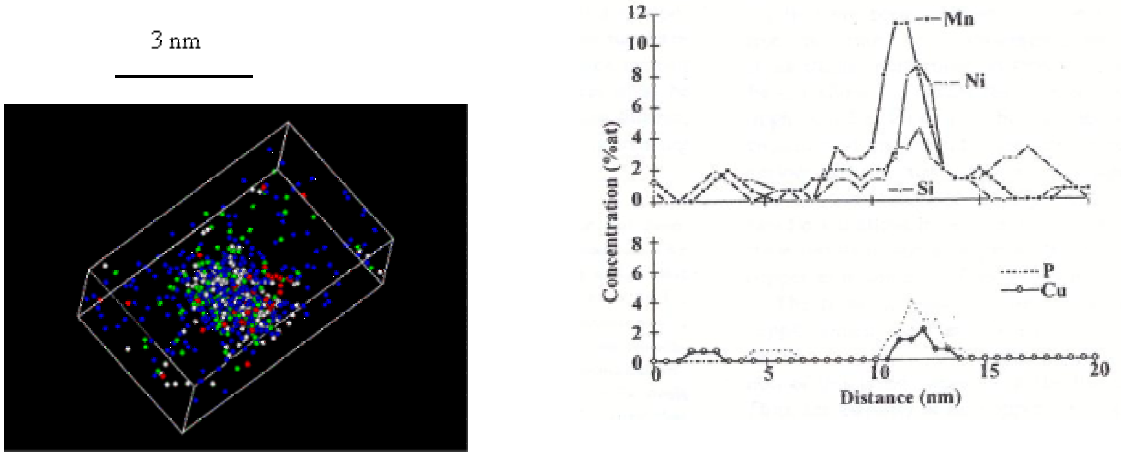

Figure 8: AP analyses of neutron-irradiated alloys [109]

a) solute atom cluster observed in a RPV steel (red: Cu, blue: Mn, white: Mn and green: Si);

b) composition profiles across an irradiation-induced solute atom cluster in an RPV steel.

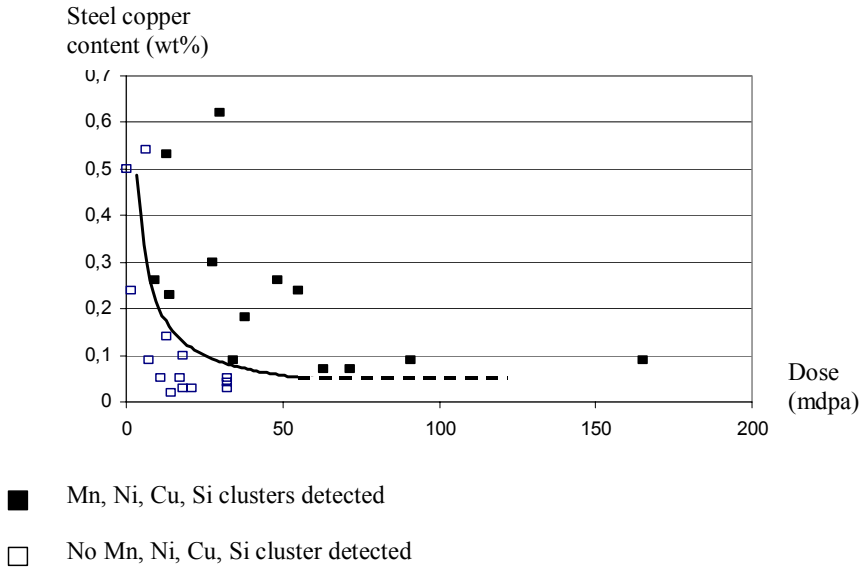

Figure 9: steel copper contents and doses for which Mn-Ni-Cu-Si clusters (clusters or precipitates or both) have been detected by AP in irradiated RPV steels [5, 48, 102, 107, 108, 109, 110, 111, 112].

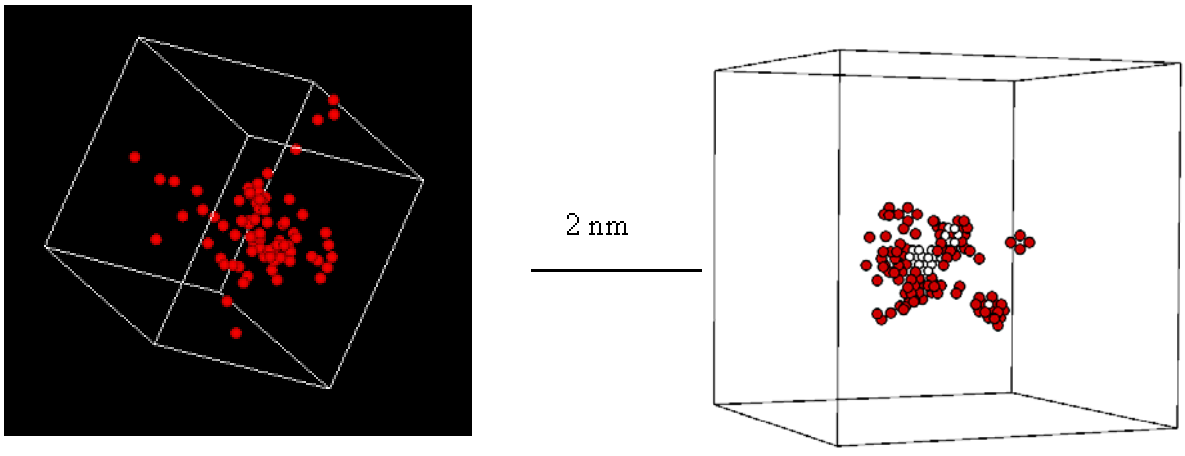

Figure 10: 3D vacancy-copper cluster.

a) observed by AP in a neutron-irradiated Fe-0.1%Cu alloy;

b) obtained by combining OKMC and LKMC in Fe-0.2% Cu (black spheres : copper atoms, white spheres : vacancies) [113].

- **SIA clusters and dislocation loops**: loops are generally not observed experimentally in RPV steels irradiated in nominal conditions (T ≈ 300°C) (e.g. [16]). However, they were revealed in ferritic alloys (Fe, Fe-Cu, RPV steels,…) irradiated with conditions different from those of LWRs: e.g. higher neutron flux or fluence (e.g. [96]), lower irradiation temperature, electron (e.g. [114]) or ion (e.g. [115]) irradiations.

The structures of SIA clusters and dislocation loops are not completely understood yet. In particular, the set of properties that distinguishes both types of defects is not well clarified [116, 117, 118, 119]. According to Puigvi et al., and Kuramoto [116, 118], about 160 or 200 SIAs are required for a cluster to behave fully as a dislocation loop. Wirth et al. [e.g. 117] estimate that, except at very small size, both types of defects have analogous properties and can be considered similar. In the rest of the document, we will retain this position assimilating SIA clusters to dislocation loops. The term "loop" and "cluster" will be equally used , but we will try to use the term "loop" for clusters with more than four SIAs.

TEM examinations of ferritic alloys irradiated with high doses (≥ 1 dpa) (e.g. [120, 121]) as well as numerical simulations (e.g. [117, 122, 123,124]) showed that the stable SIA loops have for Burgers vector b = $\frac{1}{2}\langle 111\rangle$ or $\langle 100\rangle$. Wirth et al [117] described the $\frac{1}{2}\langle 111\rangle$ loops as a mixture of $\langle 111\rangle$ dumbbells and crowdions on $\{110\}$ planes, Soneda [122] and Osetsky [124] saw only the crowdions. Osetsky described the $\langle 100\rangle$ loops as a set of $\langle 100\rangle$ crowdions.

Simulation studies showed that SIAs, SIA clusters and small SIA loops are mobile along <111> directions (e.g. [122, 124, 125, 126, 127, 128]). They may switch their moving from a <111> direction to another one either by thermal activation or when they meet impurities, other SIA loops, etc. Their migration is therefore achieved along a 3-D path made of 1-D segments (it is referred to as a mixed 1D/3D migration [128]). The capacity of loops to switch their moving direction decreases with their size. The role played by SIA loops in the irradiation response of RPV steels is not yet well understood and quantified.

- **Vacancy clusters**: large vacancy loops have never been observed in RPV steels irradiated in nominal conditions. Small vacancy clusters do exist however, and have been shown by PA[6] [129, 130].

Simulation studies showed that small vacancy clusters are more stable in a 3-D configuration than in a 2-D one [119,131]. However, it was also noticed that 3-D clusters

[6] **P**ositron **A**nnihilation

containing more than about 30 vacancies may present some fragments of $\{110\}$ vacancy platelets, which mark the beginning of a loop nucleation [132, 133]. Clusters containing more than about 100 vacancies may produce a stable nucleus of $\{110\}$ vacancy loop ($b = \frac{1}{2}\langle 110 \rangle$).

At around 290°C, small vacancy clusters and dislocation loops have a 3-D and 1-D migration respectively [134]. They are much less mobile than SIA clusters and dislocation loops of similar sizes. Vacancy clusters are also much less mobile than vacancy loops. As for SIAs, the role played by vacancy clusters in the irradiation response of RPV steels is not yet well understood and quantified.

III - Mechanisms controlling the embrittlement of RPV steels

3.1 - Mechanisms controlling the formation of irradiation-induced defects

The understanding of the mechanisms controlling the formation of irradiation-induced defects in RPV steels is not straightforward due to the large variety of involved phenomena and participating types of atom. The current vision on these mechanisms rely on the interpretation of various experimental programs and numerical simulations which can be classified as follows:

- neutron irradiation of pure Fe, binary or ternary alloys so as to identify the role played by each type of solute atom or impurity (e.g. [3, 108]);
- electron irradiations, so as to identify the role played by the isolated point defects (e.g. [48, 97]);
- numerical simulations (first principle), so as to get information on the mobility of point defects and point defect clusters as well as on the nucleation, long term behavior (growth of germs, dissolution,..) and structure of the hardening defects (e.g. [66, 114, 125]).

From the available results, the following scenario can be proposed to explain the formation of the irradiation-induced damage in RPV steels:

- Neutrons hit lattice-atoms which are called Primary Knock-on Atoms (PKAs). During their displacement, PKAs may be slowed-down by interactions with electrons and/or collisions with other atoms, which are called Secondary Knock-on Atoms (SKAs) (e.g. [135]). These SKAs can also leave their site and then be slowed-down by the same mechanism; the tertiary knock-on atoms can proceed on the same way and so on... It results a series of atomic displacements, so-called "displacement cascade" (Figure 11).

- The size of the displacement cascade increases as the PKA energy arises (e.g. [141]) and when the latter is high enough (about 40-50 keV in iron (e.g. [136, 137, 138, 139]), the displacement cascades split into sub-cascades (Figure 12).

- The PKAs also produce point defects between the sub-cascades. In their production area, these defects do not have a number density high enough to significantly interact each other, therefore most of them migrate into the bulk.

- Once all the PKA energy is dissipated in the displacement cascade, most of the created vacancies and SIAs annihilate each other. At the end of this recombination phase, only some surviving point defects are still existing. It is the migration of these surviving point defects which is responsible for the formation of hardening defects and segregation. The number (N) of surviving Frenkel pairs can be estimated with expressions such as $N = 5.57\ E_{dam}^{0.83}$ [140] or $N = 5\ E_{dam}^{0.74}$ [141] (where E_{dam} is the PKA damage energy, in keV). It is worth noticing that substitutional alloying atoms (Mn, Ni,…) and impurities (Cu,…) do not affect significantly the result of displacement cascades at the time scale of ps (e.g. [141]).

- During the following milli-seconds (Figure 13):
  - SIAs and SIA clusters migrate from the (sub)-cascade[7] area to the bulk,
  - vacancies and vacancy clusters have a three 3-D migration in the (sub)-cascade area. Their local number density is high enough for them to merge and collect some copper atoms, which leads to the formation of nuclei of small vacancy clusters, vacancy-copper clusters or pure copper clusters.

  If the copper content in the solid solution is high enough (> 0.1%), nuclei of pure copper precipitates may also appear in the bulk by a classical thermal germination process.

- Solute atoms (Cu, Mn, Ni, Si), vacancies, SIAs and SIA clusters migrate in the bulk and may meet pre-existing hardening defects by random walk, which absorb or annihilate them. Due to the vacancy super-saturation, the migration of solute atoms may be much faster than under purely thermal conditions (enhanced diffusion). Solute atoms may also migrate to hardening defects by a diffusion process induced by the flux of SIAs or vacancies reaching or leaving these defects (induced diffusion). It seems that the presence of Cu is required for the clustering of Mn, Ni and Si [66]. The propensity of these elements to remain in solid solution in low copper steels is coherent with their high solubility limits in iron.

[7] The term (sub)-cascade covers a sub-cascade or a cascade which can not split into sub-cascades (PKA recoil energy < 40-50 keV)

- Defects may emit species (SIAs, vacancies, solute atoms, …) by thermal-activated processes. Differences between emission and absorption rates, lead to the dissolution of nuclei and the growth of others which become stable hardening defects: SIA loops, vacancy clusters, vacancy-copper clusters and pure copper precipitates.

- As defects are enriched in copper, their emission rates of Ni, Mn, Si atoms decrease and they get enriched in these three elements.

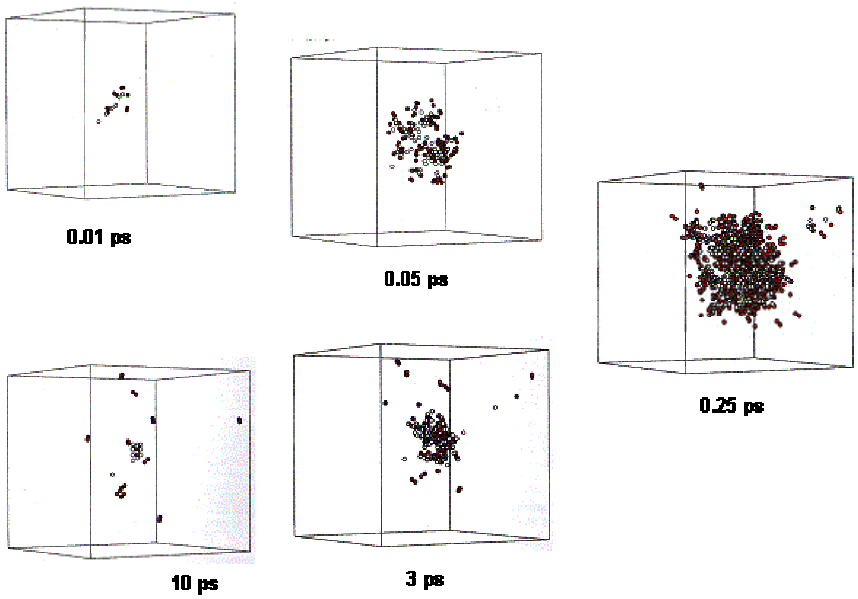

Figure 11: displacement cascade as simulated by MD in pure iron at 100K; cascade damage energy: 15 keV (recoil energy: 21 keV); white spheres: vacancies and black spheres: SIAs.

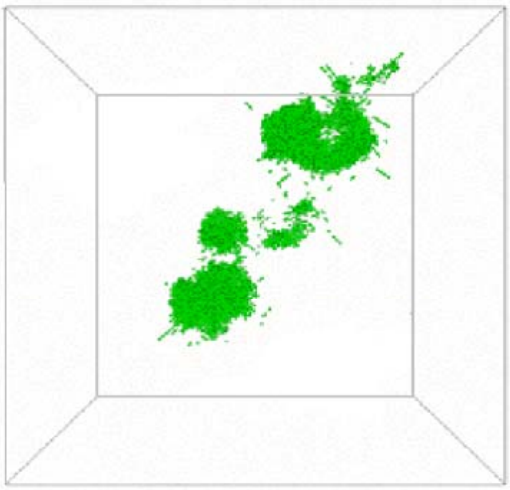

Figure 12: splitting of a displacement cascade into sub-cascades as simulated by MD in pure Fe at 100K; cascade damage energy : 40 keV (recoil energy: 61 keV) [137, 142].

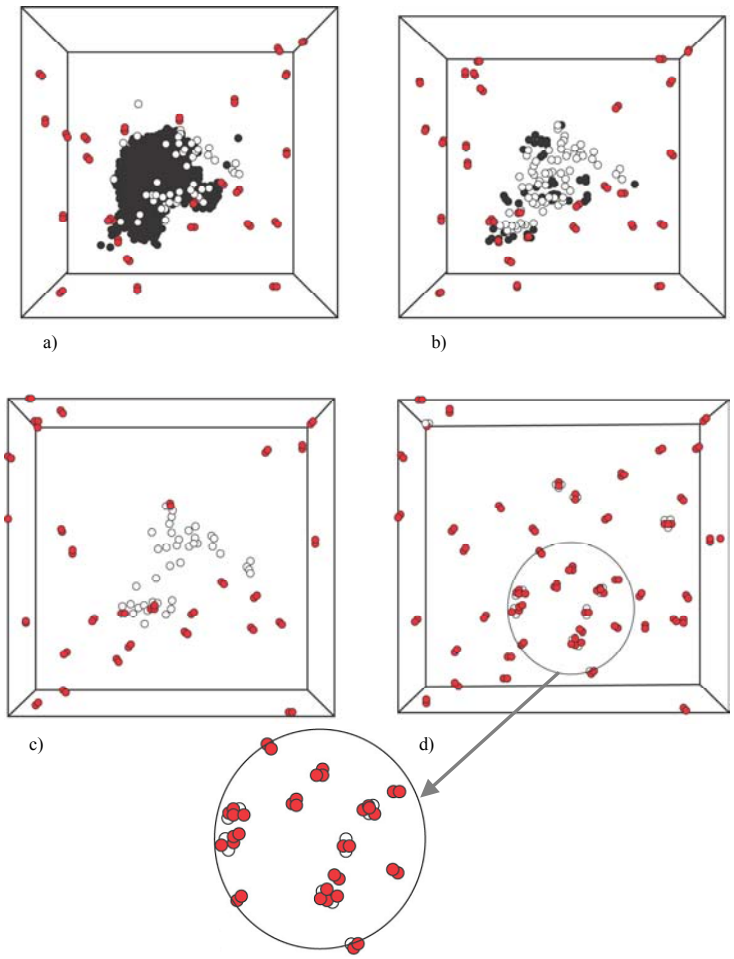

Figure 13: numerical simulation of formation of nuclei in a Fe-0.2%Cu alloy.
a) cascade peak (0.25 ps); (b) surviving defects at the end of the recombination phase (10 ps); (c) SIAs and SIA clusters have left the simulated crystal (10 µs); (d) nuclei of vacancy cluster and vacancy-copper clusters (few ms). (white spheres: vacancies, black spheres: SIAs, red spheres: copper atoms).

3.2 - Mechanisms controlling the evolution of mechanical properties

Irradiation-induced defects constitute obstacles to the gliding of dislocations (the involved mechanisms are described in Chapter IV), hence harden RPV steels, and consequently reduces their fracture toughness. In a wide range of temperatures, the irradiation-induced hardening of RPV steel is mainly controlled by athermal mechanisms, and thus is independent of the testing temperature (Figure 14). This independence, together with the steep temperature dependence of the yield stress typical of bcc structure, provides a

qualitative explanation for the irradiation-induced shift of the DBTT, as illustrated in Figure 14 : considering that the DBTT is defined by the intersection between the cleavage stress curve (which is almost temperature and irradiation independent) and the yield stress curve, then it appears that the increase of yield stress due to irradiation produces an upward shift in the point of intersection, corresponding to an increase in DBTT.

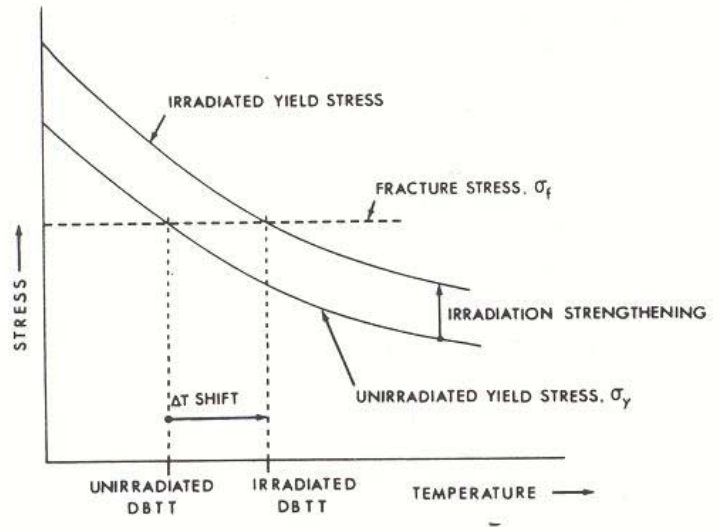

Figure 14 : schematic diagram showing how an irradiation-induced increase of yield stress results in a DBTT shift [143].

IV - Conclusion

This chapter shows that the "RPV community" has now a pretty good understanding of irradiation effects in RPV steels. It is understood that these effects result mainly from the segregation of phosphorus to grain boundaries and from the formation of 4 types of hardening defects : copper-rich precipitates, vacancy-solute atoms clusters, SIA dislocation loops and vacancy clusters. It is also obvious that the mechanisms controlling irradiation effects are dealing with several space and time scales. Consequently, the simulation of these effects require a multi-scale approach.

References

1 Jumel, S., van Duysen, J.C., "Mechanisms governing the irradiation-induced embrittlement of Light Water Reactor Pressure Vessel steels", AIEA, to be published.
2 Brillaud C., Hedin, ASTM-STP 1125, (1992), p. 23.
3 Auger, P., Pareige, P., Welzel, S., van-Duysen, J.C., J. Nucl. Mater., vol. 280, (2000), p. 331.
4 Miller, M.K. and Pareige, P., MRS meeting, Invited Paper R6.1, (2000).
5 Hyde, J. M., Ellis, D., English, C. A., Williams, T. J., ASTM-STP 1405, (2001), p. 262.
6 Hyde, J. M., English, C. A., "Microstructural Characterization of RPV steels – Phase 1", EPRI TR-107535, CRIEPI T989601 (1996).
7 Steele, L.E., "Neutron Irradiation Embrittlement of Reactor Pressure Vessel Steels", Tech. Rep., N°163, AIEA, Vienna, (1975).
8 Little, E. A., International Metals Reviews, (March 1976), p. 25.
9 Lucas, G., E., Odette, G. R., Lombrozo, P. M., J. W., Sheckherd, ASTM-STP 870, (1985), p. 900.
10 Odette, G., R., "Neutron Irradiation Effects in Reactor Pressure Vessel Steels and Weldments", IAEA report, ref IWG-LMNPP-98/3, chapter 10, (1998), p. 438.
11 Williams, T. J., Ellis, D., ASTM-STP 1405, (2001), p. 8.
12 U. S. Nuclear Regulatory Commission, "Radiation Embrittlement of Reactor Vessel Materials", Regulatory Guide 1.99, Rev. 2, (1988).
13 Jumel, S., Domain, C., Ruste, J., van Duysen, J.C., Becquart, C., Legris, A., Pareige, P., Barbu, A., Van Walle, E., Chaouadi, R., Hou, M., Odette, G.R., Stoller, R., Wirth, B.D., Journal of Testing and Evaluation, vol. 30, (2002), p. 37.
14 Odette, G. R., Wirth, B. D., J. Bacon, D., Ghoniem, N. M., MRS Bulletin Volume 26, No. 3, (March 2001), p. 176.
15 Davies, M., "A Comparison of Western and Eastern Nuclear Reactor Pressure Vessel Steels", AMES report N. 10, European Commission, DG JRC, Institute for Advanced Materials, report 17327 EN, (1997).
16 van Duysen, J.C., Bourgoin, J., Janot, C., Penisson, J. M., ASTM-STP 1125, (1992), p. 117.
17 Miller, M. K., Burke, M. G., ASTM-STP 1046, (1990), p. 107.
18 Le Bec P., private communication.
19 Petrequin, P., ASTM-STP 819, (1983), p. 29.
20 Odette, G.R., Lombrozo, P.M., EPRI Report NP 3319, Electric Power Research Institute, (1984).
21 Brillaud, C., Hedin, F., Houssin, B., ASTM-STP 956, (1986), p. 420.
22 Mancuso, J.F., Spitznagel, J.A., Shogan, R.P., Holland, J.R., ASTM-STP 725, (1981), p. 38.
23 Odette, G.R., Lucas, G.E., ASTM-STP 909, (1986), p. 206.
24 Buswell, J.T., Jones, R.B., ASTM-STP 1175, (1993), p. 424.
25 Mc Connell, P., Server, W.L., Oldfield, W., "Irradiated Pressure Vessel Steel", EPRI NP 2428, (1982).
26 Little, E.A., ASTM-STP 870, (1985), p. 1009.
27 Little, E.A., Harries, D.R., Metal Science Journal, vol. 4, (1970), p. 188.
28 Igata, N., Hasiguiti, R.R., Yagi, E., Nishiike, U., Watanabe, K., ASTM-STP 484, (1970), p. 128.

29 Little, E.A., Harries, D.R., ASTM-STP 457, (1969), p. 215.
30 Odette, G.R., Lucas, G.E., Journal of Non destructive Evaluation, vol. 15, N°3/4, (1996), p.137.
31 Odette, G.R., He, M.Y., J. Nucl. Mater., vol. 283, (2000), p. 120-127.
32 Sokolov, M. A., Nanstad, R. K., "Comparison of Irradiation-Induced Shifts of Kjc and Charpy Impact Toughness for Reactor Pressure Vessel Steels, U. S. Nuclear Regulatory report, ref NUREG/CR-6609, (2000).
33 Ruste, J., "IREMA, une Base de Données pour l'Etude des Effets d'Irradiation sur les Aciers de Cuve des Réacteurs Nucléaires", EDF report Ref. EDF/DER HT-41/94/049/A; (1994).
34 Harries, D. R. et al., UKAEA Report AERE-R4846, (1965).
35 Steele, L.E., Hawthorne, J.R., Gray, R.A., "Neutron Irradiation Embrittlement of Several Higher Strenght Steels", NRL-6419, Naval Research Laboratory (September 7, 1966) ; ASTM-STP-426 (1967), p. 346.
36 Serpan, C.Z., Steel, L.E., Hawthorne, J.R., "Radiation Damage Surveillance of Power Reactor Pressure Vessels", NRL-6349, Naval Research Laboratory (January 31, 1966) ; Trans. ASME, J. Basic Eng., Series D, 89, (1), (1967), p. 221.
37 Hawthorne, J.R., Serpan, C.Z., Watson, H.E., Gray, E.A., "Irradiation Effects on Reactor Structural Materials", NRL-1753, Naval Research Laboratory, (1967).
38 Potapovs, U., Hawthorne, J.R., "The Effect of Residual Elements on 550°F Irradiation Response of Selected Pressure Vessel Steels and Weldments", NRL-6803, Naval Research Laboratory, (November 22, 1968) ; also Nuclear Applications, vol. 46, N°1, (1969), p.27.
39 Potapovs, U., Hawthorne, J.R., Nuclear Applications, vol. 6, (January 1969), p. 27.
40 Hawthorne, J.R., ASTM-STP 484, (1970), p. 96.
41 Little, E.A., "Dimentional stability and mechanical behaviour of irradiated metals and alloys", Eds British Nuclear Energy Society, London, (1984), p.141.
42 Miller, M. K., Russell, K. F., J. Nucl. Mater., vol. 250, (1997), p.223.
43 Miller, M. K., Pareige, P., Burke, M. G., Materials Characterization, vol. 44, (2000), p. 235.
44 Pareige, P., Russel, K.F., Stoller, R.E., Miller, M.K., J. Nucl. Mater., vol. 250, (1997), p. 176.
45 Guionnet, C., Robin, Y., Flavier, C., Lefort, A., Gros, D., Perdreau, R., ASTM-STP 725, (1981), p. 20.
46 Varsik, J.D., Byrne, S.T., ASTM-STP 683, (1979), p. 252.
47 Pascal P., "Nouveau Traité de Chimie Minérale", Ed. Masson and Cie, (1963).
48 Miloudi, S., "Etude du Dommage d'Irradiation dans les Aciers de Cuve des Réacteurs à Eau Pessurisée ", PhD Thesis, Université d'Orsay, (1997).
49 Salje, G., Feller-Kniepmeier, M., Journal of Applied Physics, vol. 48, N°5, (1977), p. 1833.
50 Mc Lean, D., "Grain Boundaries in Metals", Oxford University, (1957).
51 Guttmann, M., Surface Science, vol. 53, (1975), p. 213.
52 Seah, M. P., Acta Metallurgica, vol. 25, (1977), p. 345.
53 Gurovitch, B.A., Kuleshova, E.A., Lavrenchuk, O.V., J. Nucl. Mater., vol.48, (1996), p. 330.
54 Bolton, C. J., Buswell, J. T., Jones, R. B., Muskovic, R., Priest, R. H., ASTM-STP 1270, (1996).
55 Jones, R. B., Jones, Bolton, C. J., Twenty Fourth Water Reactor Safety Information Meeting, NUREG/CP-0157, (1996).

56 Buswell, J.T., Phythian, W.J., McElroy, R.J., Dumbill, S., Ray, P.H.N., Mace, J., Sinclair, R.N., J. Nucl. Mater., vol. 225, (1995), p.196.
57 Jones, R. B., Buswell, J. T., Proceedings of the 3rd International Symposium on Environmental Degradation of Reactor Materials-Water Reactor, Met. Soc. Inc., Warrendale, Pa, USA, (1988), p. 111.
58 Barton, P.J., Harries, D.R., Mogford, I.L., Journal of the Iron and Steel Institute, vol. 203, N°5, (1965), p. 507.
59 Guionnet, C., Robin, Y., Flavier, C., Lefort, A., Gros, D., Perdreau, R., ASTM-STP 725, (1981), p. 20.
60 Hawthorne, J. R., Nuclear Technology, vol. 59, N° 3, p. 41.
61 Hawthorne, J. R., ASTM-STP 819, (1983), p. 100.
62 Guionnet, C., Houssin, B., Brasseur, D., Lefort, A., Gros, D., Perdreau, R., ASTM-STP 782, (1982), p. 392.
63 Odette, G. R., Mat. Res. Soc. Symp.Proceedings, Material Research Society, (1995), vol. 373, p. 137.
64 Burke, M. G., Stofanak, R., J., Hyde, J. M., English, C. A., Server, W. L., ASTM-STP 1447, (2003).
65 Hyde, J. M., Ellis, D., English, C. A., Williams, T. J., ASTM-STP 1405, (2001), p. 262.
66 Odette, G.R., Lucas, G.E., Radiation Effects and Defects in Solids, vol. 144, (1998), p. 189.
67 Odette, G.R., Wirth, B.D., J. Nucl. Mater., vol. 251, (1997), p. 157.
68 Odette, G.R., Private communication.
69 Odette, G.R., Scripta Metallurgica, vol. 11, (1983), p. 1183.
70 Vacek, M., ASTM-STP 909, (1986), p. 260.
71 Odette, G. R., Lombrozo, P. M. Physisally Based Regression Correlations of Embrittlement Data From Reacture Pressure Vessel Surveillance Programs, EPRI Report NP-3319, (1984).
72 Varsik, J.D., Byrne, S.T., ASTM-STP 683, (1979), p. 252.
73 Eason, E. D., Wright, J. E., Improved Embrittlement Correlation for Reactor Pressure Vessel Steels, NUREG:CR-6551, U. S. Nuclear Regulatory Commission, (1998).
74 Ahlf,, J. Scmitt, F. J., J. Nucl. Mater., vol. 105, (1982), p. 48.
75 Odette, G.R., Lucas, G.E., EPRI Report NP 6114, Electric Power Research Institute, (1989).
76 Houssin, B., "Réévaluation des Marges à la Rupture de Cuve. Prévisison de a Fragilisation par Irradiation des viroles et Soudures de Cuves Basée sur les Teneurs en Cu, P et Ni", Note d'étude Framatome, EEM DC 0328, (Novembre 1983)
77 Suzuki, M., Onizawa, K., Kizzaki, M., ASTM-STP 1270, (1996), p. 351.
78 Tran Dai Phuc, "Influence du spectre de neutrons sur la Fragilisation des Aciers de Cuve de Réacteurs", Note CEA N. 2077, (1979).
79 Pichon, C., Brillaud, C., Deylier, D., Alberman, A., Soulat, P., ASTM-STP 1366, (2000), p. 87 and Alberman, A., CEA Note technique n°95 123 - Affaire 2326, (1996).
80 Stoller, R.E., Farrel, K., Mansur, L.K., "The Effect of Thermal Neutrons and Fast Flux on Tensile properties of Ferritic Steels Irradiated at Low Temperature", ORNL Report ORNL/NRC/LTR-96/3, (February 1996).
81 Dohi, K., Onchi, T., Kano, F., Fukuya, K., Narui, Kayano, H., J. Nucl. Mater., vol. 265, (1999), p. 78.
82 Serpan, C.Z., McElroy, W.N., "Radiation Damage in Materials" 1969 (Proc. Symp. Vienna, 1969), vol. 2, IAEA, Vienna, (1969), p.33.
83 Mansur, L.K., Farrel, K. , J. Nucl. Mater., vol. 244, (1999), p. 212.

84 Alberman, A., Proceedings of the Fourth ASTM-EURATOM Symposium of Reactor Dosimetry, (1982), p. 839.
85 Jones, R. B., Derek, J. E., Woottom, M. R.., ASTM-STP 1366, (2000), p. 366.
86 Mansur, L. K., Farrell, K., J. Nucl. Mater., vol. 170, (1990), p. 236.
87 Heinisch, H. L., J. Nucl. Mater., vol. 178, (1991), p. 19.
88 Petrequin, P., Soulat, P., Proceedings of IAEA Specialists Meetings on "Irradiation Embrittlement, Thermal Annealing, and Surveillance of Reactor Pressure Vessels", IWG-RRPC 79/3, IAEA, Vienna, (1979), p. 195.
89 Odette, G.R., Lucas, G.E., Klingensmith, D., Stoller, R.E., Pythian, W.J., ASTM-STP 1175, (1994).
90 Suzuki, M., Onisawa, K., Kizaki, M., ASTM-STP 1270, (1996).
91 Proceedings of "Workshop on Dose Rate effects in Reactor Pressure Vessel Materials", EPRI-CRIEPI, (Nov. 12-14, 2001).
92 Petrequin, P., "A review of Formulas for Predicting Irradiation Embrittlement of Reactors Vessel Materials", AMES, report N°6.
93 Guthrie, G.L., NUREG/CR-1240, (1979).
94 Jones, R.B., Williams, T.J., ASTM-STP 1270, (1996), p. 569.
95 Smidt, F. A., Steele, L. E., "Residual Elements and Irradiation Embrittlement", NRL report, ref 7310, Naval Research Laboratory, (1971).
96 Smidt, F. A., Sprague, J. A., ASTM-STP 529, (1973), p. 78.
97 Akamatsu, M., "Evolution Structurale d'Alliages Ferritiques sous Irradiation", PhD thesis,, Université d'Orsay, (1994).
98 Odette, G.R., Mader, E.V., Lucas, G.E., Phythian, W.J., English C.A., ASTM-STP 1175, (1993), p. 373.
99 Pareige, P., "Etude à la Sonde Atomique de l'Evolution Microstructurale sous Irradiation d'Alliages Ferritiques Fe-Cu et d'Aciers de Cuve de Réacteurs Nucléaires", Phd Thesis, Université de Rouen, (1994).
100 English, C. A., Phythian, W. J., Buswell, J. T., Hawthorne, J. R., Ray, P. H. N., ASTM-STP 1125, (1992), p. 93.
101 Odette, G.R., Wirth, B.D., J. Nucl. Mater., vol. 251, (1997), p. 157.
102 Pareige, P., Auger, P., Van Duysen, J.C., Journal de Physique IV, vol. 11, (2001).
103 Miller, M.K., Russell, K.F., Stoller, R.E., Pareige, P., "Atom Probe Tomography Characterization of the Solute Distribution in a Neutron-Irradiated ad Annealed Pressure Vessel Steel Weld", Report NUREG/CR-6629, ONRL/TM-13768.
104 Hyde, J.M., English, C.A., "Microstructural Characterization of RPV steels- Summary of Phases I & II and next Program Plan, report AEAT-4159, (1998).
105 Domain, C., private communication.
106 Odette, G. R., Sheeks, C. K., "Phase stability during irradiation", Eds J. R. Holland, L; K. Mansur and D. I. Potter, TMS AIME, (1982), p. 415.
107 Burke, M. G., Stofanak, R., J., Hyde, J. M., English, C. A., Server, W. L., ASTM STP 1447, (2003).
108 Pareige, P., "Etude à la Sonde Atomique de l'Evolution Microstructurale sous Irradiation d'Alliages Ferritiques Fe-Cu et d'Aciers de Cuve de Réacteurs Nucléaires", Phd Thesis, Université de Rouen, (1994).
109 Pareige, P., Stoller, R.E., Russell, K.F., Miller, M.K., J. Nucl. Mater., vol. 249, (1997), p. 165.
110 Pareige, P., Miller, M. K., Applied Surface Science, vol. 94/95, (1996), p. 370.
111 Miller, M. K., Russell, K. F., Stoller, R. E., Pareige, P., "Atom Probe Tomography Characterization of the Solute Distribution in a Neutron-Irradiated ad Annealed Pressure

Vessel Steel Weld“, Report NUREG/CR-6629, ONRL/TM-13768.
112 Hyde, J. M., English, C. A., “Microstructural Characterization of RPV steels- summary of Phases I & II and next Program Plan, report AEAT-4159, (1998).
113 Domain, C., private communication.
114 Hardouin-Duparc, A., "Etude de la Formation des Amas de Défauts Ponctuels dans les Alliages Ferritiques Faiblement Alliés", PhD Thesis, Université Paris-Sud, Orsay, (1997).
115 Iwai, T., Kawanishi, H., Arai, Y., Kato, Y., Sekimura, N., Ishino, S., ASTM-STP 1204, (1993), p. 228.
116 Puigvi, M.A., Osetsky, Y.N., Serra, A., "Point-Defect Clusters and Dislocation Loops in bcc Metals: continuum and atomistic study", Phil Mag., in press.
117 Wirth, B.D., Odette, G.R., Maroudas, D., Lucas, G.E., J. Nucl. Mater, vol. 276, (2000), p. 33.
118 Kuramoto, E.J., Nucl. Mater, vol. 276, (2000), p. 143.
119 Osetsky, Y., Serra, A., and Priego, V., J. Nucl. Mater., vol. 276, (2000), p. 202.
120 Ward, A. E., Fisher, S. B., J. Nucl. Mater., vol. 166, (1989), p. 227.
121 Little, E. A., Bullough, R., Wood, M. H., Proc. Royal. Soc. London, A. 372, (1980), p. 565.
122 Soneda, N., Diaz de La Rubia, T., Philosophical Magazine A, vol. 78, (1998), p. 995.
123 Marian, J., Wirth, B. D., Perlado, J. M., Phys. Rev. Letters, vol 88, N° 25, (2002), p. 25507-1.
124 Osetsky, Y. N., Bacon, D. J., Serra, A., Singh, B. N., Golubov., J. Nucl. Mater., vol. 276, (2000), p. 65
125 Wirth, B.D., PhD dissertation, University of California, Santa Barbara, (1998).
126 Domain, C., private communication.
127 Becquart, C.S., Domain, C., Legris, A., van Duysen, J.C., J. Nucl. Mater., vol. 280, (2000), p. 73.
128 Heinisch, H.L., Singh, B.N., Golubov, S.I., J. Nucl. Mater, vol. 283-287, (2000), p. 737.
129 Akamatsu, M., Dai, G., Li, X., Moser, P., van Duysen, J. C., Zacharie, G., ASTM-STP 1175, (1993).
130 Li, X., "Etude des Processus de Formation des Microcavités dans les Alliages Ferritiques des Cuves des Réacteurs Nucléaires" PhD Thesis, Université Joseph Fourrier-Grenoble 1, (1995).
131 Becquart, C., personal communication.
132 Kapinos V.G., Osetsky, Y.N., Platanov, P.A., J. Nucl. Mater., vol. 170, (1990), p. 66.
133 Kapinos V.G., Osetsky, Y.N., Platanov, P.A., J. Nucl. Mater., vol. 173, (1990), p. 229.
134 Osetsky, Y.N., Bacon, D.J., Serra, A., Mater. Res. Soc. Symp. Proc., 538, (1999), p. 649.
135 Lehmann, C., "Interaction of radiation with solids and elementary defect production", Defects in Crystalline Solids Vol 10, Ed. S. Amelinckx, R. Gevers, J. Nihoul, Elsevier North-Holland, (1977).
136 Jumel, S., van-Duysen, J.C., J. Nucl. Mater. , vol. 328, (2004), p. 151.
137 Stoller, R. E., Odette, Wirth, B. D., J. Nucl. Mater., vol. 251, (1997), p. 49.
138 H. Heinisch, B. N. Singh, Phil. Mag. A, vol 67, N°2, (1993), p.407.
139 Stoller, R.E., Greenwood, L.R., J. Nucl. Mat., vol. 271&272, (1999), p. 57.
140 Bacon, D. J., Gao, F., Barashev, A. V., Osetsky, Y. N., Mater. Res. Soc. Symp., vol. 540, (1999), p. 617.
141 Becquart, C. S., Domain, C., van Duysen, J. C., Raulot, J. M., J. Nucl. Mater., vol. 294, (2001), p. 274.

142 Stoller, R.E., and Calder, A.F., presented at the Ninth International Conference on Fusion Reactor Materials, 10-15 October 1999, Colorado Springs, CO, Journal of Nuclear Materials, in press.
143 Wechsler, M. S., ASTM-STP 457, (1969), p. 242.

CHAPTER II

Description of RPV-1

The building of RPV-1 successively required to:

- model the formation of the irradiation induced damage in RPV steels, as well as the plasticity behavior of these steels after irradiation;
- select codes and models to carry out the simulations of the involved mechanisms. Since our main focus was to build a first tool (rather than a perfect tool), we decided to use, as much as possible, existing codes and models in spite of their imperfections. It was intended that subsequent effort would lead to improve them or propose new ones. Nevertheless, two codes (DUPAIR and INCAS) were missing and had to be developed in the framework of this thesis;
- propose an architecture to link the selected codes and models.

All these points are described in this chapter.

The first paragraph gives the hypotheses used for the modeling. The second paragraph describes the selected codes and models as well as the architecture of RPV-1. The third one explains the main steps of a typical simulation and finally, a description of the simulated evolution of the hardening defects is given in the fourth paragraph.

The elements given in this chapter were extracted from a larger document accepted for publication in Journal of Nuclear Materials [1].

I - Models used to build RPV-1

1.1 - Modeling of the irradiation-induced damage

The hypotheses used to model the formation of the irradiation-induced damage are given hereafter. Some of them are in conformity with the current state of knowledge partially described in the previous chapter: they are preceded by the symbol (♦). The other ones have been made to facilitate the building of RPV-1; they rely on the current knowledge but will have to be reconsidered for the subsequent versions of this VTR: they are preceded by the symbol (♣).

♣ The irradiation-induced increase of yield stress is independent of the steel type (forging, plate, weld) and slightly depends on its metallurgical microstructure.

Only the grain or lath size and the dislocation density have an influence (effects of size and distribution of carbides, shape of grains… are not accounted for).

♣ In its current version, RPV-1 does not take into account the intergranular segregation of phosphorus. Consequently, it cannot be used to forecast the behavior of steels containing more than about 150 ppm of phosphorus.

♣ The only chemical elements controlling the irradiation-induced hardening are Cu, Mn and Ni (Si is not allowed for, carbon and nitrogen are indirectly taken into account by reducing the mobility of vacancies).

♣ The irradiation induces the formation of the four following types of hardening defects:
- 2-D SIA clusters and dislocation loops with {111} habit planes;
- spherical vacancy clusters;
- spherical copper-rich precipitates containing Mn and Ni atoms;
- spherical vacancy-solute (Cu, Mn, Ni) clusters.

♦ Primary Knocked-on Atoms (PKAs) induced by neutrons produce displacement cascades which may split into sub-cascades. They also produce some point defects between the sub-cascades.

♦ Alloying elements and impurities do not affect:
- the generation of PKAs and (sub)-cascades[1];
- the "collision" and "recombination" phases of (sub)-cascades;
- the production and distribution of point defects between the sub-cascades.

These phenomena are also supposed to be temperature-independent between 0 and 600K. Consequently, they can be simulated in pure iron at any temperature below 600K.

♦ During their "collision" and "recombination" phases, sub-cascades belonging to the same cascade or to different cascades do not interact; they neither interact with any defect migrating in the bulk. They can therefore be simulated separately.

♣ At the end of their recombination phase (some tens of pico-seconds), each sub-cascade leaves isolated or clustered surviving point defects. The short-term evolution (some milliseconds) of these defects occurs without any interaction

[1] The term (sub)-cascade covers a sub-cascade or a displacement cascade which cannot split into sub-cascades (PKA recoil energy < 40-50keV).

with other (sub)-cascades or migrating defects, and can thus be simulated separately.

♣ Cu is the only alloying element playing a role in the short-term evolution of the point defects left by the (sub)-cascades (some milliseconds). This evolution can therefore be simulated in a Fe-Cu alloy. It can be described as follows:

- SIAs and SIA clusters migrate (1D/3D migration) from the (sub)-cascade area to the bulk, some of them may merge or interact with surviving vacancies (leading to the annihilation of SIAs and vacancies). In the bulk, they may act as nuclei of SIA dislocation loops or interact with pre-existing hardening defects or other features (grain boundaries, dislocations,…).
- vacancies and vacancy clusters have a 3-D migration in the (sub)-cascade area. Their number density in this area is high enough for some of them to merge and/or to collect some copper atoms, which leads to the formation of nuclei of hardening defects: small vacancy clusters, vacancy-copper atom clusters or pure copper clusters.

In the following part of the document, the defects (SIAs, SIA clusters, vacancy clusters, vacancy-copper clusters,...) resulting from the short term evolution of the surviving point defects left by a (sub)-cascade will be called "nuclei of hardening defects" produced by the (sub)-cascade.

♣ When a displacement (sub)-cascade is generated within a sphere of radius R_{int} centered on a pre-existing hardening defect, its residual point defects are supposed to be attracted by this defect and to annihilate on it. Thus, the cascade has no effect. The probability of occurrence of such an event is given by:

$$P(t) = 1-\exp(-G\, V_{int}\, t) \qquad (1)$$

where G is the (sub)-cascade generation rate ($cm^{-3}.s^{-1}$);
V_{int} is the interaction volume, $V_{int} = 4\,\pi\, R_{int}^3 / 3$;
R_{int} = 1 nm in the current version of RPV-1;
t is the irradiation time.

♣ The surviving vacancies created between the sub-cascades are isolated while the SIAs are distributed as follows: 60% are isolated, 20% are in clusters of size 2, 10% in clusters of size 3, 6% in clusters of size 4, 3% in clusters of size 5 and 11% in clusters if size 6. It is supposed that, in their production area, all these point defects are not in a number density high enough to significantly interact with each others or with solute atoms and to form nuclei of defects. Most of them therefore migrate into the bulk.

♦ If the copper content in the solid solution is high enough (> 0.1%), nuclei of pure copper precipitates may also appear in the bulk through a classical thermal germination process accelerated by irradiation.

♣ Copper enrichment of hardening defects occurs by enhanced and induced precipitation (cf § 2.2.a). It means that copper atoms reach these defects by the two following mechanisms:
- a random walk mechanism, accelerated by the super-saturation of vacancies.
- a diffusion process induced by an interaction with the fluxes of vacancies (interactions with the fluxes of SIAs is not accounted for in the current version of RPV-1, as first principle calculations show that the interaction between copper and SIA is negligible [2]).

♣ As hardening defects are enriched in copper, they get also enriched in Ni and Mn. This enrichment relies on an irradiation enhanced diffusion mechanism and is influenced by the interface between the matrix and the defects. In RPV-1, the numbers of Mn and Ni atoms in each defect are considered to be proportional to the number of copper atoms in the defect. The proportionality factors are calculated at the thermodynamic equilibrium (identity of the chemical potentials in the matrix and in precipitates). It is also supposed that the thermodynamic principles are not applicable for defects containing less than five copper atoms. Consequently, only defects containing more than five copper atoms are enriched in Mn and Ni atoms.

♦ Hardening defects may emit solute atoms, vacancies or SIAs through thermal-activated processes. Differences between emission and absorption rates lead to the dissolution of defects and the growth of others.

1.2 - Modeling of the plasticity behavior

Irradiation-induced defects constitute obstacles to the gliding of dislocations and thus have a hardening effect. The hypothesis used to model the gliding of dislocations and their interactions with the defects are described in Chapter IV.

II - Description of RPV-1

RPV-1 was built so that its inputs and outputs are similar to those of experimental irradiation programs carried out to assess the in-service behavior of steels (Figure 1). Its inputs are:

- the irradiation conditions: neutron spectrum, temperature and time of irradiation;
- the characteristics of the non-irradiated steel: nominal or free Cu, Mn and Ni contents, grain size, density of dislocations, yield stress;
- the conditions of the tensile test: temperature and deformation rate.

The description of the irradiation-induced evolution of the microstructure and the concomitant increase of the yield stress are the main outputs. By using theoretical or empirical correlations, the irradiation-induced shift of the DBTT can be determined from the increase of the yield stress (see Chapter I and e.g. [3]).

Section 2.1 provides a description of the overall architecture of RPV-1, i.e. the way the selected codes have been linked up together and connected to the databases. In section 2.2, a brief description of these codes and the procedures followed to build up the databases are given.

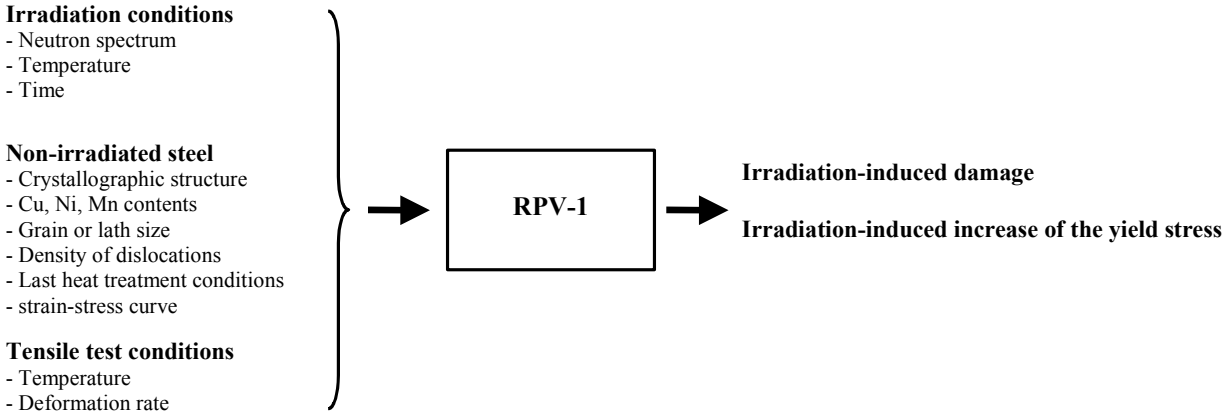

Figure 1: description of RPV-1 inputs and outputs.

2.1 - Architecture of RPV-1

The architecture of RPV-1 is sketched on Figure 2, and may be described as a stack of "racks". Each of these racks contains a code or a database and is linked up with the others so as to receive, treat and/or transmit data. Built in that way, RPV-1 is an evolutionary tool and can be improved very easily: as soon as a new code or model is available, it can be implemented without any difficulty by replacing a "rack" by a new one. The codes and databases used in RPV-1 are

accompanied by pre- and post-treatment scripts in order to link them up and transmit data. They are also embedded in a Python interface (developed by Y. Souffez –EDF-) which facilitates the running of the simulations and the visualization of the results. The main board of this interface (Figure 3) is used to select inputs concerning the irradiation conditions (neutron spectrum, irradiation time and temperature), steel (%Cu, %Ni, %Mn) and tensile test (temperature, deformation rate). Auxiliary boards are also available to select complementary steel-related inputs (grain size, dislocation density) and all the physical parameters required by the codes (point defect formation energies, defect migration energies...). As seen in Figure 2, three modules (which can be run separately) are identified in RPV-1:

- the "short-term irradiation" module treats the neutron spectrum to provide the PKA spectrum (with the code SPECMIN, see § 2.2.a) and then, the (sub)-cascade spectrum in pure iron (with the code INCAS, § 2.2.b and Chapter III). By convoluting the (sub)-cascade spectrum [number of (sub)-cascades versus the dissipated energy] and the size distribution of nuclei of hardening defects produced by each (sub)-cascade (given in the database CASCADE, see § 2.3.a), it defines a part of the source term for the long-term irradiation module. The generation rate of point defects (isolated or clustered) between the sub-cascades is the other part of this source term.

- the "long-term irradiation" module mainly includes a rate theory code (so-called MFVISC, see § 2.2.c) to simulate the evolution of the irradiated microstructure from about 10^{-3} second to years. This module continuously checks the evolution of the microstructure so as to adjust the source term to account for: i) the evolution of the free copper content in the matrix, ii) the interaction of displacement cascades with pre-existing defects.

- the "hardening" module finalizes the simulation of the formation of the hardening defects by enriching in Ni and Mn those containing Cu, using results provided by a kinetic-thermodynamics code (so-called DIFFG, see § 2.2.d). It simulates also a tensile test with a mesoscopic code (the Foreman and Makin type code called DUPAIR, see § 2.2.e and Chapter IV), using a database of pinning forces (called FORCE, see § 2.3.b and Chapter IV).

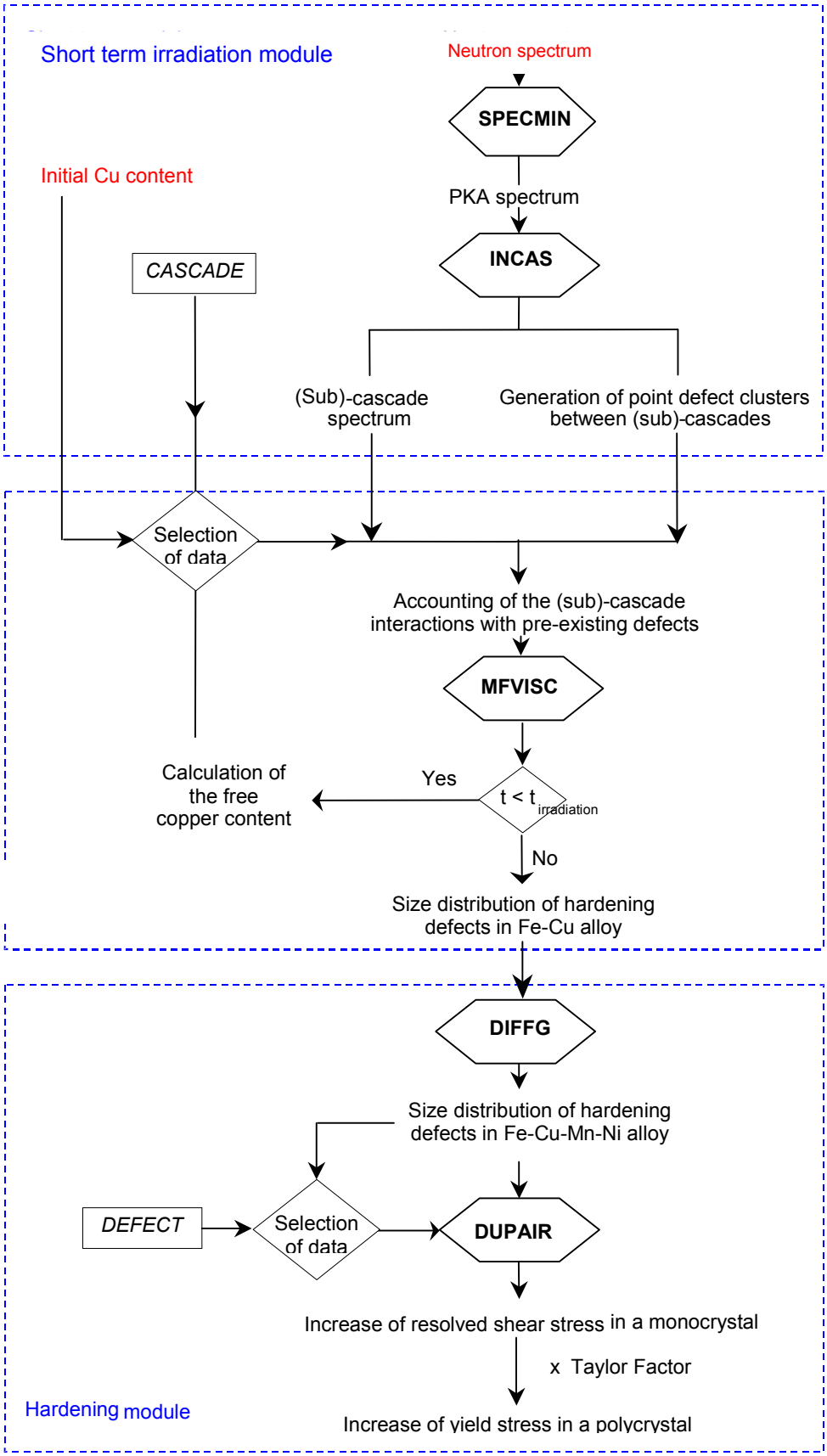

Figure 2: schematic structure of RPV- 1. To simplify the figure, only two input data (neutron spectrum and initial copper content) are indicated.

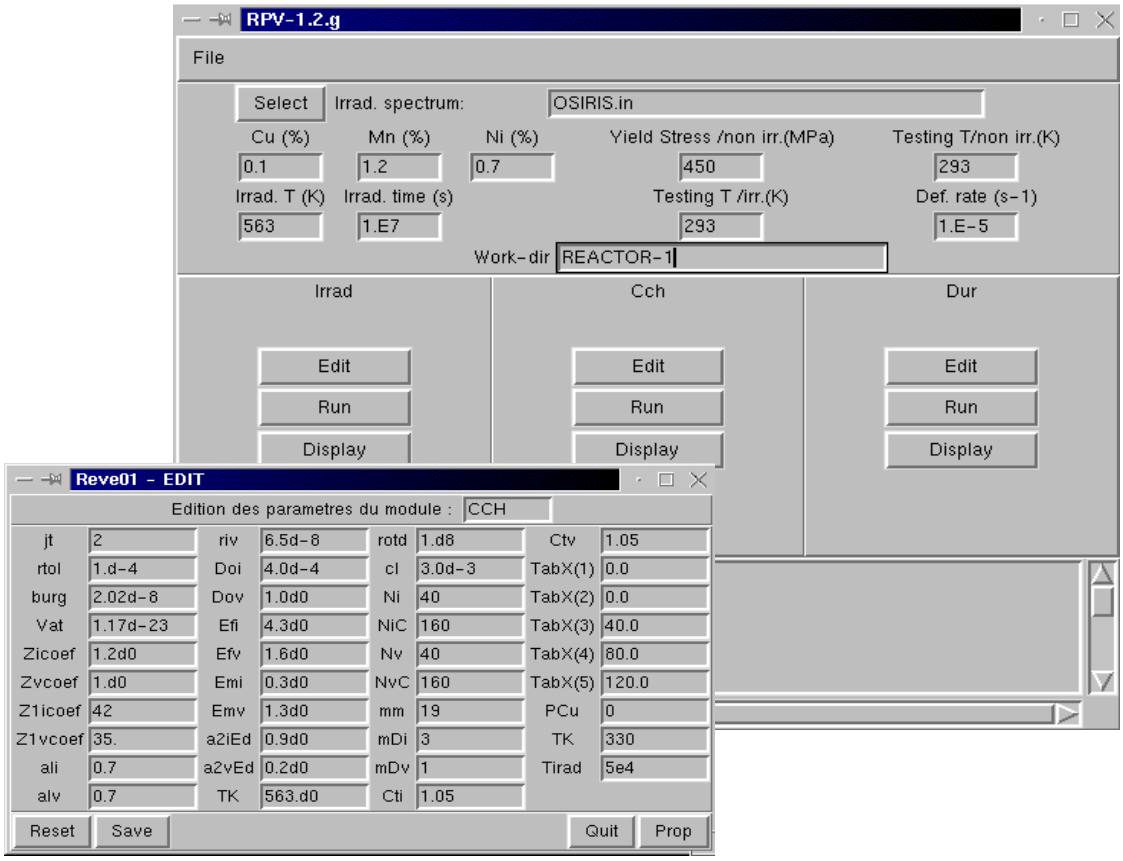

Figure 3: Python user's friendly interface of RPV- 1: main board used to select input data concerning the irradiation conditions, steel and tensile test; one of the auxiliary boards to select complementary physical parameters and inputs concerning the steel.

2.2 - Codes used to build RPV-1

This section provides a short description of the codes used to build-up RPV-1. Among them, SPECMIN, INCAS, MFVISC, DIFFG and DUPAIR are directly chained in RPV-1 (see Figure 2). Two other codes DYMOKA and LAKIMOCA, have been used to build up the two databases CASCADE and FORCE integrated in RPV-1.

a) SPECMIN

SPECMIN is a simplified version of the code SPECTER; both codes have been developed by L. Greenwood from Pacific Northwest National Laboratory [4]. SPECMIN provides less information than SPECTER, but allows the simulations to be operated on a PC-type computer with typical running times of a few seconds. It is written in FORTRAN.

SPECMIN relies on the Binary Collision Approximation (BCA) and simulates the interactions between neutrons and atoms of pure elements. It takes into account the elastic collisions as well as inelastic interactions and all possible direct nuclear reactions, such as (n,p), (n,α), (n,2n) etc, between both kinds of particles. All these phenomena are characterized by differential neutron cross sections available from the Evaluated Nuclear Data File database (ENDF). ENDF data and their uncertainties can be obtained from the National Neutron Cross Section Center at Brookhaven National Laboratory (USA). For a given neutron spectrum, the calculations with SPECMIN successively lead to the following results:

- the PKA spectrum (number of PKAs expressed as a function of PKA's recoil energy) in which PKAs are classified and counted with respect to energy groups. For the subsequent calculations, all the PKAs belonging to the same group are considered as dissipating the same energy, i.e. the middle group energy;
- the gas production calculated from the nuclear reactions;
- the "damage energy" (T_{dam}) of PKA's calculated from their recoil energy according to the Lindhard's theory [5];
- the dpa rate calculated from the Norgett, Robinson and Torrens expression (NRT dpa [6]) which gives the total number (N_s) of atoms displaced per PKA: $N_s=0.8T_{dam}/2E_d$ (E_d is the minimal energy required to displace an atom from its lattice site).

b) INCAS

As already mentioned, INCAS has been developed in the framework of this thesis. It was programmed in FORTRAN by EDF [7]. A precise description of INCAS is given in chapter III. This section summarizes some key points.

INCAS is based on the Binary Collision Approximation and simulates the fate of PKAs from the time they are knocked by a neutron, up to the time they spread all their kinetic energy and thus stop moving. It forecasts their elastic collisions with lattice atoms and interactions with electrons. INCAS provides the average number and size of the damage zones (zones where Frenkel pairs are produced) induced by the PKAs according to their recoil energy. It also provides the distance between successive damage zones and the energy dissipated in each of them. Two cases have been identified:

- damage zones in which the dissipated energy is higher than 8.3 keV are considered as (sub)-cascades. They are classified and counted with respect to 5 dissipated energy groups: 5-15, 15-25, 25-35, 35-45, 45-55 keV (the so-called (sub)-cascade spectrum). For the subsequent calculations, all the (sub)-cascades belonging to a same group are considered as dissipating the same energy, i.e. the middle group energy.

- damage zones in which the dissipated energy is lower than 8.3 keV are considered to produce Frenkel pairs between the sub-cascades. At the end of the recombination phase, the number of surviving Frenkel pairs left by each of these damage zones can be estimated with the expression (defined by Molecular Dynamics simulations; e.g. [8]):

$$\nu(E) = 5\ (T_{dam})^{0.74} \qquad (1)$$

where T_{dam} is the damage energy, in keV. The surviving SIAs and vacancies are considered isolated or clustered in small nuclei (SIAs : 60% are isolated, 20% in clusters of size 2, etc; see § 1.1 of this Chapter).

c) MFVISC

MFVISC (Mean Field Vacancy Interstitial Solute Clusters) is a Rate Theory code developed with V. Duwig (EDF), A. Ponçot (EDF) and A. Barbu (CEA), from the MFVIC code [9, 10]; it is written in FORTRAN. For the building of RPV-1, MFVISC was used to reproduce the long-term evolution of the irradiation-induced damage.

In its current version, it simulates the fate of the vacancies, copper atoms and SIAs and provides, for selected irradiation times and as a function of their size, the distribution of :

- SIAs clusters and dislocations loops,
- pure Cu clusters,
- pure vacancy clusters,
- vacancy-copper clusters.

The vacancy clusters and SIA dislocation loops containing up to 20 elements can be mobile, their mobility are parameters of the code. The other defects are immobile.

In order to reduce the computer requirements, small defects are treated by discrete equations (i.e.: one equation per defect size) while large defects are treated by so-called “continuous equations” (i.e.: one equation for a group of defect sizes). A detailed presentation of MFVISC is available in [11]. In RPV-1, MFVISC is used with a standard parameterization (Table I) which was not optimised in the framework of this thesis. The improvement of this parameterization is being done by the international community (e.g. [9]).

Table I: parameterization of MFVISC used in RPV-1

Name	Nature	Value
E^m_v	Vacancy migration energy (eV)	1.3
E^m_i	Interstitial migration energy (eV)	0.3
E^f_v	Vacancy formation energy (eV)	1.9
E^f_i	Interstitial formation energy (eV)	5
D^0_v	Vacancy diffusion pre-exponential factor (cm^2/s)	1
D^0_i	Interstitial diffusion pre-exponential factor (cm^2/s)	$4\ 10^{-4}$
E^b_v	Binding energy of di-vacancies (eV)	0.2
E^b_i	Binding energy of di-interstitials (eV)	1
ρ	Dislocation density (cm^{-2})	10^{10}

d) DIFFG

In RPV-1, Mn and Ni atoms are introduced into the simulation with the DIFFG code, developped by G.R. Odette from the University of California at Santa Barbara and B. Wirth from the University of California at Berkeley [12, 13]. DIFFG is a kinetic-thermodynamics code written in FORTRAN, which determines the phase stability in a Fe-Cu-Mn-Ni system by taking into account the influence of the precipitate–matrix interfaces. The precipitate evolution is modeled by tracking the flows of alloying atoms imposed by the difference of chemical potentials between the matrix and the precipitates. The cluster radius and composition are followed as a function of time until each alloying atom has the same chemical potential in the matrix and in the precipitates. The final ratios (Mn content) / (Cu content) and (Ni content) / (Cu content) in the precipitates are then calculated. They are used to determine the Mn and Ni enrichments of the Cu-bearing hardening defects simulated with the MFVISC code.

e) DUPAIR

DUPAIR is used to assess the irradiation-induced hardening. It is a Foreman-and Makin-type code developped in the framework of this thesis. Its programmation was made in C by C. Domain (EDF) [14]. A precise description of DUPAIR and its parameterization is given in chapter IV. This section summarizes some key points.

In DUPAIR, the studied material is represented as a parallelepipedic box and the different types of irradiation-induced defects are randomly distributed according to their

number density, each defect being characterized by its type, size and pinning force. The code simulates the gliding of one dislocation line in the mid-plane of the box. The maximal shear stress required to make the dislocation cross this box is considered as the irradiation-induced increase of the resolved shear stress of a grain. It is multiplied by the Taylor factor (≈ 3) to get the increase of yield stress of the poly-crystalline material, which is assimilated to the increase of the conventional yield stress $\Delta R_{P0.2}$. As already mentioned, the irradiation-induced shift of the Charpy brittle ductile transition temperature can be determined from this increase of the yield stress by using empirical and theoretical correlations.

DUPAIR is applied at different irradiation time so as to deliver a complete time-dependant hardening curve. The results are provided as a function of dpa, irradiation time, fluence or fluence of neutrons of energy higher than 1 MeV.

f) DYMOKA

DYMOKA is a Molecular Dynamic code developed by C. Domain from EDF (e.g. [15]); it is written in C. For the building of RPV-1, its parallel version was used to simulate displacement (sub)-cascades in iron as well as the interactions between hardening defects and a screw dislocation. The selected EAM-type inter-atomic potentials are given in Table II.

Table II : references of EAM-interatomic potentials used to carry out simulations with DYMOKA and LAKIMOCA.

EAM-interatomic potentials	Reference
Fe-Fe	Ludwig et al. [16] ; Raulot [17]
Cu-Cu	Ludwig et al. [16]
Fe-Cu	Ludwig et al. [16]

g) LAKIMOCA

LAKIMOCA is a so-called Kinetic Monte Carlo code developed by C. Domain from EDF (e.g. [15]); it is written in C. For the building of RPV-1, LAKIMOCA was used to simulate the formation of nuclei of hardening defects during the short term evolution (some milliseconds) of the residual point defects left by displacement (sub)-cascades. It takes into account a large number of objects (solute atoms, impurities, point defects clusters, vacancy-

solute clusters, grain boundaries,…) and can be used with two models: Atomistic Kinetic Monte Carlo or Object Kinetic Monte Carlo according to the nature of the object considered as mobile. With the former, the interactions between atoms are described with EAM inter-atomic potentials (Table II); with the latter, these interactions are not explicitly described.

- The Atomic Kinetic Monte Carlo model considers the mobility of vacancies only. At each time step, one vacancy jumps to one of its nearest sites or is emitted from an object (vacancy clusters,…). The physical inputs of the model are the jump frequencies of vacancies depending on their local environment and the vacancy emission frequencies of the objects depending on their type and size. With this model, the current version of LAKIMOCA cannot simulate the fate of SIAs.

- The Object Kinetic Monte Carlo model takes into account the mobility of several types of objects: isolated point defects, point defect clusters, vacancies-solute clusters, solute precipitates… At each time step, one of these objects either moves of one inter-atomic distance or emits one element (point defect or solute atom). The physical inputs of the model are the jump and emission frequencies of the objects. Several parameters describing the simulated material like the migration energies of point defects, the binding energies of point defects with point defect clusters, the binding energy of Cu atoms with vacancies …. are also required.

Both models take into account the presence of sinks (dislocations, grain boundaries…) where point defects may disappear.

2.3 - Databases used in RPV-1

Some calculations required to simulate irradiation effects are extremely computer-time consuming. They cannot be performed in flexible versions of VTRs usable on PCs. For RPV-1, these calculations were carried out separately on powerful parallel computers (CRAY, clusters of PCs,…) and their results were stored in two databases integrated in the VTR :

- the “CASCADE” database, which contains the size distributions of nuclei of hardening defects produced by (sub)-cascades in Fe-Cu alloys. These data are used to prepare the source term of the Rate Theory code MFVISC.
- the “FORCE” database which contains the values of the pinning force exerted by the irradiation-induced defects on a screw dislocation. These data are used as input data of the DUPAIR code to calculate the irradiation-induced hardening.

During the simulation, the needed data are taken from these databases.

a) CASCADE

The database CASCADE provides the size distribution of nuclei of hardening defects formed within some milliseconds (short term evolution) by the surviving point defects of (sub)-cascades in Fe-Cu alloy. Its current version includes results for:

- 3 irradiation temperatures: T = 333, 423 and 573 K;
- 4 (sub)-cascade damage energies: T_{dam} = 10, 20, 30 and 40 keV;
- 5 free Cu contents in the matrix: Cu = 0.00, 0.03, 0.10, 0.20 and 0.30 at% Cu.

The main steps of the building of "CASCADE" are described hereafter and summarized in a more intelligible way in Figure 4:

- displacement (sub)-cascades corresponding to PKA damage energies of 10, 20, 30 or 40 keV were simulated by MD[2] in pure iron at T=600K (the results are supposed to be temperature independent in the range 100-600K). The simulations were stopped when the configuration of the surviving defects did not significantly evolve anymore (about 10 picoseconds of physical time). For each PKA energy, three simulations were performed with different initial incident directions of the PKA.
- the short term evolution (some milliseconds) of the surviving point defects left by the (sub)-cascades was simulated with LAKIMOCA in Fe-Cu alloys: in practice, copper is introduced in the simulation by replacing iron atoms by copper atoms in the simulation box containing the surviving defects. For each PKA initial condition (energy and direction), simulations were carried out at three temperatures (T=333, 423 or 573 K) and with four copper contents (Cu = 0.00, 0.03, 0.10, 0.20 and 0.30 at%). For each set of copper content, temperature and PKA initial energy, the simulation sequence was :
  - ✓ firstly the OKMC[3] was applied to follow the fate (diffusion, clustering,…) of the SIAs during few microseconds. The simulation was stopped when the configuration of SIAs did not significantly evolve anymore (most of them have left the simulation box; some may have merged to form clusters or may have been annihilated with surviving vacancies). The mobility of SIAs is much higher than that of vacancies, hence the vacancies remained almost immobile during the simulation. This OKMC simulation was carried out 1000 times with different initial random selection numbers.

[2] Molecular Dynamics
[3] Object Kinetic Monte Carlo

The final size distribution of nuclei of SIA loops was determined by averaging the size distributions provided by the 3000 simulations (simulations for 3 PKA initial directions x 1000 OKMC simulations).

✓ then, the AKMC[4] was used to follow the fate of the surviving vacancies during about some milliseconds. The simulation was stopped when the configuration of the vacancies and copper atoms did not significantly evolve anymore. For each set of conditions, this simulation was carried out only once, due to its high computing requirement.

The final size distribution of nuclei of vacancy-copper cluster, vacancy cluster and copper precipitate was determined by averaging the size distributions provided by the three simulations corresponding to the different PKA initial directions.

Finally, the size distribution of nuclei of hardening defects has been stored in "CASCADE" according to the irradiation temperature, PKA energy and copper content.

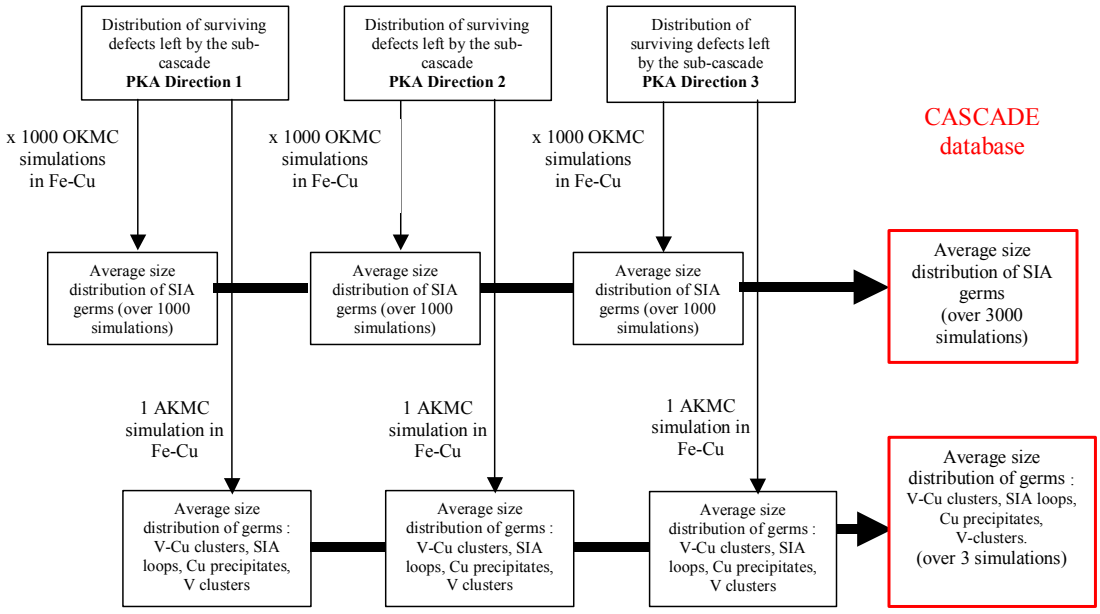

Figure 4: building of the CASCADE database - simulations carried out for a given set of irradiation temperature, PKA energy and Cu content.

[4] Atomic Kinetic Monte Carlo

b) FORCE

As already mentioned, FORCE contains the pinning forces exerted by the hardening defects (vacancy clusters, SIA clusters, pure copper precipitates and vacancy-copper clusters) on a screw dislocation. These forces have been determined from MD simulations with a "static approach". This means that the dislocation remains fixed in the simulation box (only displacements of atoms related to the box relaxation are allowed) and different positions of the defects as regard to the dislocation are considered (Figure 5a). The interaction energy between the defect and the dislocation is then recorded versus their separating distance (Figure 5b). The exact procedure as well as the way the forces were derived from the results are described in details in Chapter IV.

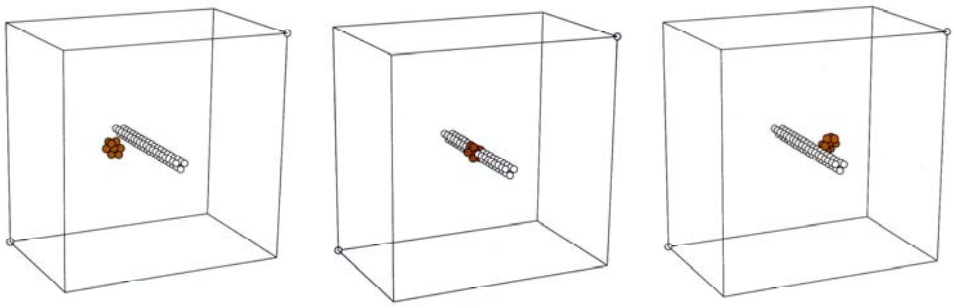

a)

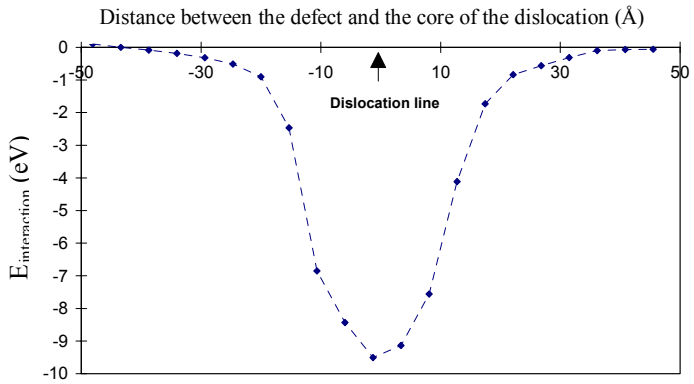

b)

Figure 5: static approach used to study the interaction between a screw dislocation and hardening defects with the Molecular Dynamics code DYMOKA [18].

a) three configurations of a 9 copper atoms precipitate and the screw dislocation;

b) variation of the interaction energy between a 400 copper-atoms precipitate and the screw dislocation, as a function of their separation distance.

III - Simulation steps of RPV-1

The simulation of irradiation effects with RPV-1 requires to activate the three modules presented in §2.1 of this Chapter. The corresponding calculation steps are described hereafter and illustrated in Figure 6 for a simulation carried out at 150°C with a neutron spectrum which is representative of an irradiation channel of the French reactor OSIRIS (composition of the irradiated steel: 0.1%Cu, 1.3 %Mn, 0.7 %Ni). This simulation has been carried out with the version 1.2.g of RPV-1.

3.1 - The "short term irradiation" module

step 1 : the PKA spectrum and the dpa rate are determined from the neutron spectrum with the code SPECMIN. As already mentioned, the effects of alloying elements and impurities on both quantities are negligible and consequently the simulation is carried out in pure iron (Figure 6a and b).

step 2 : the (sub)-cascade spectrum is determined from the PKA spectrum with the code INCAS. The effects of alloying elements and impurities on (sub)-cascade formation are also negligible and the simulation is consequently carried out in pure iron (Figure 6c). The INCAS simulation provides also the number of Frenkel pairs produced between the (sub)-cascades by time and volume units. As already mentioned, it is supposed that the corresponding vacancies are isolated and the SIAs distributed among the following nuclei: 60% are isolated, 20% are in clusters of size 2, 10% in clusters of size 3, 6% in clusters of size 4, 3% in clusters of size 5 and 11% in clusters if size 6.

step 3 : the size distributions of nuclei of SIA loops, copper precipitates, vacancy clusters and vacancy-copper atom clusters created by the (sub)-cascades are read in the CASCADE database as function of the damage energy in the (sub)-cascade, the irradiation temperature and the content of free copper in the solid solution. They are introduced as source terms in the rate theory code MFVISC according to the (sub)-cascade spectrum. To be more precise, let us consider the following example:

- the (sub)-cascade spectrum indicates that the irradiation introduces z cascades with a dissipated energy of 20 keV (corresponding to a damage energy of 15 keV) per time and volume units.
- CASCADE indicates that a 15 keV damage energy cascade creates an average of x_i SIA loop nuclei of size i and $y_{j,k}$ copper-vacancy nuclei containing j vacancies and k copper atoms,…
- then, $z.x_i$ SIA loop nuclei of size i, $z.y_{j,k}$ copper-vacancy nuclei containing j vacancies and k copper atoms,… are introduced as source

term in MFVISC per time and volume units. This operation is done for each group of (sub)-cascade damage energies.

If the free copper content of the steel is not one of those taken into account in CASCADE, the corresponding size distribution of nuclei is determined by interpolating between the two distributions related to the closest copper contents already existing in CASCADE. As an example: if for a 20 keV (sub)-cascade CASCADE indicates n_i and m_i nuclei of 3 SIAs when the copper contents are 0.03% and 0.1% respectively; then, for any copper content X such as 0.03% < X < 0.1%, the source term taken into account for nuclei of 3 SIAs is $\frac{1}{(0.1-0.03)}[m_i(X-0.03)+n_i(0.1-X)]$. The same interpolation is done for all the nuclei. The SIA clusters and mono vacancies produced between the sub-cascades are also added into the source term of MFVISC.

3.2 - The "long term irradiation" module

step 4: the simulation with MFVISC is carried out until the required irradiation time or number of dpa is reached. Results related to twenty intermediate times are also available.

step 5: at each MFVISC time step, the source term is adjusted in order to take into account the evolution of the microstructure :

- the residual free copper content in the matrix is re-calculated and the source term is modified accordingly;
- the probability for (sub)-cascades to occur at a distance of less than 1 nm of a pre-existing defect, and thus to have no effect, is calculated with the expression (1). To keep only "useful" (sub)-cascades, the (sub)-cascades spectra is modified: in each group of energy of the (sub)-cascade spectrum, the number of (sub)-cascades is multiplied by 1 – P(t).

3.3 - The "hardening" module

step 6: at the end of the MFVISC simulation and for the six last intermediate times, copper precipitates and vacancy-copper clusters are enriched in Mn and Ni atoms according to the results of DIFFG. The final size distribution of each type of irradiation-induced defects is then plotted on a graph. It can also be represented in a 3-D box by supposing that the defects are randomly

distributed (Figure 6e). The simulated evolution of the distribution of defects is described in paragraph IV of this Chapter.

step 7: following the introduction of Mn and Ni atoms in the simulations, the last six outputs of MFVISC are used as input for DUPAIR, which simulates the corresponding irradiation-induced increase of the yield stress for the selected temperature and deformation rate. The evolution of the increase of yield stress is plotted versus the irradiation time, total fluence, fluence higher than 1 MeV and number of dpa (Figure 6d). The concomitant evolution of the Charpy transition temperature can by determined from empirical correlations, e.g. : $\Delta TT \approx 0.68\ \Delta R_{P0.2}$ (at 20°C, without intergranular rupture) [19]. Comparison between experimental and simulated irradiation-induced increase of yield stress are given in Chapter V.

IV - Evolution of the irradiation-induced damage

This paragraph describes the simulated evolution of the irradiation-induced defect in a RPV steel (0.065%Cu-0.69%Mn-0.37%Ni) irradiated at 300°C with a neutron spectrum representative of a channel of HFIR ($\Phi_{E>1MeV} = 4.7\ 10^{12}$ n.cm^{-2}.s^{-1}).

The simulation was carried out with the version 1.2.g of RPV-1. For the sake of understanding, number densities of irradiation-induced defects have been plotted according to the following rules:

- number densities of SIA loops, vacancy clusters, copper precipitates and copper-rich precipitates are represented with solid lines;
- densities of copper-vacancy clusters are represented with dots. For a given number N of copper atoms in a cluster, the first dot of highest density corresponds to the density of clusters containing N copper atoms and 1 vacancy, the second one to the density of clusters containing N copper atoms and 2 vacancies, etc, ….

- **Cu-rich precipitates**: the simulated evolution of the distribution of copper-rich precipitates is plotted versus their copper content and the dose in Figure 7 a and b. This distribution becomes almost stable from a dose of about 10^{-3} dpa. In this configuration, the precipitates containing between 10 and 15 copper atoms have a number density of about 10^{24} m^{-3}. If they are supposed to be made of a core containing the copper atoms, mixed with iron atoms (20%), and surrounded by Ni an Mn, the core should have a radius of about 0.4 nm, which is a little bit smaller than the value of 0.5 nm measured by Pareige in Fe-Cu alloys [20]. With the Ni and Mn enrichment, the total radius of the precipitate is about 0.5 nm.

- **Vacancy-solute clusters**: the evolution of the distribution of the vacancy-solute clusters is plotted versus their copper content and the dose in Figure 7b and c. These clusters are getting more and more enriched in vacancies as the dose increases. Clusters containing between 10 and 15 copper atoms are in a number density of about 10^{24} m^{-3} for a dose of about 0.1 mdpa; they are also enriched in Ni and Mn (about 6 atoms). If , as observed experimentally, they contain about 85% of iron, their radius should be about 0.7 nm, which is also smaller than the radius generally determined experimentally (≈ 1.5 nm). However, the direct comparison is not straightforward since the simulation considered compact spherical defects while the structure of real defects is not really well known (ramifications, ..).

- **Vacancy clusters**: the number density and the average radius of the vacancy-clusters are increasing steadily as the dose grows.

- **SIA loops**: the behaviour observed for SIA loops is very similar to what is observed for vacancy clusters.

Thus, RPV-1 reproduces quite well the evolution of the irradiation-induced damage in term of types and number densities of defects. Even if a direct comparison is not straightforward, it seems that the size of simulated defects bearing copper is smaller than that determined experimentally.

V - Conclusion

This chapter presented the models and codes used to build RPV-1. Since the main focus of this work was to build a first tool, rather than a perfect tool, it was decided to use mostly existing codes and models in spite of their imperfections. It was intended that subsequent effort would lead to improve them or propose new ones. Nevertheless, two codes (INCAS and DUPAIR) had to be developed to complete the building of RPV-1. They are presented in the next paragraphs.

The codes were run with a standard parameterization which was not optimised in the framework of this thesis. The improvement of this parameterization is being done by the international community.

In its current state of development, RPV-1 reproduces quite well the evolution of the irradiation-induced damage in term of types and number densities of defects. Even if a direct comparison is not straightforward, it seems that the size of simulated defects bearing copper is smaller than that determined experimentally.

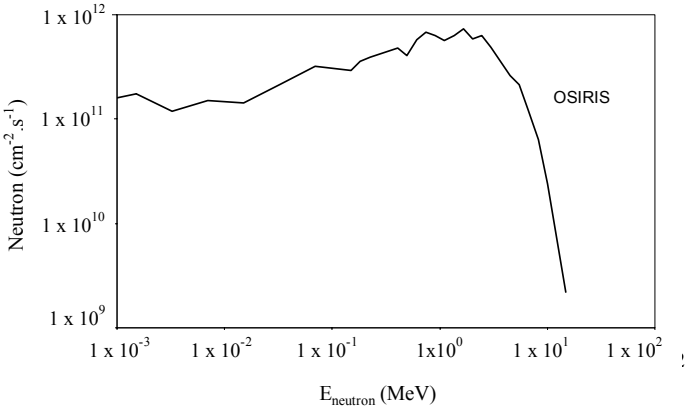

a)

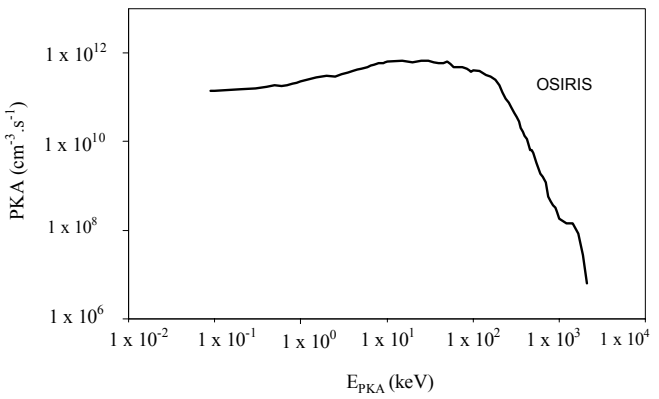

b)

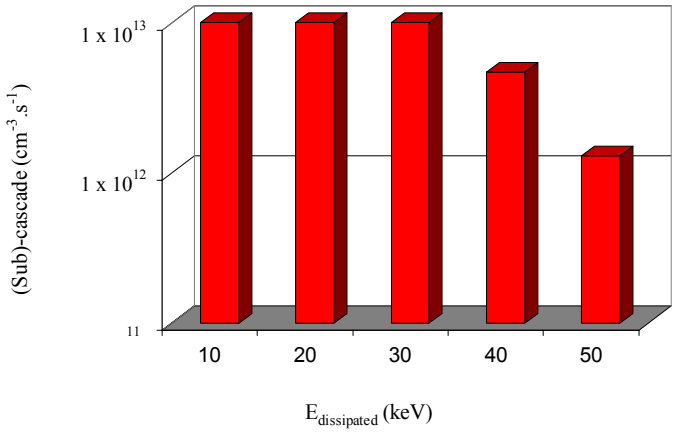

c)

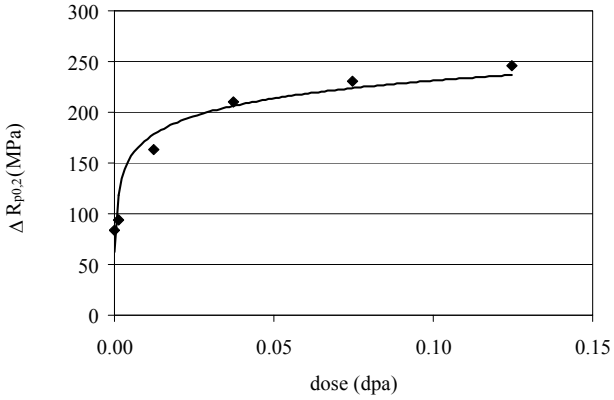

d)

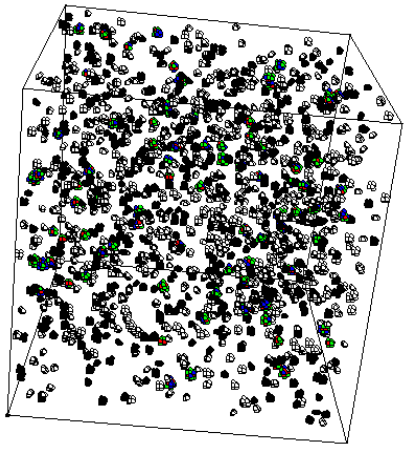

e)

Figure 6 : simulation of irradiation effects at 150°C in a 0.1%Cu-0.7%Ni-1.3%Mn steel with a neutron spectrum representative of one irradiation channel of the French reactor OSIRIS.

a) neutron spectrum;
b) PKA spectrum in pure iron;
c) (sub)-cascade spectrum in pure iron;
d) evolution of the yield stress increase versus the dose;
e) distribution of hardening defects for a dose of 0.1 dpa;
(vacancy: white, SIA: black; Cu: red, Mn: green, Ni: blue ; box size: 28.7 x 28.7 x 28.7 nm^3).

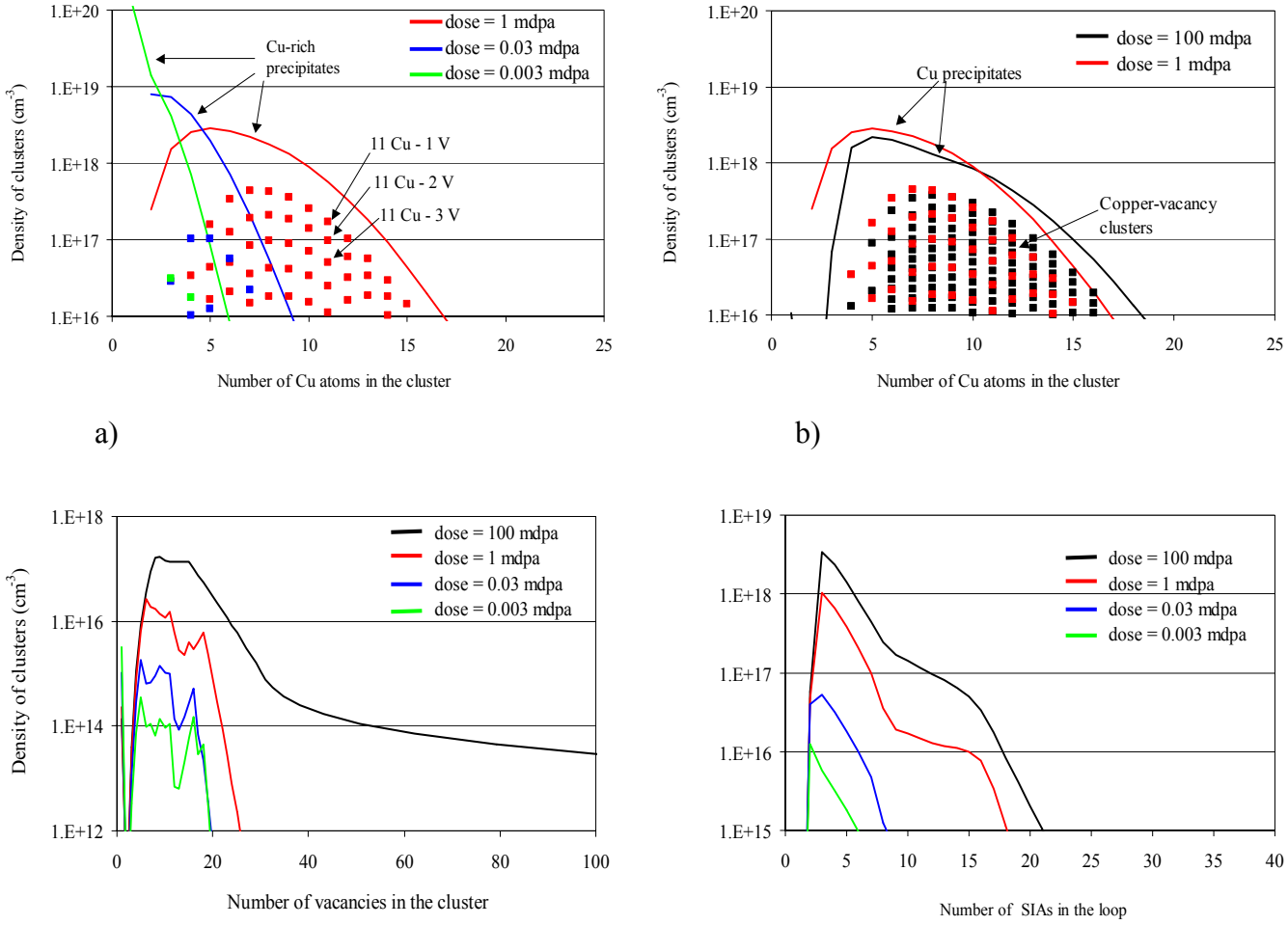

Figure 7: simulated evolution of the irradiation-induced defects in a RPV steel (0.065%Cu-0.69%Mn-0.37%Ni) irradiated at 300°C in a channel of HFIR.

a) Cu-rich precipitates and vacancy-solute clusters for doses of 3 10^{-6}, 3 10^{-3} and 10^{-3} dpa;
b) Cu-rich precipitates and vacancy-solute clusters for doses of 10^{-3} and 10^{-1}dpa;
c) Pure vacancy clusters for doses between 3 10^{-6} and 10^{-1}dpa;
d) SIA loops for doses between 3 10^{-6} and 10^{-1}dpa.;
The copper-rich precipitates and the vacancy-solute clusters are described as a function of their number of copper atoms.

References

1 Jumel, S., van-Duysen, J.C., J. Nucl. Mater., vol 340, (2005), p. 125.
2 Domain, C., Private communication.
3 Jumel, S., van Duysen, J.C., "Mechanisms Governing the Irradiation-Induced Embrittlement of Light Wate Reactor Pressure Vessel Steels" , IAEA, to be published.
4 Greenwood, L.R., J. Nucl. Mater., vol. 216, (1994), p. 29
5 Lindhard, J., Nielsen, V., Scharff, M., Det Kongelige Danske Videnskaberbernes Selskab Matematisk-fysiske Meddelelser, vol. 36, (1968), p.10.
6 Robinson, M.T. and Torrens I.M., Physical Review B, vol. 9 (12), (1974), p. 5008.
7 Jumel, S., van Duysen, J.C., "INCAS : an analytical model to describe displacement cascades", J. Nucl. Mater. , vol. 328, (2004).
8 Becquart, C.S., Domain, C., van Duysen, J.C., Raulot, J.M., J. Nucl. Mater., vol. 294, (2001), p. 274.
9 Hardouin-Duparc, A., Mointgeon, C., Smetniansky-de-Grande, N., Barbu, A., J. Nucl. Mater., vol. 302, (2002) p. 143.
10 Duwig, V., Ponçot, A., "Note théorique et informatique du code MFVIC", EDF Report, H-I23/2003/005, (2003).
11 Duwig, V., Jumel, S., EDF report, "Note théorique et informatique du code MFVISC" (2004).
12 Odette, G.R., Wirth, B.D., J. Nucl. Mater., vol. 251, (1997), p. 157.
13 Liu, C.L., Odette, G.R., Wirth, B.D., Lucas, G.E., Materials Science and Engineering, A238, (1997), p. 202.
14 Jumel, S., Domain, C., Van Duysen, J.C., "DUPAIR : a Foreman and Makin-type Code to Simulate Structural Hardening", EDF Internal Report, (2004).
15 Becquart, C.S., Decker, K.M., Domain, C., Ruste, J., Souffez, Y., Turbatte, J.C., van Duysen, J.C., "Massively parallel molecular dynamics simulations with EAM potentials ", Radiation Effects and Defects in Solids, vol. 142, (1997), p. 9.
16 Ludwig, M., Farkas, D., Pedraza, D., Schmauder, S., Modell. Simul. Mater. Sci. Eng., vol. 6, (1998), p.19.
17 Raulot, J.M., Master of Science Thesis, Université de Marne la Vallée, (1998).
18 Jumel, S., Ruste, J., Domain, C., van Duysen, J. C., submitted to J. Nucl. Mater.
19 Odette, G.R., He, M.Y., J. Nucl. Mater., vol. 283, (2000), p. 120-127.
20 Pareige, P., "Etude à la Sonde Atomique de l'Evolution Microstructurale sous Irradiation d'Alliages Ferritiques Fe-Cu et d'Aciers de Cuve de Réacteurs Nucléaires", Thèse de doctorat, Université de Rouen, (1994).

CHAPTER III

INCAS: INtegration of CAScades

The description of the code INCAS given in this chapter was extracted from a larger document published in Journal of Nuclear Materials [1].

One of the important steps in the building of RPV-1 is the description of the displacement cascades induced by neutrons. The required information are essentially the number of (sub)-cascades[1], the dissipated energy in each (sub)-cascade and the number of Frenkel pairs produced between the (sub)-cascades. Several simulation codes based on Binary Collision Approximation (e.g. Marlowe [2], Trim [3]) can already provide this information. However, their use presents some weaknesses for the aimed application, e.g.:

- the identification of (sub)-cascades is not straightforward. It is done by analysing the shape and size of the zones where point defects are produced [4] or measuring the local density of vacancies [5]. In both case, these post-treatments are rather complex.
- it is necessary to carry out a large number of simulations to get statistically-relevant information, which make the analysis even longer.

To get round these difficulties, a new analytical model based on the Binary Collision Approximation has been developed; it is called INCAS (INtegration of CAScades). INCAS relies on a simple definition of the sub-cascades and leads directly to average results. It has been set up to be used on pure elements; however, it can also be applied on diluted alloys (reactor pressure vessel steels,….) or alloys composed of atoms with close atomic number (stainless steels,…).

The objective of this section is to briefly describe the proposed model as well as some of its results and applications. Paragraph I reviews some elements about the displacement cascade phenomenon; in paragraph II, the proposed model and the corresponding equations are briefly presented. Paragraph III is dedicated to the determination of the required characteristics of displacement cascades and finally, in Paragraph IV, INCAS is applied on some examples and compared to other methods.

It should be mentioned that Sigmund et al. developed more than 30 years ago most of the ideas used in INCAS [6].

[1] The term (sub)-cascade covers a sub-cascade or a displacement cascade which cannot split into sub-cascades (PKA recoil energy < 40-50keV).

I - Displacement cascades

In displacements cascades, the slowing-down of moving atoms (PKAs, SKAs,...) is essentially controlled by electronic interactions in the high velocity range (e.g. E > 1 MeV for iron) and by atomic collisions in the low velocity range (e.g. E < 150 keV for iron) [7, 8, 9]. For LWR-type neutron spectra, displaced atoms have a maximal kinetic energy of about 3 MeV. This energy is high enough for both types of slowing-down processes to be considered. Thus, for each moving atom we have to consider both an electronic $(dE/dx)_e$ and a nuclear $(dE/dx)_n$ stopping power; these two functions characterise the energy losses per unit length of displacement. The total stopping power is given by :

$$(dE/dx)_{tot} = (dE/dx)_n + (dE/dx)_e \quad (1)$$

For the considered kinetic energy the ionisation effect is always very low and can be neglected in the quantification of $(dE/dx)_e$ and $(dE/dx)_n$.

1.1 - Electronic interactions

Since ionisation is negligible, it can be considered that the electronic interactions undergone by moving atoms mainly result from their collisions with the electrons of the other atoms (conduction electrons in the case of metals). Hence, the electronic stopping power can be expressed by the Lindhard-Scharff expression [8]:

$$\left(\frac{dE}{dx}\right)_e = NS_L(E) \text{ where } S_L(E) = kE^{1/2} \quad (2)$$

with $$k = \frac{8\pi e^2 a_0 Z_1^{7/6} Z_2}{(Z_1^{2/3} + Z_2^{2/3})^{3/4} M_1^{1/2} v_0} \quad (eV^{1/2}\ m^2) \quad (3)$$

where : Z_1 and Z_2 are respectively the atomic numbers of the moving and lattice-atoms,
M_1 is the atomic mass of the moving atom,
$a_0 = 5.3\ 10^{-11}$ m is the Bohr radius,
$v_0 = 2.2\ 10^6$ m/s is the Bohr velocity,

$e^2 = \frac{2.2\ \ 10^6 h}{2\pi}$ eV.m where h is the Planck constant = $4.135\ 10^{-15}$ eV.s.

Figure 1 shows the evolution of Lindhard-Scharff electronic stopping power versus the kinetic energy of an iron atom moving in pure iron.

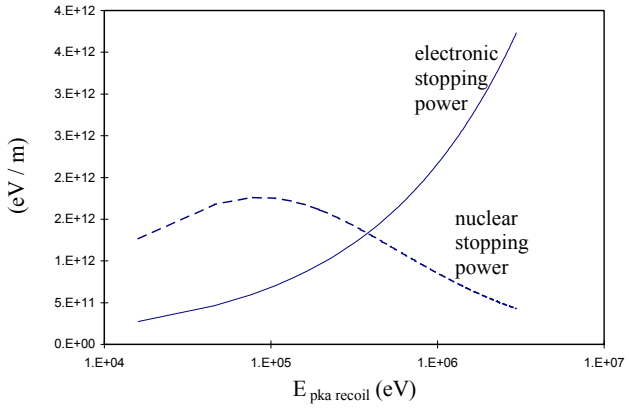

Figure 1: evolution of the nuclear and electronic stopping powers versus the kinetic energy of an iron atom moving in pure iron.

1.2 - Atomic collisions

Collisions between atoms can be treated in the framework of the binary collision approximation, i.e. they concern only two atoms at a time and do not depend on their environment. These collisions are also supposed to be elastic (the internal energy of each particle is the same before and after the collision) and not affected by the small equilibrium charge of moving atoms.

Let us consider a collision between an incident atom and a target atom. The incident atom has a kinetic energy E before the collision and E' after the collision. During this collision, it transfers an elastic energy E-E' to the target atom. If this energy is:

- higher than the displacement threshold energy E_d, then the hit atom leaves permanently its site with a kinetic energy T=E-E'-ε', where ε' is its binding energy (neglected in the present demonstration)
- lower than E_d, then the hit atom cannot leave its site.

The description of the atomic interactions can be made with the following quantities, expressed as a function of the energy of the incident atom:

- the differential cross-section for collision between the incident and target atoms: the expression proposed by Winterbon et al [9] and derived from a Thomas-Fermi type potential is used. It is expressed as:

$$d\Sigma(E) = \Sigma(E \rightarrow E')dE' = \left(\frac{\pi a^2}{2t^{3/2}}\right)\frac{\lambda t^{1/2-m}dt}{[1+(2\lambda t^{1-m})^q]^{1/q}} \qquad (4)$$

where :

$$t = E(E-E')\frac{M_2}{M_1}\left(\frac{a}{2Z_1Z_2e^2}\right)^2$$

$a = \frac{0.885 a_0}{(Z_1^{2/3} + Z_2^{2/3})^{1/2}}$ is the Lindhard screening radius,

$a_0 = 5.3\ 10^{-11}$ m is the Bohr radius,

Z_1 and Z_2 are respectively the atomic numbers of the incident and target atoms,

M_1 and M_2 are respectively the atomic masses of the incident and target atoms,

$e^2 = \frac{2.2\ \ 10^6 h}{2\pi}$ eV.m where h is the Planck constant $= 4.135\ 10^{-15}$ eV.s,

Considering the PKA energy range of this study (E ≤ 3 MeV), the parameters of expression (4) are those provided by Winterbon [10]:

$\lambda = 2.92 \qquad m = 0.191 \qquad q = 0.512$

- the total cross-section for collisions with a transferred energy higher than x:

$$\Gamma_x(E) = \int_0^{E-x} \Sigma(E \rightarrow E')\, dE' \qquad (5)$$

- the probability density for the incident atom to have a kinetic energy E' after a collision with a transferred energy higher than x:

$$\Pi_x(E \rightarrow E') = \frac{\Sigma(E \rightarrow E')}{\Gamma_x(E)} \qquad (6)$$

- the mean distance between two collisions of this type:

$$\beta_x(E) = \frac{1}{N\Gamma_x(E)} \qquad (7)$$

where N is the atomic density of the target material.

- the nuclear stopping power:

$$\left(\frac{dE}{dx}\right)_n = N\int_0^E \Sigma(E \rightarrow E')[E - E']dE' \qquad (8)$$

Figure 1 shows the evolution the nuclear stopping power versus the kinetic energy of an iron atom moving in pure iron.

All these equations are quite common for the "Binary Collision" community. In the next paragraph, they will be used to determine the main characteristics of displacement cascades.

II - Description of the proposed model

In order to characterise the displacement cascade induced by a PKA, the simplest approach consists in following it until it stops, and describing its interactions with matter along its trajectory (atomic collisions and electronic interactions). However, after a nuclear collision, the SKA may be more energetic than the PKA and hence induce most of the subsequent damage. To give a better description of a displacement cascade, it is preferable to follow the fate of the atom with the highest energy after each atomic collision.

To establish the required formalism, let us consider a PKA with an energy E just before a nuclear collision; after the collision we call [11]:

- PKA, the atom with the highest kinetic energy, noted E',
- SKA, the atom with the lowest kinetic energy, noted T = E-E'.

The two possible configurations that can happen during a collision are illustrated in Figure 2. For each of them, E' ≥ T, which leads to E' ≥ E/2 and T ≤ E/2. These inequalities will be utilized to define the limits of some integrals used in the model. With such conventions, the PKA moving in the material is not a single atom but a series of atoms. Along its trajectory, it successively corresponds to the atoms which leave the collision sites with the highest energy, i.e.: the PKA can be the same atom before and after the collision (case a in Figure 2) or can be exchanged with the lattice-atom (case b in Figure 2).

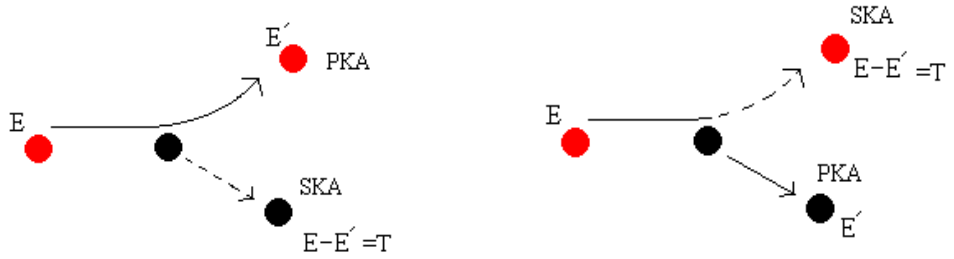

a) E-E'≤ E/2 b) E-E'≥ E/2

Figure 2: collision conventions where
a) the incident atom remains the PKA after the collision
b) the target becomes the PKA after the collision.

2.1 - Size of the damage zone

For collisions which create at least one stable Frenkel pair (the transferred energy has to be higher than E_d), we call "damage zone" the volume affected by the slowing-down of

the SKA and we characterise this volume by its spherical envelop (Figure 3). The sphere's diameter is given by the penetration depth of the SKA, calculated as follows: during its slowing-down, a SKA with an initial kinetic energy T_0 covers a distance $R(T_0) = \int_0^{T_0} \frac{dT}{(dT/dx)_{tot}}$. According to Sigmund [6], the penetration depth $R_P(T_0)$ is given by :

$$R_P(T_0) = 0.73R(T_0) = 0.73 \int_0^{T_0} \frac{dT}{(dT/dx)_{tot}} \quad (9)$$

Consequently, the mean size of the damage zone created during a collision with a transferred energy higher than E_d is obtained by averaging the possible SKA penetration depths:

$$R_{E_d}(E) = \int_{E_d}^{E/2} R_P(T) P_{E_d}(E,T) dT \quad (10)$$

The mean distance between these two damage zones can also be calculated by:

$$\lambda_{E_d}(E) = \frac{1}{N\Sigma_{E_d}(E)} \quad (11)$$

2.2 - Description of the (sub)-cascades

Damage zones are considered as sub-cascades if they fulfil the two following criteria (Figure 3):

- the dissipated energy in each of these zones is higher than a threshold value "a" ($T_0 \geq a$) [13]. We call "high transferred energy" damage zones, the damage zones respecting this criteria and "low transferred energy" damage zones the other ones. A priori, the value of "a" depends on the irradiated element;
- they do not overlap each other.

The determination of the parameter "a" deserves a particular attention since it is the only adjustable parameter of the proposed model. According to expression (10), the size of two successive "high transferred energy" damage zones (i.e. with a transferred energy higher than "a") is given by $R_a(E)$. On the same way, the distance between these damage zones is given by $\lambda_a(E)$ (see equation 11). Figure 4a and b show the evolution of $\lambda_a(E)$ and $R_a(E)$ as a function of the PKA energy (E) for two values of "a" (4 keV and 13 keV):

- with "a" = 4 keV, the curves have two intersections corresponding to PKA energies of 14 and 230 keV. Between these two energies, there is overlapping of the "high transferred energy" damage zones which, consequently, cannot be considered as sub-cascades.

- with “a” = 13 keV, λ_a is always higher than $R_a(E)$, thus, the “high transferred energy’ damage zones allowed for may be considered as sub-cascades. However, the two curves are rather distant which reveals that smaller sub-cascades are very likely neglected.

In a first approximation, we will consider that the “high transferred energy” damage zones corresponding to the sub-cascades are selected when the curves $R_a(E)$ and $\lambda_a(E)$ are tangent. For iron, that leads to “a” = a_{sub} = 8.3 keV (Figure 4c).

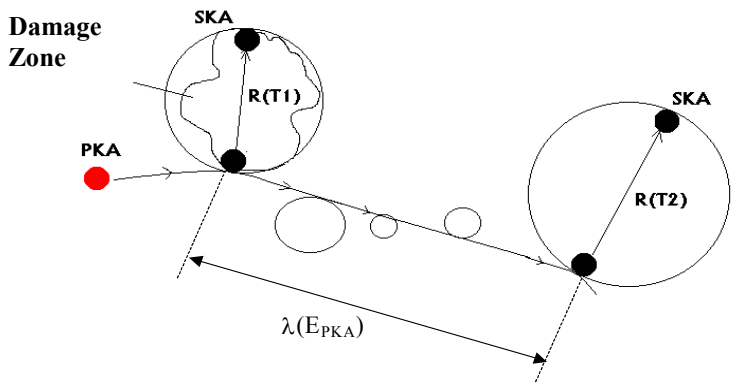

Figure 3: two "high transferred energy" damage zones separated by three "low transferred energy" (T1 and T2 ≥ a_{sub}). The "high transferred energy" damage zones are considered as being sub-cascades.

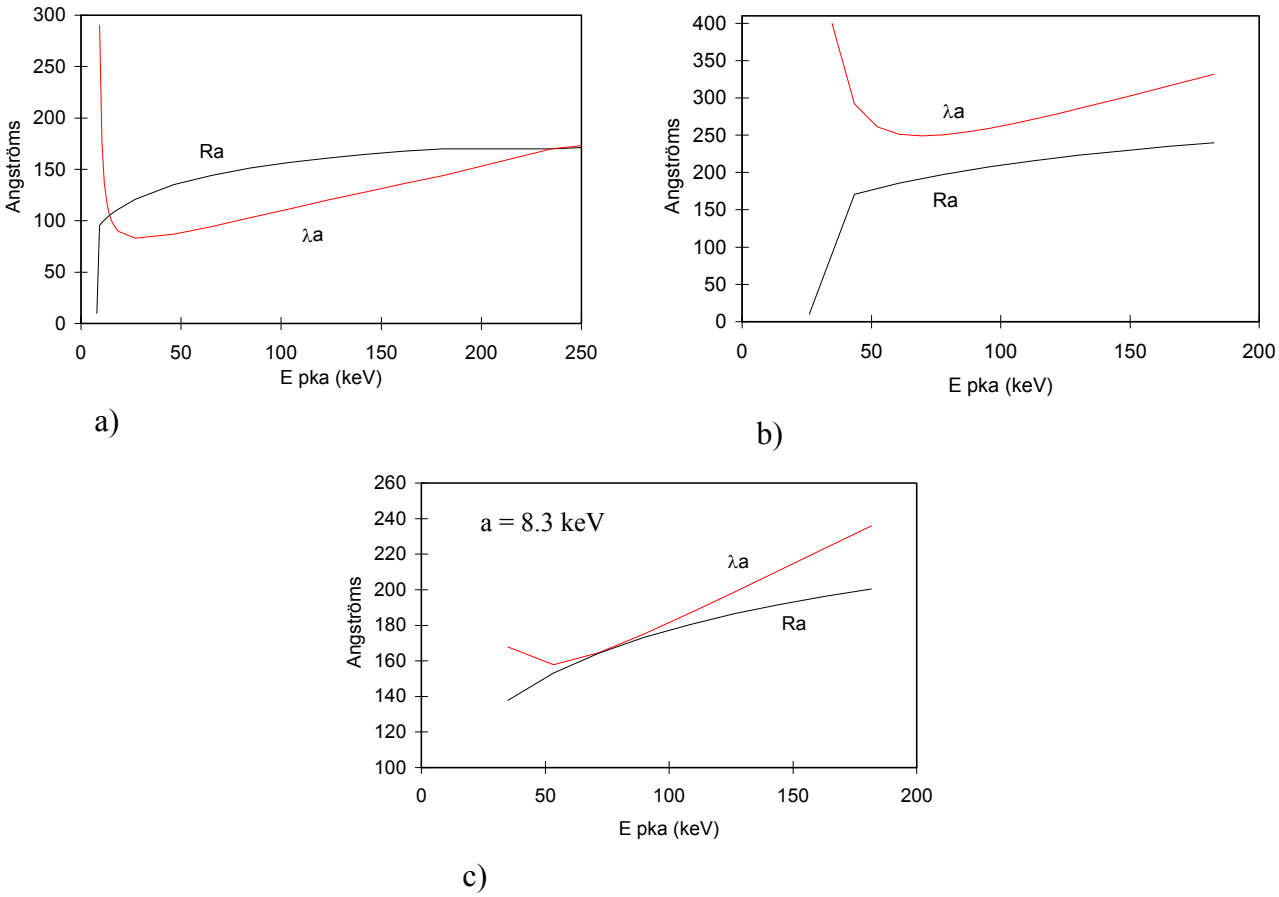

Figure 4: $R_a(E)$ and $\lambda_a(E)$ versus the PKA kinetic energy E and as a function of "a".

a) a = 4 keV; b) a = 13 keV; c) a = 8.3 keV.

III - Some characteristics of displacement cascades

Many characteristics of displacement cascades may be deduced from the model described in the previous section. The expressions required to determine the quantities used in RPV-1 are developed now, i.e. the mean energy dissipated in (sub)-cascades, the mean number of (sub)-cascades and the mean number of residual Frenkel pairs let between the sub-cascades, versus the PKA energy.

3.1 - Energy dissipated in (sub)-cascades

For a PKA with an initial energy E_0, the mean energy dissipated in a sub-cascade (recoil energy) is:

$$\Delta E_{sub}(E_0,E_1) = N\int_{E_1}^{E_0}\left[\frac{1}{\left(\frac{dE}{dx}\right)_{tot}}\Sigma_{a_{sub}}(E)\int_{a_{sub}}^{E/2}TP_{a_{sub}}(E,T)dT\right]dE \qquad (12)$$

where E_1 is the energy such as during its slowing-down between E_0 and E_1 the PKA produces one sub-cascade. E_1 can be deduced from the expression:

$$\int_{E_1}^{E_0} \frac{dE}{\left(\frac{dE}{dx}\right)_{tot}} N\Sigma_{a_{sub}}(E) = 1. \qquad (13)$$

Similarly, expressions can be derived to determine the mean energy losses of the PKA due to the formation of "low transferred energy" damage zones $[\Delta E_{<a_{sub}}(E_0, E_1)]$, electronic interactions $[\Delta E_e(E_0, E_1)]$ and collisions with energy transfers lower than E_d (sub-threshold collisions): $[\Delta E_{<Ed}(E_0, E_1)]$. All these quantities have to verify :

$$E_0\text{-}E_1 \approx \Delta E_{Sub}(E_0, E_1) + \Delta E_e(E_0, E_1) + \Delta E_{<a}(E_0, E_1) + \Delta E_{<Ed}(E_0, E_1) \qquad (14)$$

The same calculation is then carried out between E_1 and E_2, then between E_2 and E_3 etc, until the PKA has an energy lower than $2a_{sub}$. Below this value, the PKA cannot produce sub-cascade anymore.

3.2 - Number of (sub)-cascades produced by a PKA

The mean number of (sub)-cascades produced by a PKA with an initial energy E_0 is then given by :

- $N_{sub}(E_0) = 1 + N\int_{2a_{sub}}^{E_0} \frac{\Sigma_{a_{sub}}(E)}{\left(\frac{dE}{dx}\right)_{tot}} dE$, for $2a_{sub} \le E_0$ (15)

  The integral in this expression corresponds to the number of sub-cascades induced by the PKA during its slowing-down between E_0 and $2a_{sub}$; 1 is added to take into account the final damage zone induced by the PKA itself during its slowing-down between $2a_{sub}$ and E_d.

- $N_{sub}(E_0) = 1$, for $a_{sub} \le E_0 < 2a_{sub}$ (16)

  In this range of energy, the PKA cannot induce the formation of sub-cascades. However, we count 1 to take into account the damage zone produced by the PKA itself.

- $N_{sub}(E_0) = 0$, for $E_0 < a_{sub}$ (17)

SKAs may have a kinetic energy high enough for the induced damage zones to also split into sub-cascades; the latter have to be taken into account to determine the mean

total number of sub-cascades induced in the cascade. Such SKAs must have a kinetic energy higher than $2a_{sub}$. The total mean number of (sub)-cascades induced by a PKA is given by:

$$N_{sub}^{Total} = N_{sub}(E_0) + [N_{sub}(T_1) - 1)] + [N_{sub}(T_2) - 1] + [N_{sub}(T_3) - 1] + ... \quad (18)$$

where T_1, T_2, ... are the initial kinetic energies of SKAs (with $T_i \geq 2a_{sub}$) successively induced by the PKA during its slowing down.

3.3 - Number of residual Frenkel pairs left by "low transferred energy" damage zones

Along its trajectory, a PKA produces "low transferred energy" damage zones between the sub-cascades. After their recombination phase, each of these zones leaves a number $\nu(T_0)$ of Frenkel pairs in the material, where T_0 is the initial energy of the SKA producing the damage zone. The total number of Frenkel pairs, $N_{rF}(E_0)$, produced by a PKA during its slowing-down from an initial energy E_0 is given by:

- $$N_{rF}(E_0) \approx \int_{2a_{sub}}^{E_0} \left\{ \frac{1}{\left(\frac{dE}{dx}\right)_{tot}} N\Sigma_{<a_{sub}}(E) \int_{Ed}^{a_{sub}} \nu(T) P_{<a_{sub}}(E,T) dT \right\} dE \text{ , for } 2a_{sub} \leq E_0 \quad (19)$$

  This expression ignores the residual point defects left during the slowing-down of the PKA from $2a_{sub}$ to E_d. Indeed, these defects are formed in the final damage zone produced by the PKA which is counted as a "high transferred energy" damage zone [see expression (15)].

- $$N_{rF}(E_0) = 0 \qquad \text{for } a_{sub} \leq E_0 < 2a_{sub} \quad (20)$$

  In this range of initial energy, the damage zone produced by the PKA is counted as a sub-cascade (see expressions (16)); thus, there is no "low transferred energy" damage zone.

- $$N_{rF}(E_0) = \nu(E_0), \qquad \text{for } E_0 < a_{sub} \quad (21)$$

  In this range of initial energy, the PKA can only induce a "low transferred energy" damage zone.

For iron, several expressions have been proposed for $\nu(E)$ (e.g. [12, 13]) from Molecular Dynamics simulations; in INCAS, we used [13]:

$$\nu(E) = 2.977\ E^{0.95} \qquad (\text{for } E \leq 20 \text{ keV}) \quad (22)$$

In this expression, E is the damage energy (keV) dissipated in nuclear collisions (= recoil energy – energy losses in electronic interactions). However, since the PKAs or SKAs concerned by this expression have a low kinetic energy ($\leq a_{sub}$), we neglect their electronic interactions and consider that their kinetic energy (recoil energy) equals the damage energy.

As already mentioned, SKAs may have a kinetic energy high enough ($T_0 \geq 2a_{sub}$) so that the induced damage zones can split into sub-cascades; the "low transferred energy" damage zones formed between these sub-cascades also have to be taken into account. Hence, the mean total number of residual Frenkel pairs left by a PKA between the sub-cascades it has induced is given by :

$$N_{rF}^{Total} = N_{rF}(E_0) + N_{rF}(T_1) + N_{rF}(T_2) + N_{rF}(T_3) + ... \quad (23)$$

where T_1, T_2, ... are the initial kinetic energies of SKAs (with $T_i \geq 2a_{sub}$) successively induced by the PKA during its slowing down.

The residual point defects may be isolated or clustered in small nuclei. Their distribution depends on the irradiated materials. For example, statistical analysis of results of displacements cascades simulated by MD [14, 15, 16, 17] show that in iron, most of the residual vacancies are isolated. They also show [13, 17] that the distribution of the residual SIAs can be roughly estimated as follows: 60% are isolated, 20% are in clusters of size 2, 10% in clusters of size 3, 6% in clusters of size 4, 3% in clusters of size 5 and 11% in clusters of size 6.

IV - Applications

An experimental validation of INCAS could be carried out by measuring the number density of (sub)-cascades induced by neutron or ion irradiations in simple alloys. There were a lot of attempts to do so by measuring the number densities of point defect clusters induced by such irradiations. However, there is no direct correlation between the number density of (sub)-cascades and the number densities of point defect clusters. A better way could consist in measuring the number densities of irradiation-induced disordered zones in an ordered alloy (made of close atomic weight atoms). It was not possible to carry out this work during the presented thesis work. However, we checked that INCAS results are in good agreements with those obtained with other simulation approaches.

As an example of application, INCAS has been used to describe displacement cascades induced in pure elements: firstly iron, then aluminium, copper, niobium, silver, indium, barium, lanthanum, gold. Most of these elements have no special link with irradiation effects

in LWRs, they have been selected to make comparisons with other studies or to assess the effect of the atomic number, atomic mass or atomic density on the results. The following PKA energies were allowed for: 3, 2, 1, 0.5, 0.2 and 0.1 MeV.

4.1 - Iron

To describe displacement cascades in iron, we used a_{sub} = 8.3 keV as determined in section 2.2 of this Chapter. Table I gives the results obtained by following the series of calculations described in Paragraph III of this Chapter. When SKAs produce sub-cascades, their energy losses in electronic interactions, "low transferred energy" damage zones and sub-threshold collisions between the sub-cascades can be calculated as those of the PKA. These SKA energy losses are also given in Table I. From these calculations, it can be noticed that :

- SKAs produce sub-cascades when the PKA has an initial energy between 500 and 3000 keV;
- the mean energy dissipated in sub-cascades (recoil energy) ranges between 8 keV and 44 keV;
- as already noticed by Sigmund [13], the mean energy dissipated in "low energy transferred" damage zones between two sub-cascades is of the order of a_{sub};
- the mean energy losses in sub-threshold collisions ($T < E_d$) is always negligible;
- the total dissipated energies (last column) are in conformity with the energy losses of the PKA ($E_{i+1} - E_i$).

The mean number of (sub)-cascades is plotted versus the PKA energy in Figure 5. It can be noticed that the curve tends towards an asymptote as the PKA energy increases. This effect results from the increase of the electronic interactions which become predominant for kinetic energies higher than about 1 MeV (see Figure 1). It has been checked that for PKA energies lower than 100 keV, the trend curve is in agreement with results of displacements cascades simulated with MD [18].

4.2 - Effect of the irradiated element

As for iron, INCAS has been used to describe cascades in aluminium, copper, niobium, silver, indium, barium, lanthanum, gold. Some characteristics of these elements are given in Table II. The corresponding a_{sub} values are also given in Table II and plotted versus the atomic number and atomic density on Figure 6.

It appears that a_{sub} increases steadily with the atomic number (Figure 6a), but is not directly correlated to the atomic density (Figure 6b). The evolution of the mean number of (sub)-cascades versus the PKA recoil energy is given Figure 7. For a same PKA energy, the mean number of (sub)-cascades increases as the atomic number decreases. This trend is in conformity with other studies (e.g. [4, 5, 19]). Concerning Al, Cu, Ag and Au, the results obtained with INCAS can be quantitatively compared with those obtained by Heinisch and Singh with the Marlowe code [5]. Indeed, these authors developed a computational method to objectively identify sub-cascades simulated with Marlowe and thus have probably produced the most reliable results on this topic up to now. The evolutions of the mean number of (sub)-cascades versus the PKA recoil energy are compared in Figure 8. The results obtained with the two methods are in very good agreement.

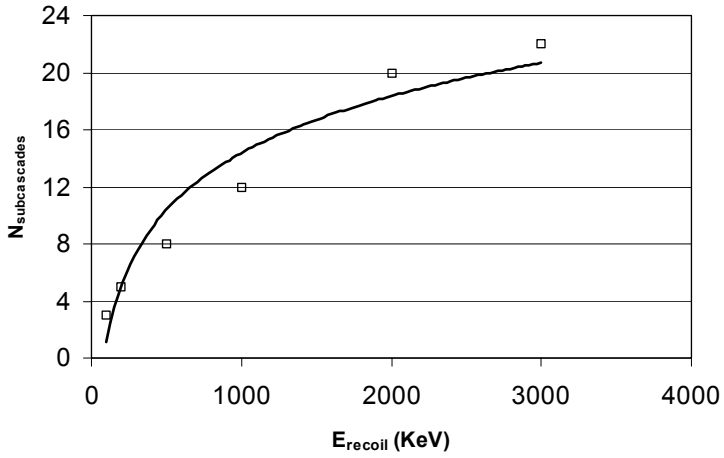

Figure 5: number of (sub)-cascades created in pure iron versus the kinetic energy of the PKA (dots given by the simulations and an associated regression curve).

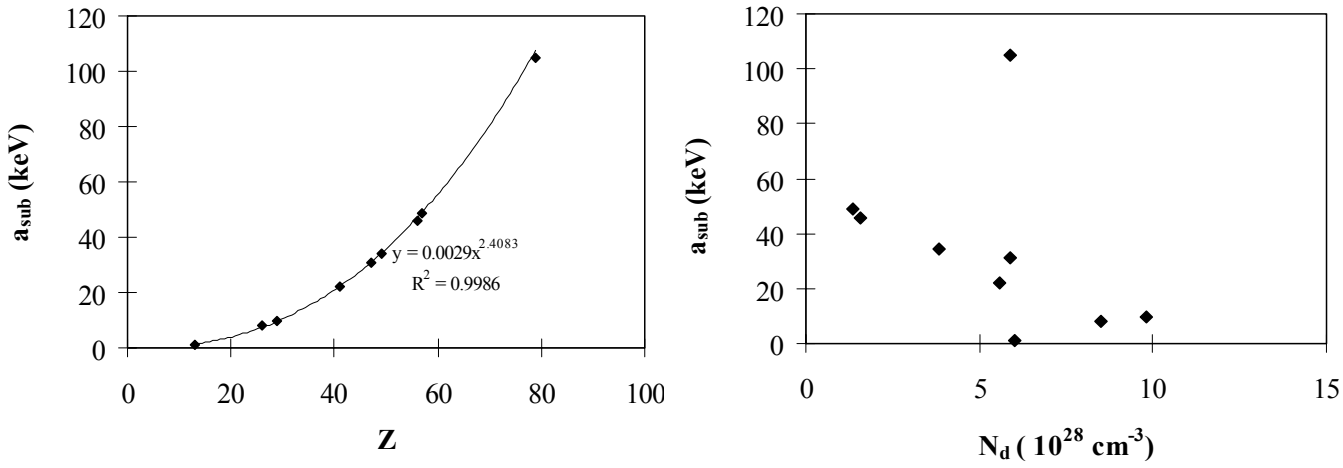

Figure 6: evolution of a_{sub} versus: (a) the atomic number Z and (b) the atomic density N_d of the irradiated element.

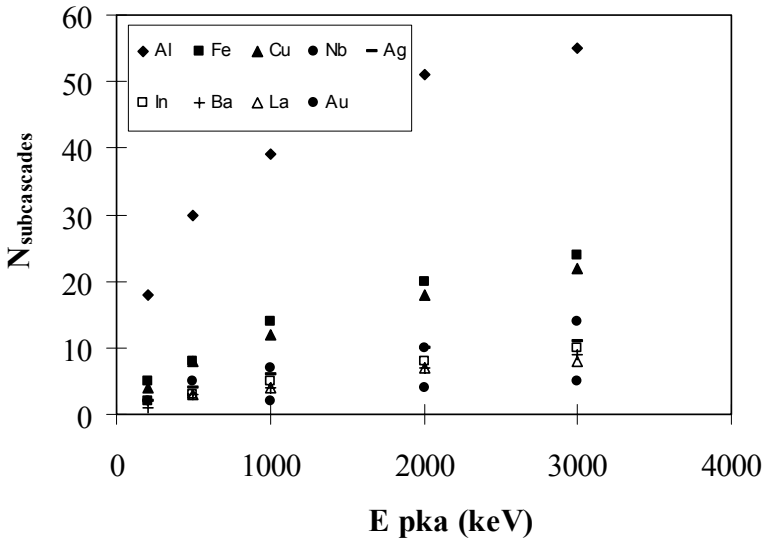

Figure 7: number of (sub)-cascades created in aluminium, copper, niobium, silver, indium, barium, lanthanum, gold versus the kinetic energy of the PKA.

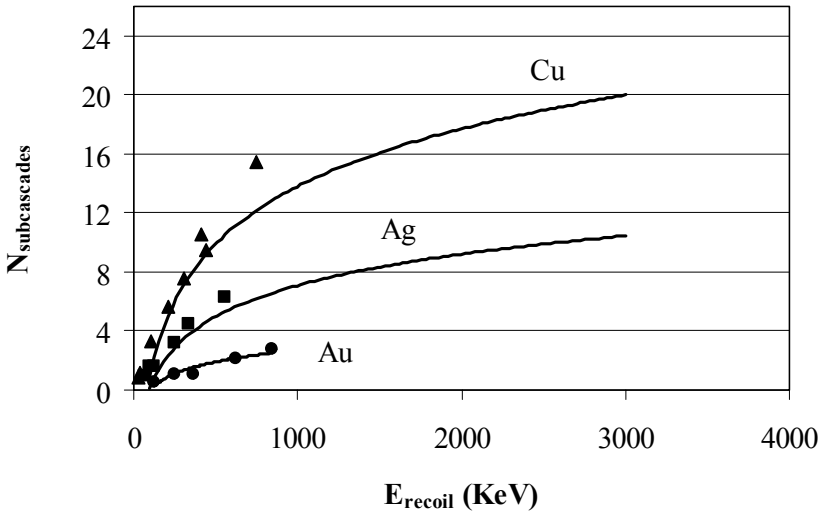

Figure 8: number of (sub)-cascades created in copper, silver ad gold (regression curves) versus the kinetic energy of the PKA; comparison with results obtained with the Marlowe code (dots) [6].

Table I: parameters describing displacement cascades (iron self-irradiation, a_{sub} = 8.3 keV).

* LTE : Low Transferred Energy.

** Total dissipated energy = $(\Delta E_{sub} + \Delta E_e + \Delta E_{<a} + \Delta E_{<E_d})_{PKA} + (\Delta E_{sub} + \Delta E_e + \Delta E_{<a} + \Delta E_{<E_d})_{SKA}$.

*** Range of PKA energy where the SKA has enough energy to produce 2 sub-cascades.

PKA initial energy (keV)	Number of (sub)-cascades	PKA energy range $E_{i+1} - E_i$ (keV)	Energy dissipated in sub-cascades ΔE_{sub} (keV)	Electronic losses ΔE_e (keV)	Losses in LTE* $\Delta E_{<a}$ (keV)	Losses in sub-threshold collisions $\Delta E_{<E_d}$ (keV)	Total dissipated energy**/$(E_{i+1}-E_i)$ (keV)
2000	20	2000 – 1613***	24 11	PKA : 320 SKA : 6	PKA : 15 SKA : 12	PKA : 0.7 SKA : 0.2	389/387
		1613 – 1306***	22 11	PKA : 243 SKA : 6	PKA : 14 SKA : 13	PKA : 0.6 SKA : 0.2	310/307
		1306 – 1058***	20 10	PKA : 186 SKA : 6	PKA : 13 SKA : 13	PKA : 0.5 SKA : 0.2	249/248
		1058 – 855***	18 9	PKA : 143 SKA : 6	PKA : 13 SKA : 14	PKA : 0.5 SKA : 0.2	204/203
		855 – 688***	16 8	PKA : 110 SKA : 6	PKA : 12 SKA : 14	PKA : 0.4 SKA : 0.2	167/167
		688 – 549	42	85	12	0.4	139/139
		549 – 433	40	64	11	0.4	115/116
		433 – 337	37	48	11	0.3	96/96
		337 – 256	34	36	11	0.3	81/81
		256 – 188	31	27	10	0.3	68/68
		188 – 132	29	19	10	0.2	58/56
		132 – 87	22	13	10	0.2	45/45
		87 – 50	17	9	10	0.2	36/37
		50 – 21	10	6	12	0.2	28/29
		21 – 0	21	-	-	-	21/21

Table II: some physical characteristics and a_{sub} values for aluminium, iron copper, niobium, silver, indium, barium, lanthanum, gold.

	Al	**Fe**	**Cu**	**Nb**	**Ag**	**In**	**Ba**	**La**	**Au**
Atomic number	13	26	29	41	47	49	56	57	79
Atomic mass	27	56	63	93	108	115	137	139	197
Atomic density (10^{28} cm^{-3})	6	8.5	9.8	5.56	5.9	3.82	1.57	1.33	5.9
Crystallographic structure	fcc	bcc	fcc	bcc	fcc	tetra	bcc	hcp	fcc
a_{sub} (keV)	1.3	8	9.8	22.1	31	34.2	46	48.7	105

V - Conclusion

INCAS is a code developed to complete the building of RPV-1. It enables to determine the mean number of (sub)-cascades induced by a PKA (depending on its energy) as well as the mean energy dissipated in each of them. The mean PKA energy dissipated in electronic interactions and sub-threshold collisions (collisions with lattice-atoms in which the transferred energy is lower than the displacement energy) are also available. In addition, INCAS gives the mean number of Frenkel pairs produced between the sub-cascades.

It was not possible to carry out an experimental validation of INCAS. However, it was checked that it results are in good agreement with those obtained by other approaches.

Finally, as first application, INCAS was applied to determine the (sub)-cascade spectra induced in pure iron by the neutron spectra in central channel of HIFR.

A computer code has been written in Fortran 77 by EDF to solve all the equations of INCAS. It can be used through a friendly interface and with the help of a user guide.

References

1 Jumel, S., van Duysen, J.C, J. Nucl. Mater., vol. 328, (2004), p. 151.
2 Robinson, M.T., Torrens, I.M., Physical Review B, vol. 9, (1974), p. 5008.
3 Ziegler, P.S., Biersack, J.P., Littmark, U., "The Stopping and Range of Ions in Solids", Eds Pergamon, New-York, (1985), p. 48.
4 Satoh, Y., Kojina, S., Yoshiie, T., Kiritani, M., J. Nucl. Mater., vol. 179-181, (1991), p. 901.
5 Heinisch, H., Singh, B. N., Phil. Mag. A, vol 67, N°2, (1993), p. 407.
6 Sigmund, P., Scheidler, G.P., Roth, G., "Spatial distribution of defects in cascades. Black spot defects in electron irradiated copper" , BNL report - 50083 (C-52), (1968).
7 Robinson, M.T., J. Nucl. Mater., vol. 216, (1994), p. 1.
8 Lindhard, J., V. Nielsen and M. Scharff, Det Kongelige Danske Videnskaberbernes Selskab Matematisk-fysiske Meddelelser, vol. 36, (1968), p.10.
9 Winterbon, K. B., Sigmund P. and Sanders, J. B., Mat. Fys. Medd. Dan. Vid. Selsk., vol. 37, N° 14, (1970).
10 Winterbon, K. B., Rad. Effects, vol. 13, (1972), p. 215.
11 Bethe, H., Zeits. F. Physik, vol. 76, (1932), p.293.
12 Bacon, D. J., Calder, A. F., Gao, F., Kapinos, V. G., Wooding, S. J., Nucl. Instrum. Metho. B, vol. 102, (1995), p. 49.
13 Becquart, C.S., Domain, C., van Duysen, J.C., Raulot, J. M., J. Nucl. Mater, vol. 294, (2001), p. 274.
14 Stoller, R.E., Greenwood, L.R., J. Nucl. Mater., vol. 271&272, (1999), p. 57.
15 Phythian, W. J., Stoller, R. E., Foreman, A. J. E., Calder, A. F., Bacon, D. J., J. Nucl. Mater., vol. 223, (1995), p. 245.
16 Stoller, R. E., Odette, G. R., Wirth, B. D., J. Nucl. Mater., vol. 251, (1997), p. 49.
17 Domain, C., Private communication.
18 Stoller, R.E., Private Communication.
19 Satoh, Y., Yoshiie, T., Kiritani, M., J. Nucl. Mater., vol. 191-194, (1992), p. 1101.

CHAPTER IV

DUPAIR: DURcissement Par IRradiation

This chapter presents the code DUPAIR and the database FORCE used in RPV-1 to simulate the irradiation-induced hardening. Its contains three main parts:

- the first one provides a description of the model and equations used to build DUPAIR;
- the second one describes the approach followed to determine the pinning force exerted by the irradiation-induced defects on a screw dislocation. These pinning forces are stored in the database FORCE and are used as inputs of DUPAIR;
- the last one presents the validation of the whole procedure set up to simulate the irradiation-induced hardening.

The last two parts were extracted from a larger document submitted for publication in Journal of Nuclear Materials [1].

I - Presentation of DUPAIR

1.1 Description of the model

DUPAIR is a so-called "Foreman and Makin-type" code (e.g. [2, 3]) aimed at assessing the increase of the resolved shear stress of a single crystal due to the presence of hardening defects. It consists in simulating the gliding of one single dislocation through an array of randomly distributed obstacles representing the defects. The dislocation cannot leave its slip plane (no cross-slip nor climbing). The resolved shear stress required to overcome each obstacle is calculated and the highest obtained value is the result of the simulation.

In order to set up the required system of equations, let us consider an isotropic medium (characterized by its shear modulus μ and Poisson ratio ν) containing one dislocation and an array of obstacles which can pin the dislocation with a pinning force $\vec{F}_p$ (Figure 1a). The dislocation is characterized by its Burgers vector $\vec{b} = \begin{pmatrix} b_1 \\ b_2 \\ 0 \end{pmatrix}$, its slip plane Oxy and a line tension $\vec{T}_i$ [4, 5, 6,] on

each point i of its line. The medium is submitted to a stress field $\overline{\overline{\sigma}} = \begin{pmatrix} 0 & 0 & \sigma_1 \\ 0 & 0 & \sigma_2 \\ \sigma_1 & \sigma_2 & 0 \end{pmatrix}$ which induces the stress $\vec{\sigma} = \begin{pmatrix} \sigma_1 \\ \sigma_2 \\ 0 \end{pmatrix}$ in the slip plane.

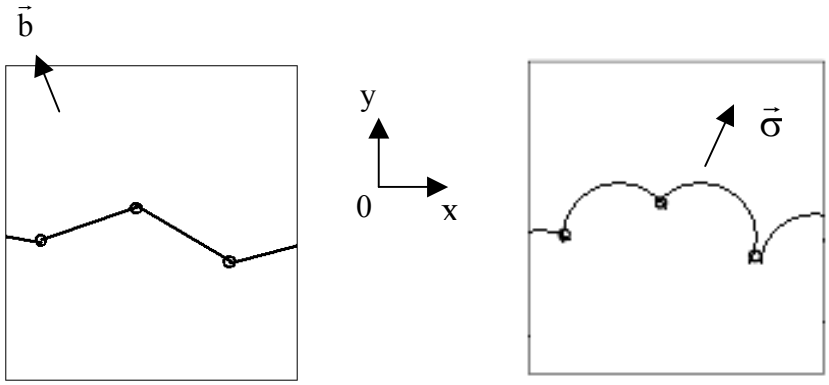

a) no stress b) with stress

Figure 1: sketch showing the effect of a stress field on a dislocation line pinned by obstacles ($\vec{b}$: Burgers vector).

a) Dislocation curvature

The applied stress field induces a force $d\vec{F}_i$ on each element $d\vec{l}_i$ of the dislocation line. This force, expressed by the Peach and Koehler formula: $d\vec{F}_i = (\overline{\overline{\sigma}}.\vec{b}) \wedge d\vec{l}_i$, is perpendicular to $d\vec{l}_i$ [7] and confers to it the shape of an arc of circle having for radius :

$$R_i = \frac{T_i}{(\sigma_1.b_1 + \sigma_2.b_2)} \qquad (1)$$

It results a curvature of the dislocation segments between each obstacles (figure 1b). The precise determination of this curvature requires the evaluation of the line tension T_i, at each point of the dislocation line.

In DUPAIR, the shape of the dislocation segments is determined in a simplified way. The line tension is considered to be constant along each segment and independent of the curvature, i.e: calculated for the straight configuration (without any applied stress). In the framework of this approximation, the dislocation segments bow according to an arc of a circle when the stress is applied (R_i = cte).

b) Dislocation line tension

Several models can be used to calculate the line tension of the dislocation segments, DUPAIR takes into account three of them. They are briefly described in the following paragraph, supposing spherical obstacles.

- **model 1** is the simplest one. It consists in supposing the line tension independent of its character (screw, edge or mix) and equal to $T = \frac{\mu b^2}{2}$ (e.g. [5]), where b is the length of the Burgers vector. It is the model used by Foreman et Makin to develop their code [2, 8].

- **model 2** is more realistic since it takes into account the character of the dislocation segments in their straight configuration (without any applied stress). It considers that the line tension is given by the Wit and Koehler's expression [4, 6]:

$$T(\theta) = \frac{\mu b^2}{4\pi}\left(\frac{1+\nu-3\nu\sin^2\theta}{1-\nu}\right)\ln\left(\frac{A}{r_0}\right) \qquad (2)$$

where r_0 is the dislocation core radius, θ is the angle between the straight dislocation segment and the Burgers vector, A is an outer cut-off distance. The parameter A approximately corresponds to the closest distance to a parallel dislocation of opposite sign [9]. Here, $A = L - r_1^P - r_2^P$, where L is the distance between the centers of the two pinning obstacles, r_1^P and r_2^P are the radii of these obstacles in the slipping plane. A priori model 2 is relevant for slight curvatures of the segments [8, 10].

- **model 3** is also based on the Wit and Koehler expression, in which the expression of A relies on that proposed by Bacon et al [11]: $A = \frac{1}{\frac{1}{2\min(r_1^p, r_2^p)} + \frac{1}{L - r_1^P - r_2^P}}$. A priori, this model is adequate not only for slight curvatures ($L - r_1^P - r_2^P << r_1^P + r_2^P$, so $A \approx L - r_1^P - r_2^P$), but also for strong curvatures (r_1^P and $r_2^P << L$, so $A \approx 2\min(r_1^p, r_2^p)$ [12]) where the segments on both sides of the obstacles attract each others. This attraction is equivalent to reducing the tension line as regard to the straight configuration.

c) Overcoming of obstacles

The bowed dislocation segments on each side of an obstacle exert a force on it. In DUPAIR, this force is calculated with the expression $\vec{F} = T(\theta_1).\vec{n}_1 + T(\theta_2).\vec{n}_2$ where $T_1(\theta_1)$ and

$T_2(\theta_2)$ are the line tensions, $\vec{n}_1$ and $\vec{n}_2$ the tangent to the dislocation segments, θ_1 and θ_2 the angles between the Burgers vector and $\vec{n}_1$ and $\vec{n}_2$ on both sides of the obstacle (Figure 2). $\vec{n}_1$ and $\vec{n}_2$, θ_1 and θ_2 are determined from the approximated curvatures of the segments given by expression 1.

As the applied stress grows, the curvatures of the segments, and hence $|\vec{F}|$, increase. In DUPAIR, two processes can lead the dislocation to overcome an obstacle:

- the unpinning process: as soon as $|\vec{F}|$ reaches the value of the pinning force F_p, the obstacle releases the dislocation.

- the bypassing process: such a configuration happens when the dislocation segments on both sides of the obstacle are getting in contact. It is the case when i) one of the segments reaches an instable position of ″Frank-Read″ type [13] or ii) when three successive obstacles along the dislocation line define an angle smaller than π, in this configuration, the segments can join for a stress lower than the Orowan stress.

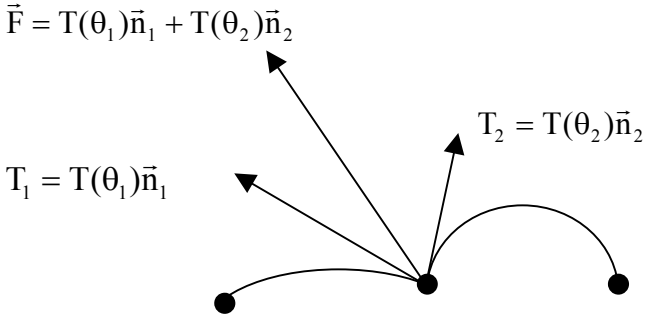

Figure 2: force equilibrium on an obstacle. $\vec{n}_1$ and $\vec{n}_2$ are the tangents to the dislocation segments; θ_1 and θ_2 the angles between these tangents and the Burgers vector; $T(\theta_1)$ and $T(\theta_2)$ the tension lines nearby the obstacle.

d) Complementary information and steps of the simulation

The crystal simulated with DUPAIR is tetragonal (length = width, and thickness = two times the largest obstacle radius), and periodic boundary conditions are applied along the Ox direction. At the beginning of the simulation the dislocation line is parallel to this direction.

The obstacles are randomly introduced in the simulated crystal according to their number density; attention is made to avoid overlapping. The total number of defects introduced in the crystal can be selected (the length of the crystal is adapted according to this number). Each type of obstacle is characterized by its number density, size and pinning force on the dislocation.

Starting with a configuration where no stress is applied, the simulation is run as follows:

1) calculation of the tension line of each dislocation segment between the obstacles (the segments are straight);
2) increase of the stress (the stress increase level can be chosen);
3) bowing of the dislocation segments according to the radii calculated with the expression (1). The bowing segments can be pinned by new obstacles;
4) calculation of the tension line of the curved segment on both sides of each pinning obstacles (as described in section 1.1.c);
5) checking for each pinning obstacle if the unpinning or bypassing conditions are reached;
6) in case neither unpinning nor bypassing happens, the stress is increased, etc;
7) as soon as an obstacle can be overcome, the stress is put back to zero, the overcome obstacle is suppressed and simulation restart at steps 1, etc;
8) the maximal resolved shear stress required to make the dislocation cross the simulation box is considered as the increase of the resolved shear stress due to the presence of the hardening defects.

1.2 - DUPAIR in RPV-1

The hypotheses made to use DUPAIR in RPV-1 are given in this section. They complement those presented in section 1.1 of this Chapter and in paragraph I of Chapter II:

- ✓ the plasticity of irradiated RPV steels is controlled by the gliding of screw dislocations. This hypothesis is verified for non-irradiated RPV-steels at temperatures up to 20°C but, to our knowledge, has never been checked after irradiation.
- ✓ screw dislocations are considered to slip on the $\{110\}$ planes of bcc iron (e.g. [14, 15, 16, 17]).

- ✓ the lattice friction (Peierls stress) exerted on the screw dislocation is supposed to be independent of the irradiation-induced defects.
- ✓ above room temperature, the dislocation can pass the smallest defects (some atoms or point defects) by thermally activated mechanisms; hence, these defects have no hardening effect [39].
- ✓ in copper-rich precipitates and vacancy-solute (Cu, Mn, Ni) clusters, Ni and Mn atoms are supposed to have the same "hardening effect" as copper atoms. Thus, for assessment of the hardening, these defects are considered to contain only one type of solute atoms: copper atoms.
- ✓ the increase of the macroscopic yield stress is calculated by multiplying the simulated increase of resolved shear stress by the Schmid's factor (≈ 3).

II Parameterization of DUPAIR : the database FORCE

2.1 - Literature survey

a) Strengthening effects of irradiation-induced defects

As already described in Chapter II, RPV-1 considers four types of hardening defects. The knowledge concerning their strengthening effect can be summarized in the following way (e.g. [18, 19]):

- **Copper-rich precipitates**: in first studies, copper-rich precipitates were described as "soft" spots that attract dislocations by lowering their elastic energy. The phenomenon was assumed to arise from the difference between their shear modulus and that of the surrounding matrix (e.g. [20, 21]) and was assessed in terms of the Russell and Brown's model [22]. Another explanation based on non-elastic effect within the dislocation core was put forward by Phythian [20] and then by Harry and Bacon [23]. From Molecular Dynamics (MD) simulations, they noticed that a dislocation may transform the bcc structure of copper precipitates embedded in α-iron into a fcc-like structure. More precisely, Harry and Bacon reported that the dislocation core of a screw dislocation spreads in the precipitate and transforms its structure, leading to a lower energy configuration. The larger the precipitate, the easier is the change of its structure from bcc to fcc. In both models, copper-rich precipitates are expected to pin the dislocation; their strengthening effect results from the difficulty to pull it out.

The role played by Mn, Ni and Si atoms in the strengthening effect of copper-rich precipitates has not been the object of dedicated studies yet. However, it was proposed that Mn and Ni could strongly contribute by forming an ordered structure [24].

- **Vacancy clusters**: vacancy clusters pin the dislocations through a mechanism initially analyzed by Coulomb and Friedel [25]. These authors considered that if the radius (r) of the cavity is much larger than the core radius of the dislocation, the binding energy (E_{Bind}) between the two defects can be approximated by the energy corresponding to the missing segment of dislocation line: $E_{Bind} = 2rE_{Line}$, where E_{Line} is the energy of the dislocation line per length unit ($E_{Line} \approx \frac{\mu b^2}{2}$); Osetsky et al. [26] recently confirmed this result by Molecular Dynamics simulations for an edge dislocation.

A more precise elastic calculation by Bullough and Newman [27] showed that the long range elastic interaction between a cavity and a screw dislocation is given by:

$$E = \frac{-5\mu b^2 r^2 (1-\nu)}{2\pi(7-5\nu)d^2} \qquad (3)$$

where d is the distance between both defects. For a dislocation tangential to the cavity, they approximated the interaction energy by using this expression with d = r (which leads to $E \approx \mu b^2 r/10$). They also estimated that the pinning force is at most $\mu b^2/5$ (when the slip plane is through the center of the cavity) and on average $\mu b^2/10$ ($\approx$ 3eV/nm).

- **Vacancy-solute atom (Cu, Mn, Ni, Si) clusters**: to our knowledge, no model has been developed to describe the strengthening effect of the vacancy-solute atom clusters. It can be assumed that it is a mix of several types of strengthening, depending on the solute and vacancy contents: vacancy cluster-type, solid solution-type or copper-precipitate-type.

- **Self-interstitial-atom loops**: the interactions between a dislocation loop and glissile dislocations can be classified in two types : “elastic” interaction and “reaction” interaction:

- *Elastic interaction:* the elastic interaction between a prismatic loop and a dislocation has been calculated by several authors in the approximation of isotropic elasticity (e.g. [28, 29, 30, 31, 32]). According to this approximation, there is no elastic interaction between a loop and a screw dislocation with a line perpendicular to the loop habit plane when the two Burgers vectors are parallel (e.g. [30]). Kroupa [28] calculated the elastic interaction when the two Burgers vectors are not parallel. He showed that the dislocation can be attracted or repulsed by the loop according to the relative position of both defects.

- *Reaction interaction:* when the loop and the dislocation intersect, they may combine and form a junction which can pin the dislocation (e.g. [33]). Friedel estimated that a junction led to a pinning force $F_{max} \approx \frac{\mu b^2}{4}$ [5], Kimura proposed

a value of $\frac{\mu b^2}{8}$ [34]. The junction may be unstable and evolve, which transform the loop: Foreman and Sharp [35] (generalizing a model proposed by Saada and Washburn [33]), described a mechanism where the loop combines with the dislocation to form a segment of the gliding dislocation (Figure 3a). Hirsch [36] proposed another mechanism where the junction evolves to form an helix on the dislocation (Figure 3b). Both mechanisms provide an explanation on the way gliding dislocations can sweep out loops and form cleared channel (e.g. [37]).

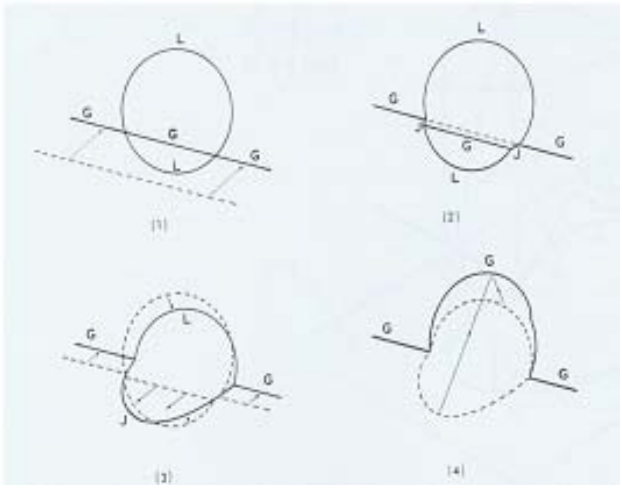

a) Foreman and Sharp mechanism [35]: when the loop (L) and the dislocation (G) are in contact, a junction dislocation (J) is formed. J and L rotate towards one another and combine to form a segment of the original dislocation G.

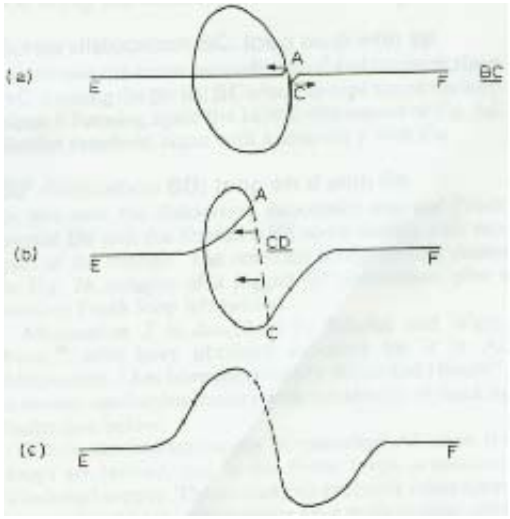

b) Hirch mechanisms [36]: a junction AC is formed at the point of contact. Nodes A and C are unstable and the dislocation segment AC sweeps across the plane of the loop which progressively turn into the glide plane of A. When AC reaches the opposite side a helix has been generated.

Figure 3: reaction interaction between a screw dislocation and a dislocation loop.

b) Thermal activation

At temperature above 0 K, dislocations can overcome irradiation-induced defects with the assistance of thermal energy. This thermal effect may result from a modification of the interaction mechanism between both defects or from the atomic fluctuations:

- **Modification of the interaction:** thermal energy can weaken the interaction between the dislocations and the defects. Osetsky and Bacon [38] observed by Molecular Dynamics simulations that the resolved shear stress required by an edge dislocation to overcome pure copper precipitates (100%Cu) and vacancy clusters decreases with increasing temperature. This effect has been attributed to a stronger tendency of dislocation climbing and a weaker tendency for bcc-to-fcc transformation in the precipitates as the temperature increases. It diminishes with decreasing size of the defects.

- **Atomic fluctuations:** as the temperature increases, the atomic fluctuations increase and may help the dislocation to overcome small defects. Such processes are characterized by a decreasing yield stress with increasing temperature up to a critical temperature (Tc) above which thermal fluctuations become so large that obstacles are overcome only by thermal energy. Tc is strain-rate-dependent, for attractive obstacles it can be assessed from the expression [5]:

$$kTc = \frac{E_{Binding}}{\ln(\nu n^2 \rho l^2 D^{-2} \dot{\varepsilon}^{-1})} \qquad (4)$$

Where : ρ : density of moving dislocations;

ν : Debye frequency ($\approx 10^{13}$ s^{-1});

b: Burgers vector ($2.48\ 10^{-10}$ m for iron);

$D = (\frac{2Tl^4}{E_{Binding}})^{\frac{1}{3}}$: effective inter-defect distance along the dislocation line resulting from the zig-zag shape of the dislocation ;

$l = (Nd)^{-0.5}$: average inter-defect distance;

N: number density of the defects;

d: diameter of the defects;

T: the dislocation line tension, $T \approx \frac{\mu b^2}{2}$;

μ: shear modulus ($8\ 10^{10}$ Pa);

$\dot{\varepsilon}$: strain rate.

With $\rho = 10^{14}$ m^{-2}, $N = 10^{25}$ m^{-3}, $d = 3\ 10^{-9}$ m, $\dot{\varepsilon} = 10^{-5}$ s^{-1}, this expression shows that Tc = 20°C leads to $E_{Bind} \approx -0.7$ eV.

For RPV steels, the effect of the overcoming of irradiation-induced defects by thermal activation is difficult to assess experimentally. Indeed, as noticed by Kirk et al [39], the temperature-dependence of the yield stress of such steels appears independent of the presence of the irradiation-induced damage (Figure 4) for temperature higher than –200°C. Kirk et al, suggested that the thermal-activated overcoming of irradiation-induced defects is screened by the strong temperature dependence imposed by the Peierls friction stress. The Kirk et al's observation is coherent with Bacon and Osetsky's simulation results [38] showing a low temperature dependence of the resolved shear stress required to overcome small copper precipitates (R ≤ 1nm) in iron at temperature higher than –173°C.

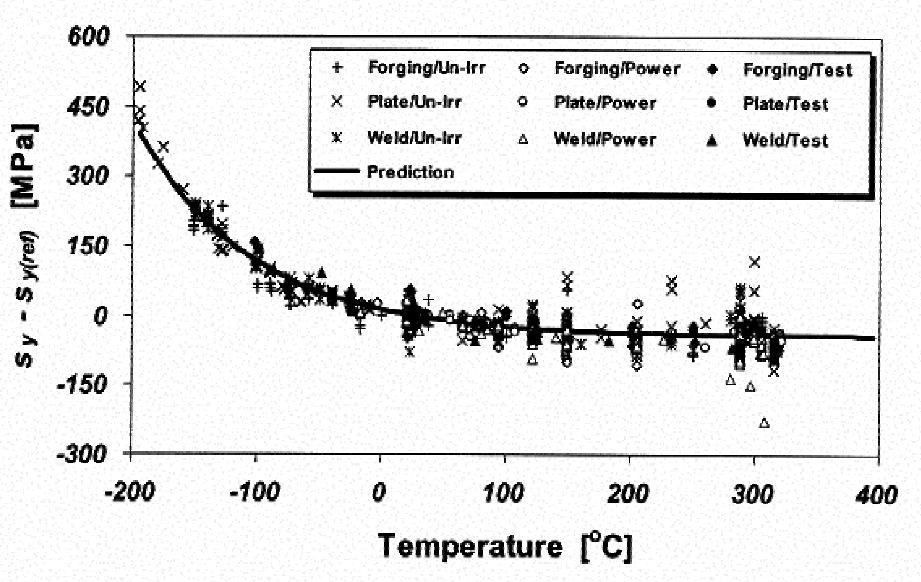

Sy : yield stress, Sy(ref) : yield stress at about 27°C.

Figure 4: temperature dependence of the yield stress of un-irradiated iron-based alloys [39].

2.2 - Simulation work carried out

To build RPV-1, the interaction between irradiation-induced defects and a screw dislocation were assessed by Molecular Dynamics simulations at 0 K using a "static approach". That means that the dislocation remains fixed in the simulated crystal (only displacements of atoms related to the crystal relaxation are allowed) and different positions of the defects as regard to the dislocation are considered. This approach can be summarized in the following way [23, 40, 41]:

- ✓ the screw dislocation is introduced at the center of the simulated crystal by applying the corresponding displacement field to the atoms;
- ✓ the studied defect is successively introduced at different distances from the core of the dislocation (one simulation per position of the defect);

- ✓ for each configuration, a quasi-Newton quenching is used to obtain equilibrium atomic arrangement: atomic velocities are rescaled every time step (≈ 10^{-15} second) to reach a steady energy of the system (at ± 0.01 eV) at the simulation temperature (T = 0 K). Typically, the static equilibrium arrangement is obtained after about 1000 simulation steps;
- ✓ the relaxed energy of the system is then recorded versus the distance between the core of the obstacle and the dislocation line. For a given configuration, the interaction energy between the two features is defined as the relaxed energy for the considered configuration minus the relaxed energy when they are largely separated (i.e. do not interact).

Four types of defects were considered: SIA loops, copper precipitates, copper-iron clusters and vacancy clusters. The simulations were carried out in α-Fe and α-binary Fe-Cu alloys with the Molecular Dynamics code DYMOKA developed by EDF [42]. The EAM-type Fe, Cu and Fe-Cu atomic potentials used for the simulations were developed by Ludwig et al [43] and hardened by EDF for simulation of displacement cascades. They lead to the following characteristics at 0 K:

- lattice parameter: a_0 = 0.287 nm for bcc Fe; a_0 = 0.288 nm for bcc Cu;
- interface energy between bcc copper and bcc iron: 318 and 121 mJ.m^{-2} on the {100} and {110} planes, respectively;
- interface energy of a spherical bcc copper precipitate of 2 nm radius: 207 mJ.m^{-2}.

The simulated crystal has its edges along the $[11\bar{2}]$, $[\bar{1}10]$ and [111] directions, and respectively 26, 22 and 26 elementary cells in the three directions. Usual boundary conditions for static studies of dislocation were applied: i.e. periodic along the dislocation line (direction [111]) and layers of fixed atoms along the surfaces perpendicular to the two other directions (width of these layers: $a_0\sqrt{2}$ and $a_0\sqrt{6}$ for surfaces perpendicular to $[11\bar{2}]$ and $[\bar{1}10]$, respectively).

- **Dislocation** : only a right-handed screw dislocation with Burgers vector b = 1/2 [111] was considered in the simulations. As observed by Suzuki et al [44], two distinct types of site are possible to place the elastic center of a screw dislocation in α-Fe [23]. The introduction of a right-handed screw dislocation in both types of site leads to different atomic configurations named "easy" and "hard" respectively. Suzuki et al [44] as well as Harry et al [23] noticed that the easy configuration is energetically more favorable and that a dislocation which is initially in a hard configuration may shift to the easy one. In the present study, the dislocation was always placed in an easy configuration. The site was selected in such a way that the dislocation was close to the central axis of the simulated crystal.

The dislocation was introduced by applying to the atoms the displacement field given by the isotropic elastic displacement field of a screw dislocation in α iron [31]. Following

established practice, the core structure of the dislocation was analyzed by plotting the [111] displacement difference between pairs of atoms with arrows drawn between them (to get the so-called differential displacement maps). As it is well known (e.g. [23, 45]), the atomic disregistry in the dislocation core appeared concentrated along the {110} planes of the [111] zone. The center of the dislocation can be regarded as the intersection of three stacking faults with displacement 1/6 [111]. On each of the three {110} planes, the large relative displacements occur only on one side of the dislocation, resulting in a three-fold symmetry.

In an isotropic crystal, the elastic line energy per unit length of a screw dislocation is given by:

$$E = \frac{\mu b^2}{4\pi} \ln\left(\frac{A}{r_c}\right) + E_c \qquad (5)$$

where μ, r_c and A are the shear modulus, the core radius and the outer cutoff distance, respectively (e.g. [4, 5]). To determine r_c, Molecular Dynamics simulations were carried out [46] so as to calculate the energy in different cylinders of radius A around the dislocation. The results leads to estimate $r_c \approx 8$ Å, which is larger than the radius of most of the considered neutron irradiation-induced defects.

- **SIA loops** : the dislocation loops were introduced in the simulated crystal by: i) making a selection of atoms on three successive {111} planes, these atoms were on filled hexagonal shells surrounding a central atom, and ii) by moving a copy of the selected atoms a distance + b/2 along the normal of the planes, and moving back the selected atoms a distance – b/2. After the introduction of the loop, the crystal was quenched. In their minimum energy configuration, the loops are made of $\langle 111 \rangle$ crowdions disposed on several (up to 7) parallel $\{111\}$ planes. They are more extended than perfect planar loops which should be located on only three planes. On a $\langle 111 \rangle$ projection, loops have a hexagonal shape, with edge parallel to $\langle 112 \rangle$ directions.

Among the four possible {111} habit planes, only two were considered here: (111), leading to a loop and a dislocation with parallel Burgers vectors, and $(11\bar{1})$ leading to an angle of about 70° between the Burgers vectors. For each plane, eight loops were taken into account (Table I). They were placed in the simulated crystal so that their center was on the slip plane of the dislocation. The relative positions were noted as shown in Figure 5 and about 20 values (0, positive and negative) of x were used for each loop.

Table I : SIA loops taken into account.

Number of SIAs in the loop	7	19	37	61	91	127	169	217
a* (nm)/b* (nm)	0.2/0.35	0.4/0.7	0.6/1.15	0.8/1.5	1.0/1.85	1.2/2.15	1.4/2.5	1.6/2.85

* a and b are defined as shown :

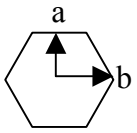

- <u>Copper-rich precipitates and vacancy-clusters</u> : as aforementioned, we consider that in copper-rich precipitates, Mn and Ni atoms have the same hardening effect as copper atoms. Consequently, only pure copper precipitates were taken into account to assess the pinning forces exerted by precipitates. Their radii, given in Table II, are lower than the critical radius of 3 nm from which the Cu structural transformation bcc structure→ 9R structure occurs [20, 47], they were thus expected to have a bcc structure. Some of the radii are also lower than the dislocation core radius. The relative positions of the defects, the dislocation line and the slip plane were noted as shown in Figure 6. For each defect, simulations were carried out with six positive values of y along $[1\bar{1}0]$; for each of these values, 20 values of x (0, positive and negative values) were used along $[11\bar{2}]$.

Simulations were also carried out with clusters (radius = 1.12 nm, 500 atoms) composed of an homogeneous mixture of Cu and Fe atoms. Ten copper contents were considered: 5, 10, 15, 20, 25, 30, 35, 50, 75 and 100%. Only the configuration where the slip plane is through the center (y = 0) of the cluster was allowed for (Figure 5).

Nine spherical vacancy clusters were also considered, their size is given in Table II. Some of them are also smaller than the dislocation core. The corresponding simulations were similar to those described for the copper precipitates.

Table II : copper precipitates and vacancy clusters considered in the simulations.

Number of Cu atoms or vacancies in the defect	10	50	100	200	500	750	1000	2000	3000	4000
Defect radius (nm)	0.30	0.52	0.65	0.82	1.12	1.28	1.41	1.77	2.03	2.23
Copper precipitates taken into account	-	X	X	X	X	-	X	X	X	X
Vacancy clusters taken into account	X	X	X	X	X	X	X	X	-	X

X: taken into account

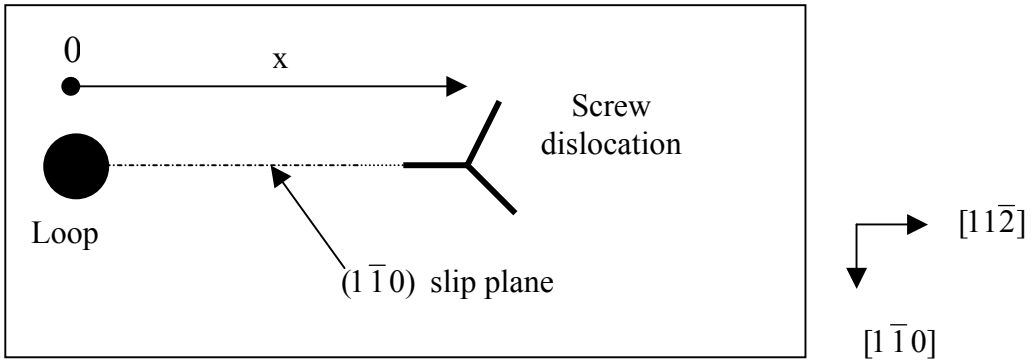

Figure 5: relative position of the dislocation loop (here on (111) habit plane) and the screw dislocation. The slip plane of the dislocation is through the center of the loop.

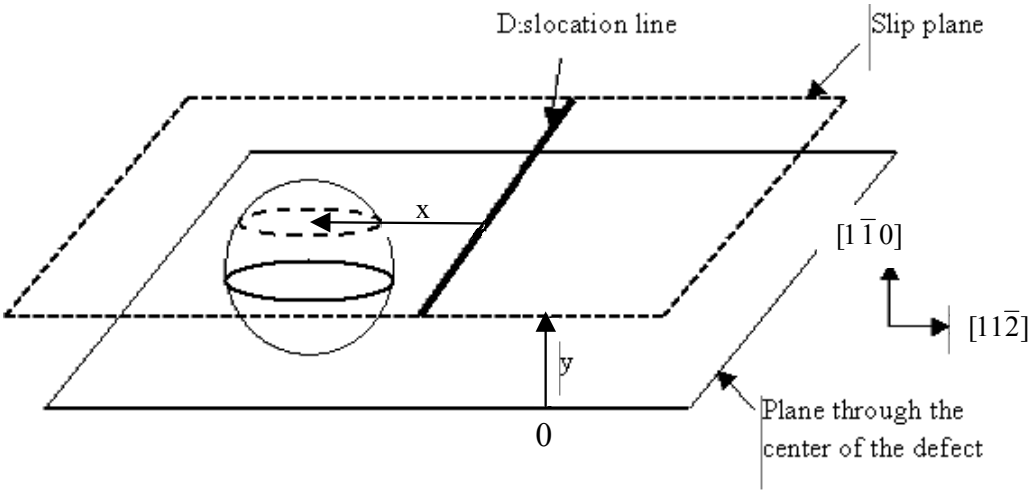

Figure 6: relatives positions of the dislocation line, slip plane and copper precipitate, vacancy clusters or copper-iron cluster.

2.3 - Results of the simulation

a) Interaction between the dislocation and SIA loops

When the dislocation is outside the SIA-loop, the interaction energy between the two defects is very small, except when they are almost in contact. In this configuration, they attract each other and have a "reaction"-type interaction. Two cases have to be considered:

- **Screw dislocation and SIA loops with parallel Burgers vectors**: when both defects have parallel Burgers vector, their combination leads to the transformation of the loop into an helix on the dislocation (Figure 7a and b), as foreseen by Hirsch (see Figure 3b). An example of "interaction energy versus distance" curve is given in Figure 8. In accordance with the isotropic elasticity calculations (see section 2.1.a), the interaction between both defects is almost negligible when they are not in contact.

- **Screw dislocation and SIA loops with non-parallel Burgers vectors**: when the Burgers vectors are non-parallel (angle 70°32'), the dislocation and the loop interact in two ways according to the size of the loop (Figure 7c):
  - ✓ small loops (≤ 19 SIAs) rotate to have parallel Burgers vector with the dislocation and combine with it, leading to the destruction of the loop and the formation of an helix on the dislocation.
  - ✓ large loops (>19 SIAs) form a junction with the dislocation along <311> directions.

b) Interaction between the dislocation and copper precipitates, copper-iron clusters and vacancy clusters

Figure 9 sketches (for a given value of y) typical curves giving the evolution of the interaction energy (E_{Inter}) versus the distance between the dislocation and a copper precipitate, a vacancy cluster or a copper-iron cluster. In spite the non-symmetry of the interaction configuration (for $x > 0$, the defect is facing one fractional dislocation; for $x < 0$, it is facing two fractional dislocations, see Figure 5), most of the obtained profiles are almost symmetrical. In all cases, E_{Inter} is minimal (hence the interaction is maximal) when the dislocation is within the obstacle, which means that the latter attracts and pins the dislocation. The zone corresponding to the minimal energy increases with the size of the obstacle. The binding energy (E_{Bind}) between the two features is defined as the minimal interaction energy.

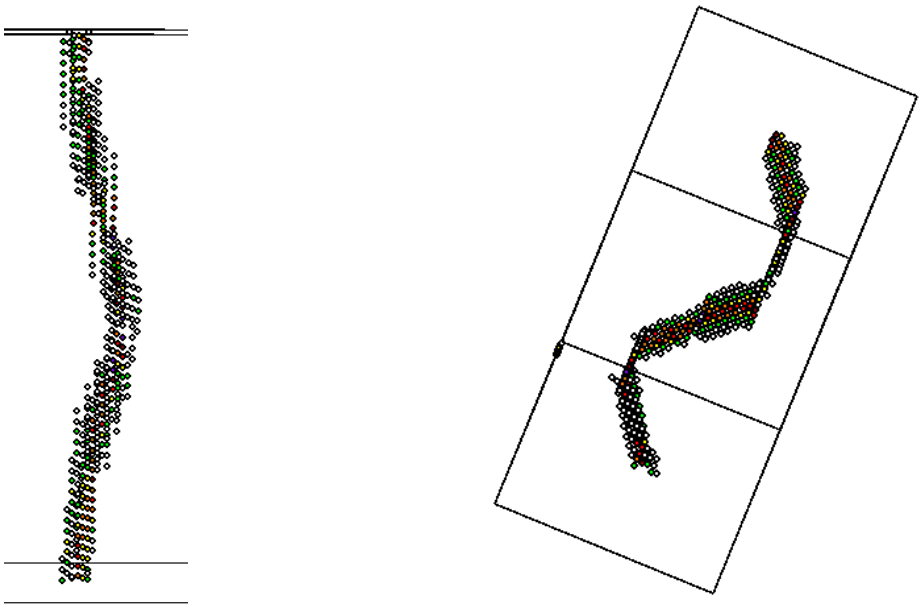

a) 19 SIA's loop b) 217 SIA's loop

Loop and dislocation with parallel Burgers vectors.

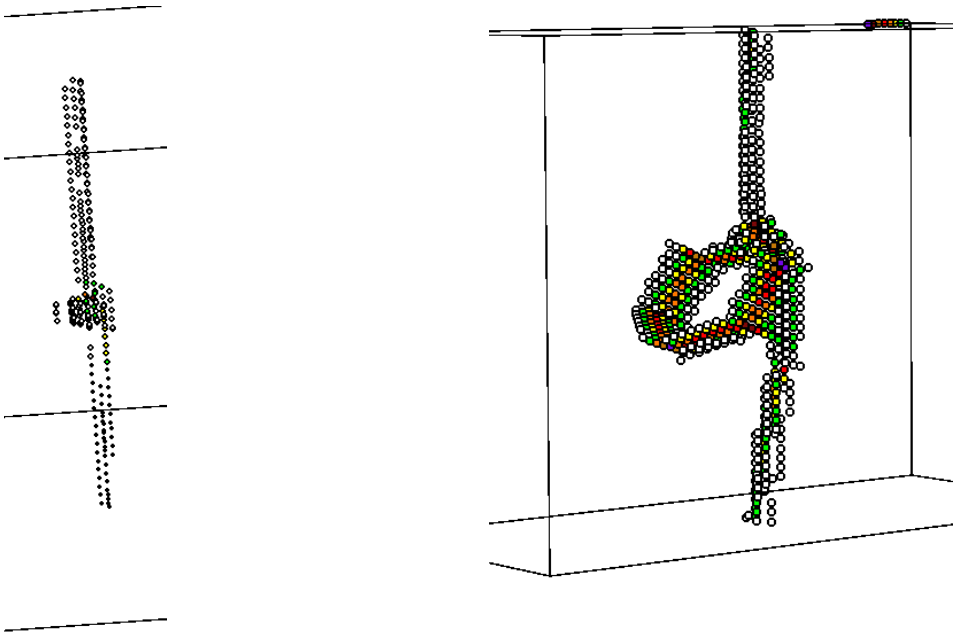

c) 19 SIA's loop d) 217 SIA's loop

Loops and dislocation with non parallel Burgers vector.

Figure 7: formation of an helix or a junction by the dislocation and the SIA loop.

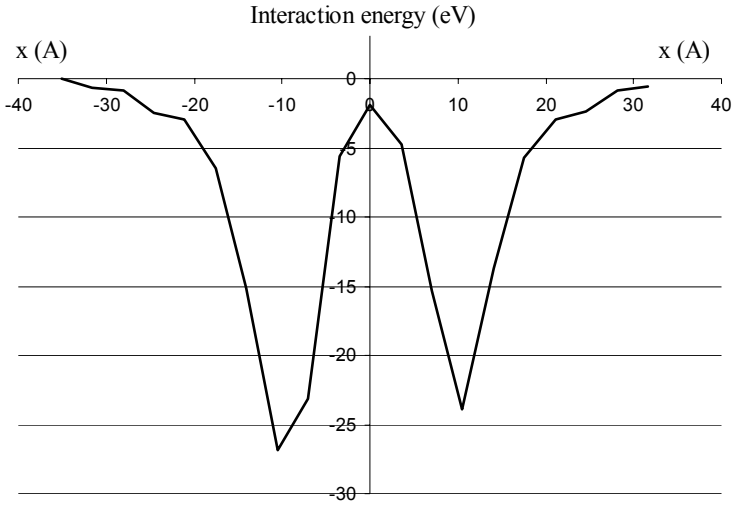

Figure 8: interaction between a screw dislocation and a loop containing 91 SIA's, with parallel Burgers vector.

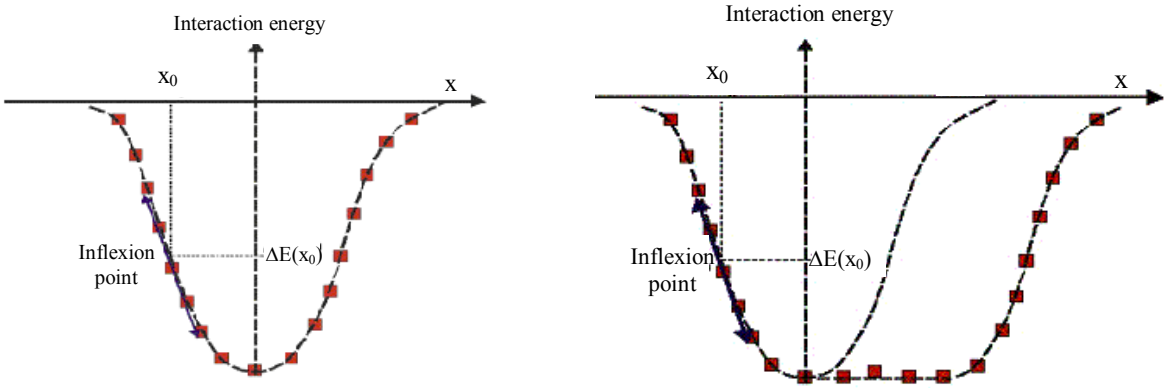

a) small defect b) large defects

Figure 9: sketch showing the evolution of the interaction energy versus the distance between the dislocation and a large or small copper precipitate, vacancy cluster or copper-iron cluster. A Gaussian curve was fitted on simulation points: all the points for smallest precipitates and only points on one side of the plateau of minimal interaction energy for the largest ones.

To determine the pinning forces exerted by the obstacles on the dislocation, Gaussian curves having the following expression were fitted on the simulation results:

$$E_{Inter}(r, x, y) = E_{Bind}(y,r) \exp[-\alpha(r, y)\, x^2] \quad (6)$$

where x and y are defined in Figure 6, r is the radius of the obstacle, α is a parameter depending on r and y. As shown in Figure 9, all the results were used for the small defects and only results corresponding to one side of the plateau of minimal energy were taken into account for the largest ones. The pinning force was defined as the value of the derivative of the Gaussian at the inflexion point ($x_0 = \sqrt{\frac{1}{2\alpha(r,y)}}$):

$$F = -2\alpha(r,y)\, x_0\, E_{Bind}(y,r) \exp[-\alpha(r, y)\, x_0^2] \quad (7)$$

- **<u>for the copper precipitates</u>:** all the studied pure copper precipitates have a bcc structure when they are not in contact with the dislocation. As observed by Harry et al [23], when the dislocation line is within a precipitate, its core spreads and modifies the precipitates bcc structure. Examples of curves "interaction energy-distance" are given in Figure 10 for two copper precipitates. In all cases, the minimal binding energy (hence the maximal interaction) and the maximal pinning force (F_{Pm}^{Cu}) are obtained when the slip plane is through the center of the precipitate (y = 0); the values are given in Table III. Analysis of the results shows that:

- the maximal pinning force and the precipitate radius are linked by the expression:

$$F_{Pm}^{Cu} \approx 0.05\, r^{1.17} \quad (eV/Å) \quad (8)$$

- the pinning force evolves with y according to the expression:

$$F_P^{Cu} \approx F_{pm}^{Cu} \exp(-0.843\, r^{-4.53}\, y^4) \quad (eV/Å) \quad (9)$$

The expression (9) is plotted in Figure 11a for several sizes of precipitates. Irradiation induced copper-rich precipitates ($r \leq 1.5$ nm) can be considered as rather weak obstacles.

Table III : minimal binding energy and maximal pinning force exerted by copper precipitates on a screw dislocation (y=0).

Number of Cu atoms in the precipitate	50	100	200	500	750	1000	2000	3000
Radius of the precipitate (nm)	0.52	0.65	0.82	1.12	1.28	1.41	1.72	2.03
Minimal binding energy (eV)	-2.27	-4.2	-4.8	-10	-11.6	-14.5	-21	-27
Maximal pinning force : F_{Pm}^{Cu} (eV/Å)	0.34	0.45	0.60	0.85	1	1.12	1.46	1.71

- **for the copper-iron precipitates:** examples of "interaction energy versus distance" curves are given in Figure 12. The binding energies and the pinning forces are given in Table IV. Analysis of the results showed that the pinning force evolve linearly with the copper content in the cluster according to the following expression:

$$F_{Pm}^{Cu-Fe} \approx 0.013[\%Cu] \qquad (eV/\text{Å}) \qquad (10)$$

This expression is obtained for y = 0, but it can be supposed that a linear relation between the pinning force and the copper content can also be applied for y ≠ 0.

Table IV: minimal binding energy and maximal pinning force exerted by iron-copper clusters (r = 1.12 nm, 500 atomic sites) on a screw dislocation (y=0).

Percentage of Cu in the cluster (%)	5	10	15	20	25	30	35	50	75	100
Minimal binding energy (eV)	-0.9	-1.6	-3.1	-3.6	-3.9	-4.3	-4.9	-4.7	-7.2	-9.9
Maximal pinning force (eV/Å)	0.08	0.10	0.18	0.32	0.33	0.49	0.57	0.515	0.83	1.09

- **for the vacancy clusters**: examples of "interaction energy-distance" curves are given in Figure 13 for two vacancy clusters. In all cases, the minimal binding energy (hence the maximal interaction) and maximal pinning force are obtained when the slip plane is through the center of the cluster (y = 0); the values are given Table V. Analysis of the results shows that:
  - the maximal pinning force F_{Pm}^{Va} and the cluster radius are linked by the expression:

$$F_{Pm}^{Va} \approx 0.0448\, r^{1.23} \qquad (eV/\text{Å}) \qquad (11)$$

  - the pinning force evolves with y according to the expression:

$$F_{P}^{Va} \approx F_{pm}^{Va} \exp\left(-0.219\, r^{-1.74} y^{2}\right) \qquad (eV/\text{Å}) \qquad (12)$$

The expression (12) is plotted in Figure 11b for several cluster sizes. It can be noticed that results are quite similar with those obtained for copper precipitates. For the clusters containing less than about 100 vacancies, the pinning forces are in agreement with that proposed by Bullough and Newman (see section 2.1). Irradiation-induced vacancy clusters (r ≤ 0.5 nm) can also be considered as rather weak obstacles.

Table V: minimal binding energy and maximal pinning force exerted by vacancy clusters on a screw dislocation (y=0).

Number of vacancies in the cluster	10	50	100	200	500	1000	2000	4000
Radius of the cluster (nm)	0.30	0.52	0.65	0.82	1.12	1.41	1.78	2.03
Minimal binding energy (eV)	-1.2	-2.3	-4	-6	-8.5	-12.4	-16	-24
Maximal pinning force : F_{Pm}^{Va} (eV/Å)	0.17	0.32	0.43	0.55	0.78	1.03	1.35	1.77

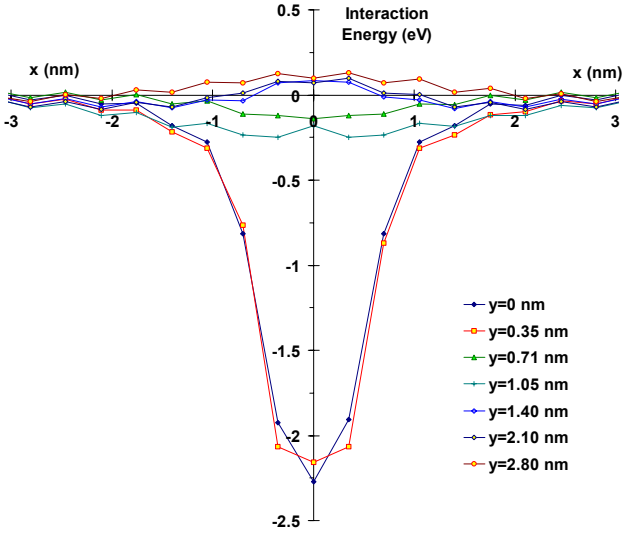

a) copper precipitate containing 50 atoms

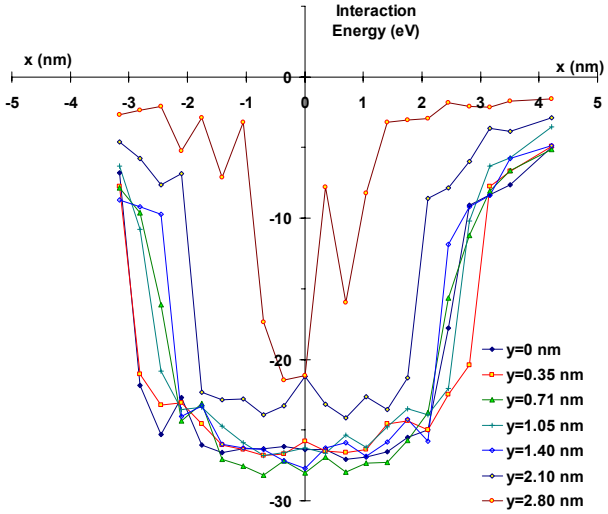

b) copper precipitate containing 3000 atoms

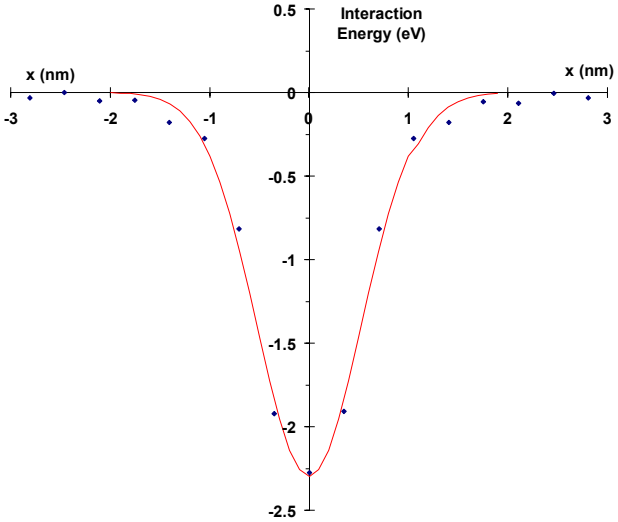

c) copper precipitate containing 50 atoms

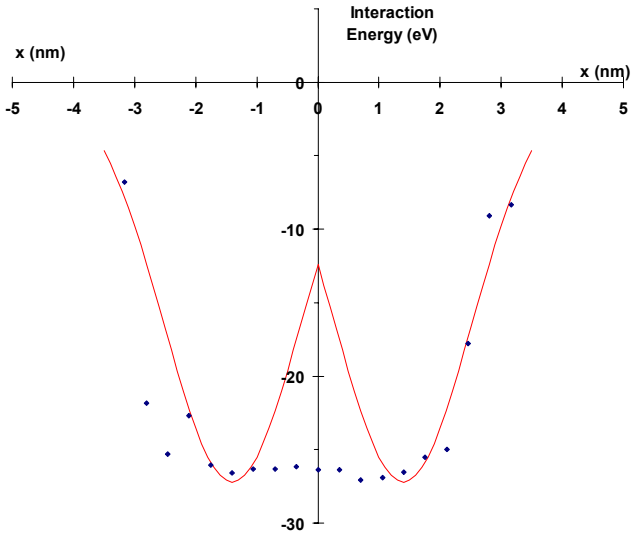

d) copper precipitate containing 3000 atoms

Figure 10: examples of results obtained for the copper precipitates (x and y are defined in Figure 6):

- a and c : Curves “interaction energy versus distance”;
- c and d : Gaussian curves fitted on simulation results obtained with y = 0.

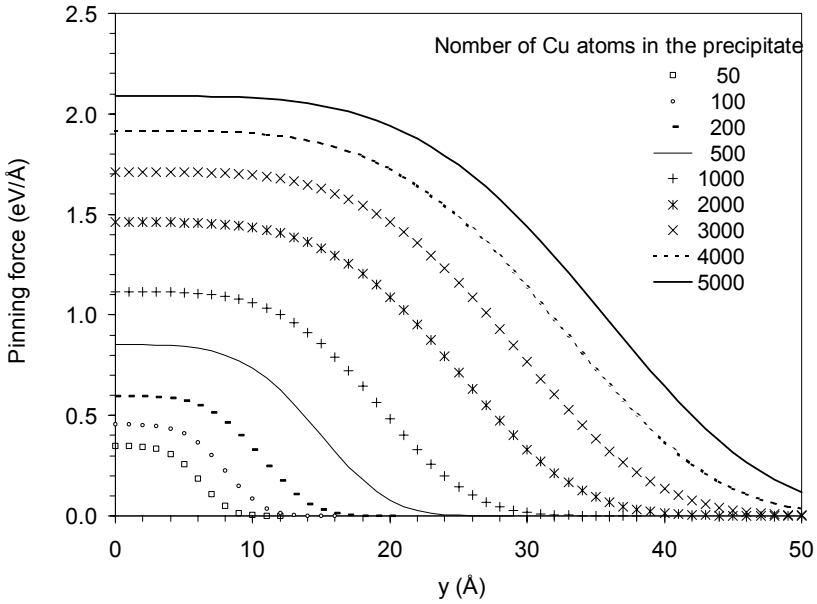

a) copper precipitates

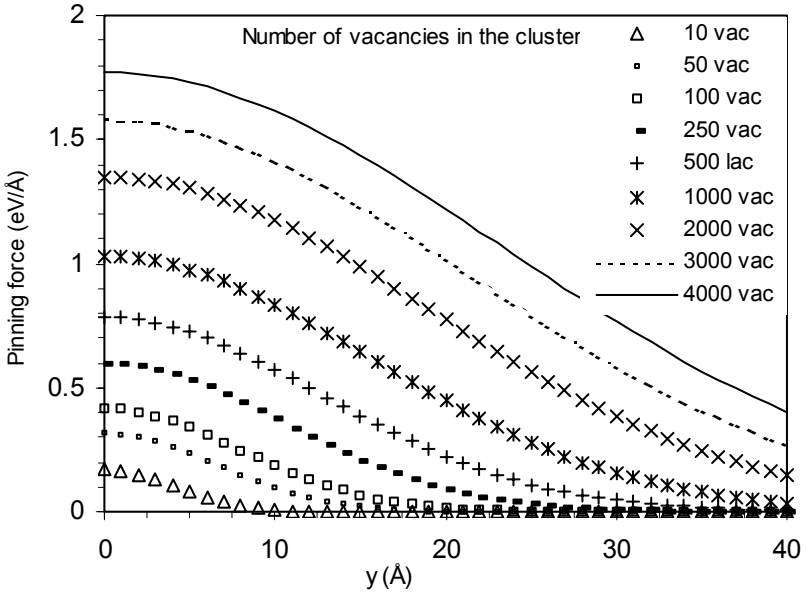

b) vacancy clusters

Figure 11: evolution of the pinning force versus the position of the slip plane (y) for different size of copper precipitates or vacancy clusters (y is defined on Figure 6).

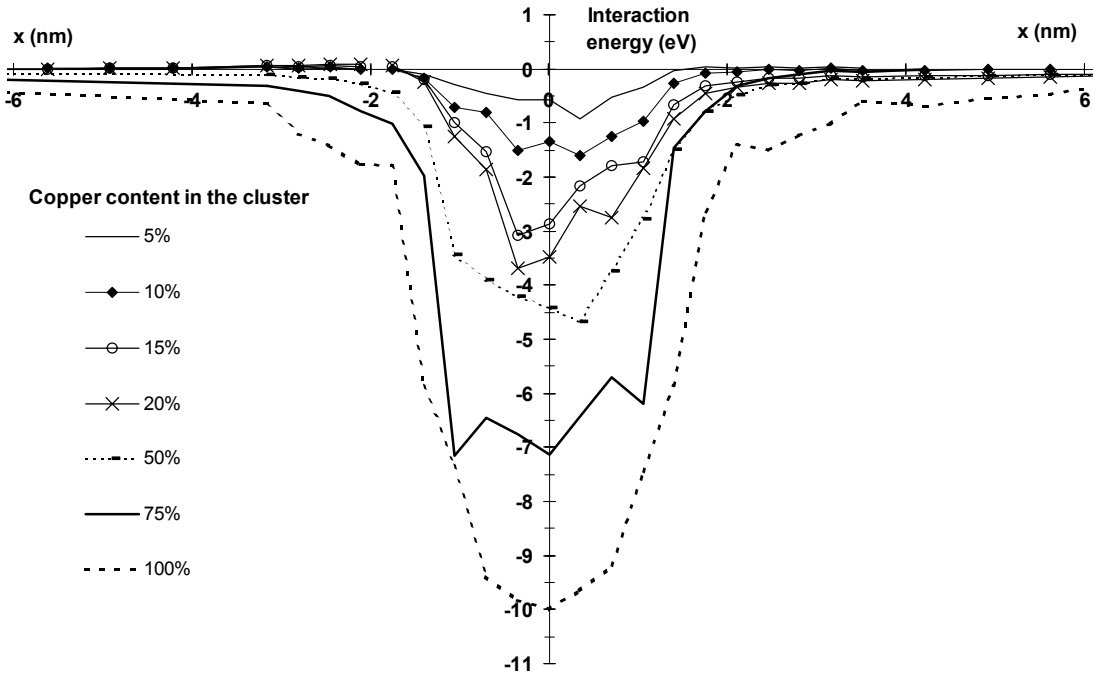

Figure 12: interaction energy versus distance for a screw dislocation and an iron-copper cluster containing 500 atomic site (r = 1.18 nm).

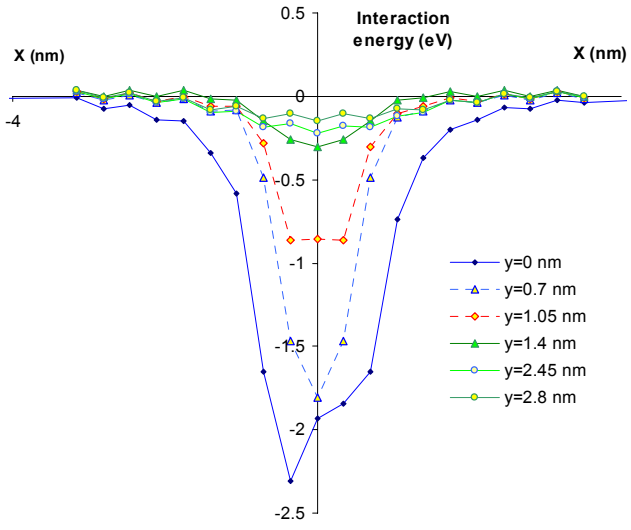

a) cluster of 50 vacancies

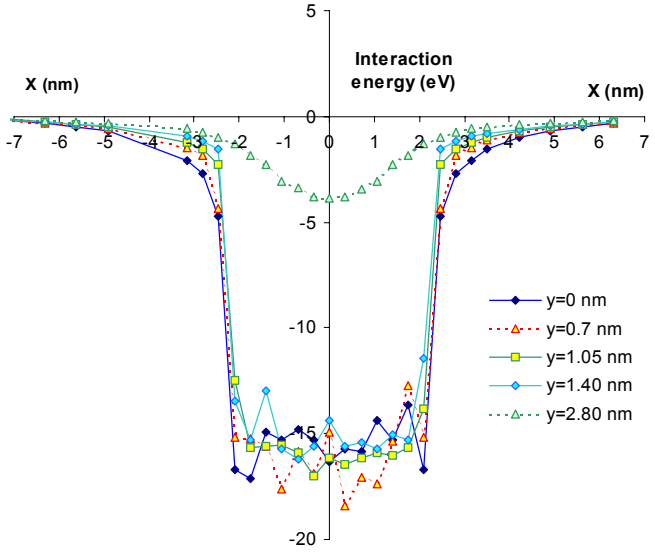

b) cluster of 2000 vacancies

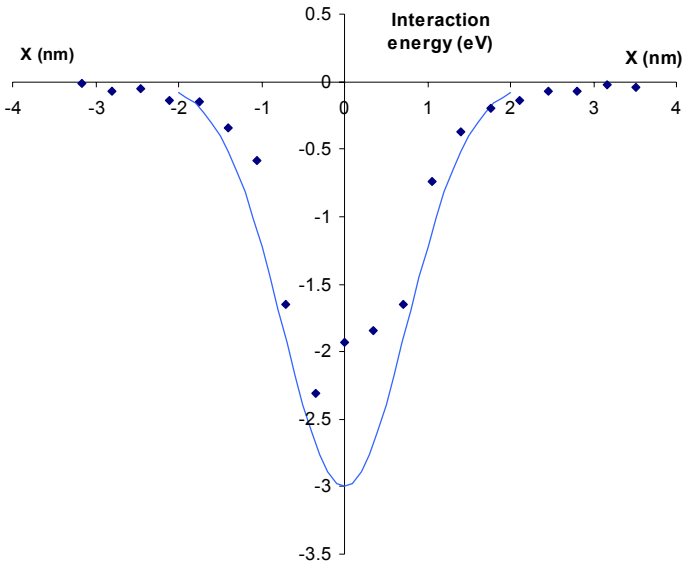

c) cluster of 50 vacancies

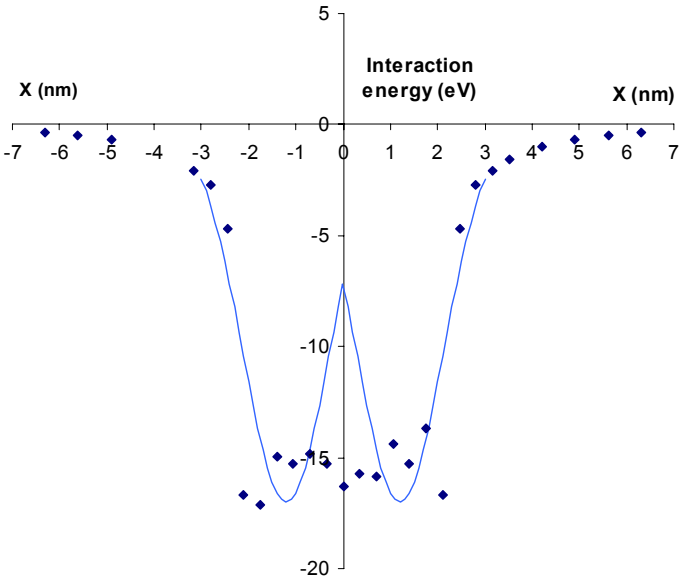

d) cluster of 2000 vacancies

Figure 13: examples of results obtained for the vacancy clusters (x and y are defined in Figure 6) :

- a and b : curves “interaction energy versus distance”;
- c and d : Gaussian curves fitted on simulation results obtained with y = 0.

2.4 Pinning forces used in RPV-1

The pinning forces used in RPV-1 to simulate the irradiation-induced hardening of RPV steels at 20°C are summarized in Table VI. Their estimation, obtained by Molecular Dynamics simulations at 0 K and presented in section 2.3, required some new approximations which are given in this section. In a first step, we derive the pinning forces at 0 K, then we take into account the thermal activation and approximate them at 20°C.

a) Pinning forces at 0 K

- **SIA loops**: by interacting with a SIA-loop, a screw dislocation forms either a junction or an helix. We consider that the pinning force of the junctions is $F_P^{Loop} \approx \mu b^2/8$ (see section 2.1). At 0 K, the helixes are much stronger obstacles, and probably lead to an Orowan mechanism [48].

- **Copper-rich precipitates**: as aforementioned, we consider that in the copper-rich precipitates Mn and Ni atoms have the same "hardening effect" as copper atoms. Thus, the pinning forces exerted by such precipitates at 0 K is calculated by replacing their Mn and Ni atoms by Cu atoms and using expression (9).

- **Vacancy-clusters**: the pinning forces (F_P^{Va}) exerted at 0 K by the vacancy clusters are calculated with expression (12).

- **Vacancy-solute atom clusters**: having no model to assess the pinning forces (F_P^{Va-sol}) exerted by the vacancy-solute atom clusters (as aforementioned they are probably made of small vacancy-copper atoms complexes distributed in a volume of some cubic nanometers), these forces are assessed by replacing Mn and Ni atoms by Cu atoms and by using the expression:

$$F_P^{Va-sol} \approx (F_P^{Cu} + F_P^{Va})/2 \qquad (13)$$

where F_P^{Cu} and F_P^{Va} are given by (9) and (12).

b) Thermal activation

- **SIA loops**: we consider that at 20°C thermal fluctuations do not help significantly the screw dislocations to escape from the junctions they formed with SIA-loops. However, we suppose that the helixes disappear shortly after their creation and then do not exert any significant pinning force. Indeed, an helix on a screw dislocation may be described as a succession of kinks on {110} slip planes (see sketch in Figure 14). As recently confirmed by Molecular Dynamics

simulations [17], kinks are very mobile along screw dislocation lines in iron at room temperature. At this temperature, screw dislocation lines are mostly straight in irradiated RPV steels (the Peierls friction stress is still efficient and the dislocations are slightly bowed between the irradiation-induced defects since they are weak obstacles), then the applied shear stress can easily sweep the kinks along them. Whatever the applied stress, two configurations have to be taken into account according to the orientation of the applied stress:

- ✓ all the kinks forming the helix are swept out to the extremities of the dislocation segments where they may be absorbed by sinks (e.g. grain boundaries, carbide-matrix interfaces), which makes the helix vanish (Figure 15). At the end of the process, the loop has disappeared and the dislocation line has regained its straight configuration.
- ✓ two kinks forming the helix slip in opposite directions and create a cross-kinks (Figure 16). As proposed by Marian et al [17], kinks slipping along the dislocation line and piling up on the cross-kink can suppress it and rebuild the loop behind the dislocation. These new kinks can be generated in other parts of the dislocation (e.g. by thermal activation, from other helixes).

In conclusion, we consider that at 20°C:

- ✓ the loops containing more than 19 SIAs and with a Burgers vector non-parallel to that of the dislocation (see section 4.1) lead to the formation of junctions and exert a force $F_P^{Loop} \approx \mu b^2/8$.
- ✓ the loops with less than 19 SIAs as well as the larger loops with a Burgers vector parallel to that of the dislocation (see section 4.1) lead to the formation of helixes and do not exert any pinning force on the dislocation ($F_P^{Loop} \approx 0$).

- **Copper-rich precipitates, vacancy clusters and vacancy-solute clusters**: as explained in section 2.1.b, thermal activation can reduce the critical shear stress of irradiated RPV-steels either by modifying the interaction mechanism between the defects and the dislocations or by inducing atomic fluctuations large enough to help the dislocations to overcome the smallest defects. To assess the pinning forces exerted at 20°C by the copper-rich precipitates, vacancy clusters and vacancy-solute clusters, we consider only the latter mechanism. In particular, for the copper-rich clusters and vacancy-solute clusters, we do not introduce the temperature dependence observed by Bacon et Osetsky in the case of pure copper precipitates (see section 2.2), for at least two reasons:

- ✓ the considered irradiation-induced defects are small (core zone of about 1 nm for the copper-rich precipitate) or contain a high concentration of iron atoms (about 80% for the vacancy-solute clusters), thus their tendency for bcc-to-fcc transformation must be weak whatever the temperature;

- ✓ since we consider a screw dislocation, we do not expect any significant climbing effect during the overcoming of the defects.

It will be seen in section 2.5 of this Chapter, that neglecting the pinning force temperature dependence measured by Bacon and Osetsky for an edge dislocation, does not affect the quality of our simulations even for large ($r \approx 1$ nm) pure copper precipitates. This observation may indicate that this temperature dependence is weaker for screw dislocations than for edge ones.

In section 2.1.b, it was estimated that at 20°C the dislocations can overcome defects with a binding energy lower than about –0.7 eV without the help of the stress. This binding energy corresponds to vacancy-clusters, copper-rich precipitates and vacancy-solute clusters containing less than 5 solute atoms or vacancies. Consequently, we consider that such defects do not introduce any hardening at 20°C. The solute atoms they contain are supposed to be in solution and to contribute to the athermal solution hardening.

Table VI: summary of the pinning forces used in RPV-1.

Defect	Size of the defect*	Force (eV/nm)
SIA loops	N < 19	$F_P^{Loop} = 0$
	N ≥ 19	- $F_P^{Loop} = 0$ for parallel Burgers vectors (formation of an helix): apples to one quarter of the loops - $F_P^{Loop} = \mu b^2/8$ for non-parallel Burger vectors (formation of a junction): applies to three quarters of the loops
Copper-rich precipitates	N < 6	Copper atoms contribute the solution hardening
	N ≥ 6	$F_P^{Cu} = 1.3\ F_{pm}^{Cu} \exp(-0.843 r^{-4.53} y^4)$ with $F_{Pm}^{Cu} = 0.39 r^{1.17}$
Vacancy clusters	N < 6	$F_P^{Va} = 0$
	N ≥ 6	$F_P^{Va} = 1.2\ F_{pm}^{Va} \exp(-0.219 r^{-1.74} y^2)$ with $F_{Pm}^{Va} = 0.373 r^{1.23}$
Vacancy-solute clusters	N < 6	$F_P^{Va-sol} = 0$
	N ≥ 6	$F_P^{Va-sol} = (F_P^{Cu} + F_P^{Va})/2$

* N = number of cu atoms or vacancies in the defect.

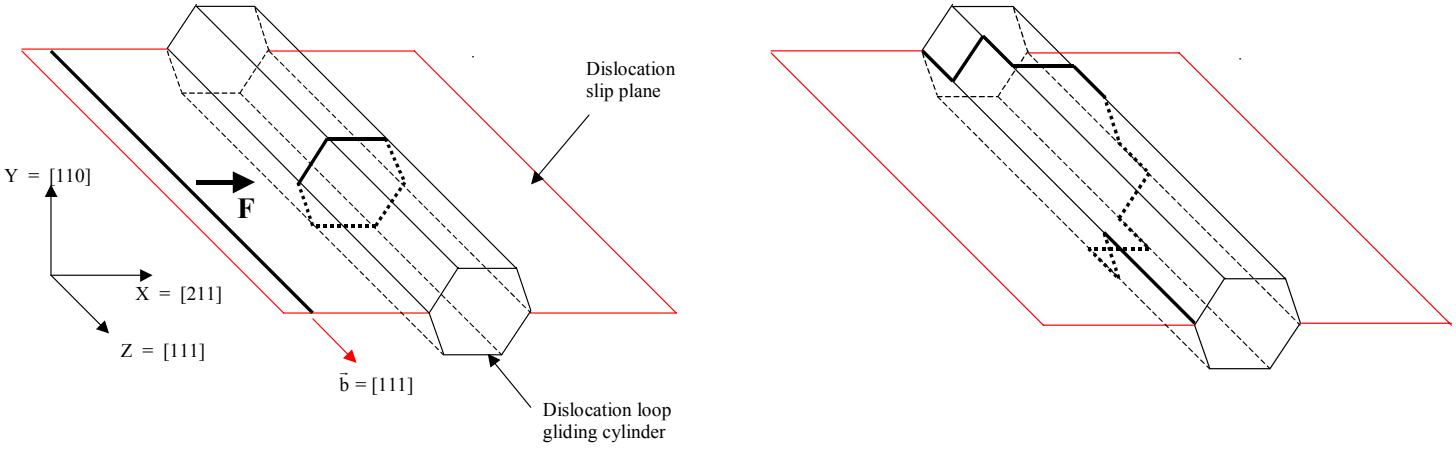

Figure 14: sketch showing a screw dislocation interacting with SIA loops (habit plane perpendicular to the dislocation line) and forming an helix described as a succession of kinks on {110}slip planes. Both defects have parallel Burgers vectors.

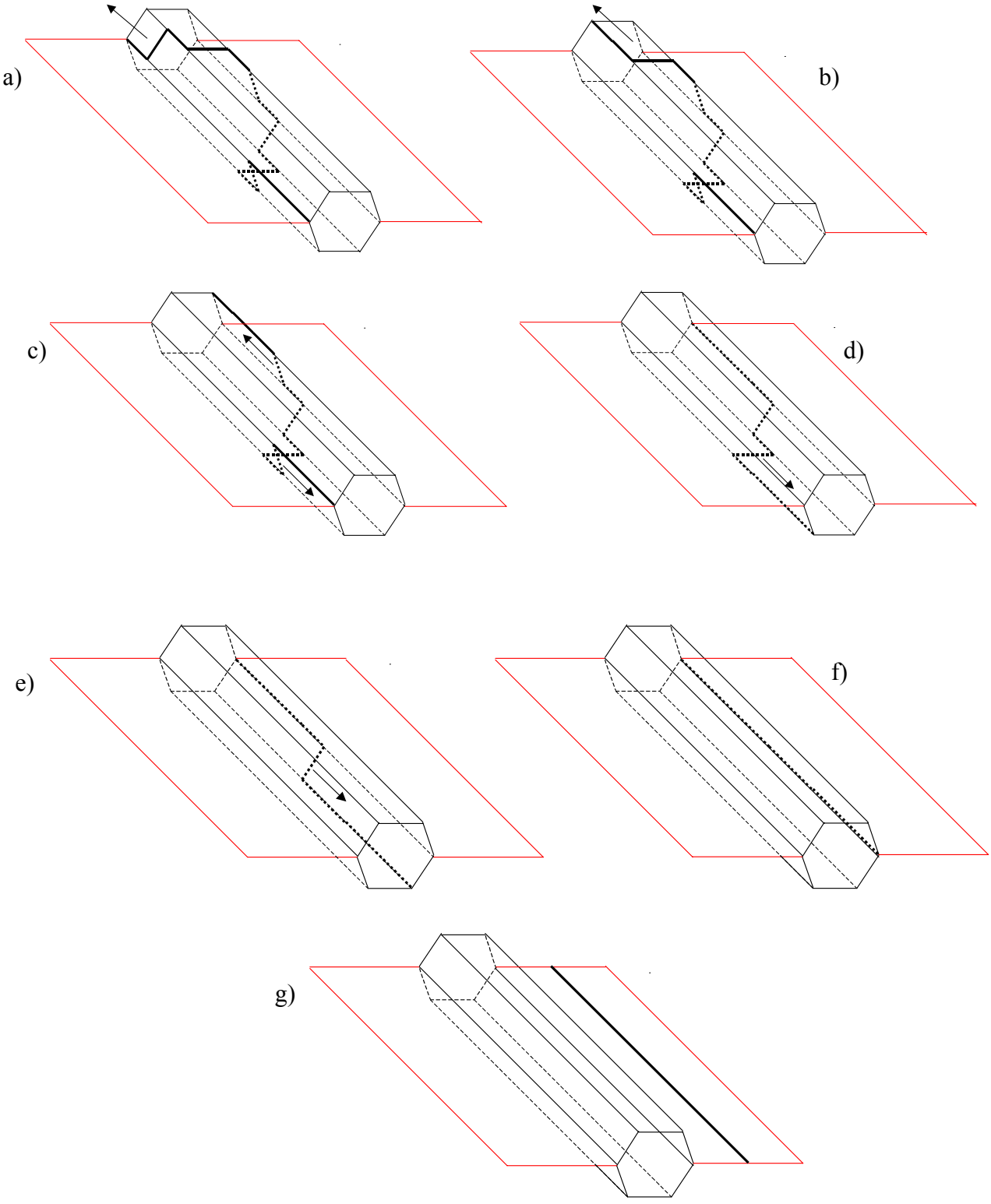

Figure 15: disappearance of a loop on a screw dislocation by gliding of kinks away from the loop area (the arrows indicates the directions of gliding of the kinks), vectors are given in Figure 14.

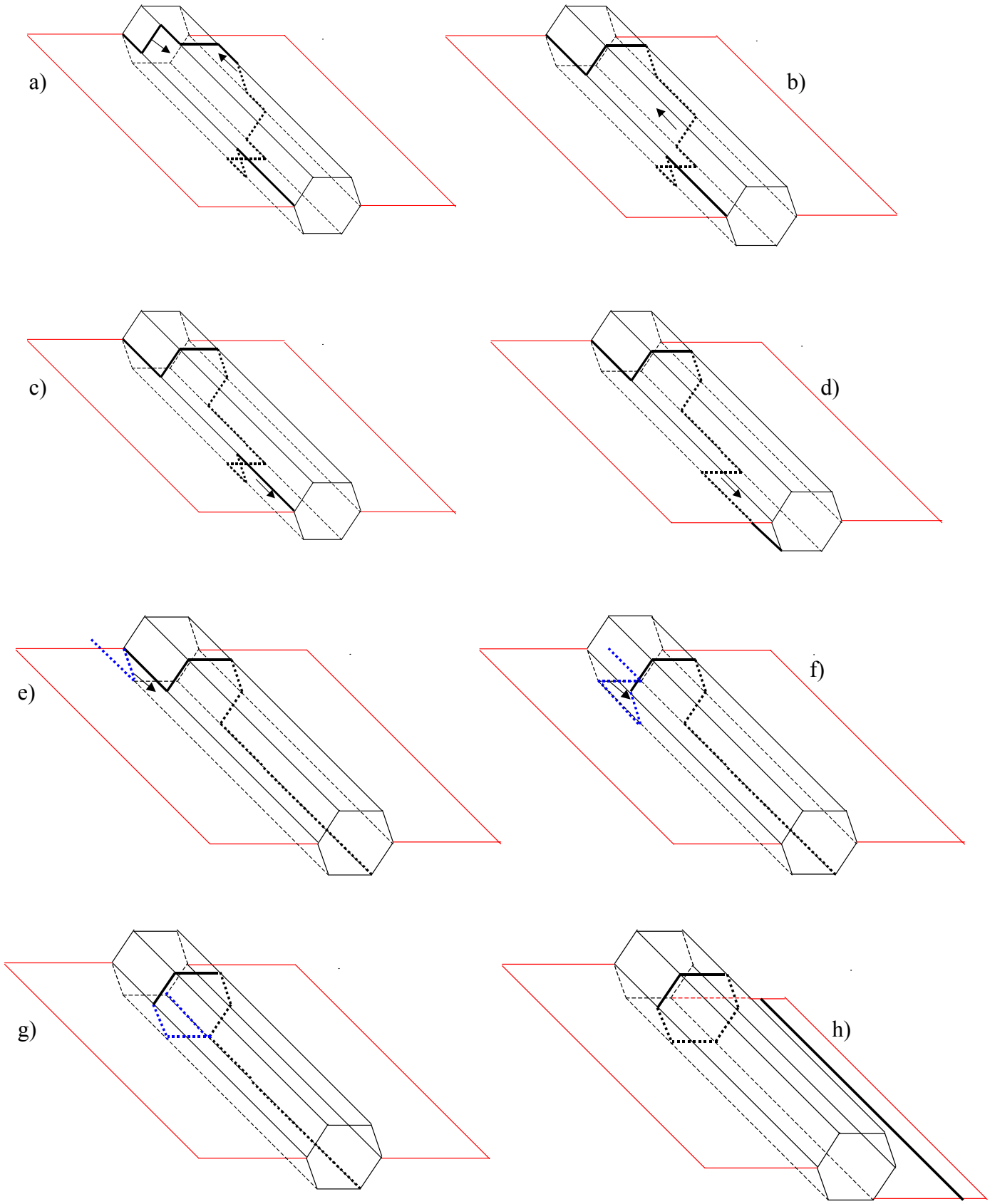

Figure 16: reconstruction of a loop from an helix on a screw dislocation by gliding of kinks away and to the loop area (the arrows indicate the directions of gliding of the kinks, the blue kinks are coming from other parts of the dislocation line), vectors are indicated in Figure 14.

III -Experimental validation

3.1 - Experimental conditions

We attempted to validate the approach used in RPV-1 to simulate the grain hardening (use of DUPAIR with the assessed pinning forces) by comparing simulation results with previously published experimental results. The challenge was to find out available results of mechanical tests carried out on iron-based alloys for which a complete description of the hardening defects was available. The possibilities were very limited and we had to separate the validation for copper precipitates on the one hand from vacancy clusters and SIA loops on the other hand.

- **For Copper precipitates,** results provide by Goodman et al. [49] and Mathon [50] on Fe-1.5%Cu alloys thermally aged at 500°C were used. It is well known that at this temperature, such type of alloy exhibit a hardening resulting from the precipitation of copper precipitates. Goodman et al studied this hardening by tensile tests at 20°C and Mathon by hardness tests. Both teams characterized the copper precipitates by Small Angle Neutron Scattering (SANS).

To supplement these previous studies, we performed additional ageing to establish a relationship between hardness and yield stress increases and to get precise information on the chemical composition of the precipitates. To do so, tensile tests, hardness tests and Atom Probe experiments were carried out on a Fe-1.5%Cu alloy aged 1.5, 2.5 and 25 hours at 500°C. The mechanical testings were performed in the Laboratoire de Métallurgie Physique et Génie des Matériaux of the University of Lille and the Atom Probe examinations in the Groupe de Physique des Matériaux of the University of Rouen.

- **For the vacancy clusters and SIA loops**, the results of tensile tests, TEM experiments and Positron Annihilation experiments obtained by Eldrup et al [51], on pure iron neutron-irradiated in HIFR at 70°C, probably constitute the most complete set of experimental data which can be used. Unfortunately, the microstructural data present uncertainties inherent to the used techniques (no information on SIA-loops with a radius smaller than 1 nm and pretty large uncertainty band on PA results). Thus, the Eldrup et al results were used to check that the simulation provide results with correct order of magnitude.

3.2 - Comparison of simulation and experimental results

As demonstrated hereafter, the comparison with experimental results shows that the simplified approach used in RPV-1 to simulate grain hardening (use of DUPAIR with the assessed pinning forces) leads to reasonable results.

- **Copper precipitate hardening**: the tensile and hardness tests carried out on the Fe-1.5%Cu alloy aged 1.5, 2.5 and 25 hours at 500°C (Table VII) show that the increases of hardness and yield stress resulting form the copper precipitation in this alloy verify the following relation:

$$\Delta R_{P0.2} = 2.5\ \Delta H_v \qquad (14)$$

The Tomographic Atom Probe experiments on the same alloy reveal that the copper content in the precipitates is about 85% after the 1.5 h ageing time and 100% for the 2.5 and 25 h ageing times.

Results previously obtained by Goodman et al [49] and Mathon [50] on aged Fe-1.5%Cu alloys are summarized in Table VIII. In all cases, the precipitates have an average radius much lower than the critical value of 9 nm from which a transformation of their bcc structure into a 9R structure is expected. It can be noticed that the thermal hardening results mainly from precipitates with a radius lower than 1.2 nm. Therefore, the pinning forces derived in this study can be used to describe their interaction with a screw dislocation. Expression (14) was used to determine the increase of yield stress of the alloy studied by Mathon from the hardness data. The obtained values are plotted in Figure 17 with those published by Goodman et al and those measured in this study. All the results are consistent.

For each ageing time, the number density and average radius of the precipitates determined by Goodman et al and Mathon (SANS experiments) were used as input parameters of the DUPAIR code to simulate the corresponding increase of yield stress. For the ageing times longer than 2.5 hours, the pinning forces of the precipitates were calculated from expression (7). For the 2.5 hours ageing time, we used the expression (9) multiplied by 0.85 to allow for the presence of about 15% of iron in the precipitates (see expression (10)).

The volume of the crystal simulated with DUPAIR was adjusted so that 5000 defects were taken into account in each simulation. For each ageing time, we carried out 5 simulations with different random distributions of defects and we took into account the softening of the solid solution resulting from the copper depletion. This softening was assessed from (14) and the expressions established by Akamatsu $\Delta H_V = 32\ \Delta Cu_{Sol}$ [52], where $\Delta R_{P0.2}^{Sol}$ (MPa) is the increase of yield stress associated to an increase ΔCu_{Sol} (wt %) of the copper content in solid solution. The average results obtained are in agreement with experimental ones as shown in Figure 17. This agreement may mean, as it was aforementioned, that the temperature dependence of the pinning force observed by Bacon and Osetsky is lower for screw dislocations than for edge ones.

- **Vacancy clusters and SIA loops**: results published by Eldrup et al are summarized in Table IX. With the measured size and number densities of point defect clusters, DUPAIR simulates an increase of yield stress of 30 and 45 MPa for the doses of 0.009 dpa and 0.23 dpa, respectively. The simulated results are smaller than the experimental ones, but as expected, have the right order of magnitude (cf section 3.1).

Table VII: increase of the hardness and the yield stress of a Fe-1.5%Cu alloy during ageing.

Ageing time (h)	ΔH_v	$\Delta R_{P0.2}$ (MPa)
1.5	117	292
2.5	108	270
25	103	257

Table VIII : Ageing of Fe-1.5Cu alloys - mechanical testing and SANS results obtained by Goodman et al [49] and Mathon [50].

Ageing time (h)	1*	2.5**	3*	4.5**	8**	9.4*	25**	42*	124*	142**	312**
Number density of Cu precipitates (10^{22} m^{-3})	95	200	100	17	8	11	7	2.8	0.8	0.7	0.4
Mean radius of the Cu precipitates (nm)	0.8	0.9	1.2	2.3	2.9	2.8	3	4.8	7.3	6.3	8
Increase of hardness	-	75	-	118	112	-	95	-	-	62	53
Increase of yield stress (MPa)	314	-	321	-	-	295	-	205	124	-	-

* from [49]
** from [50]

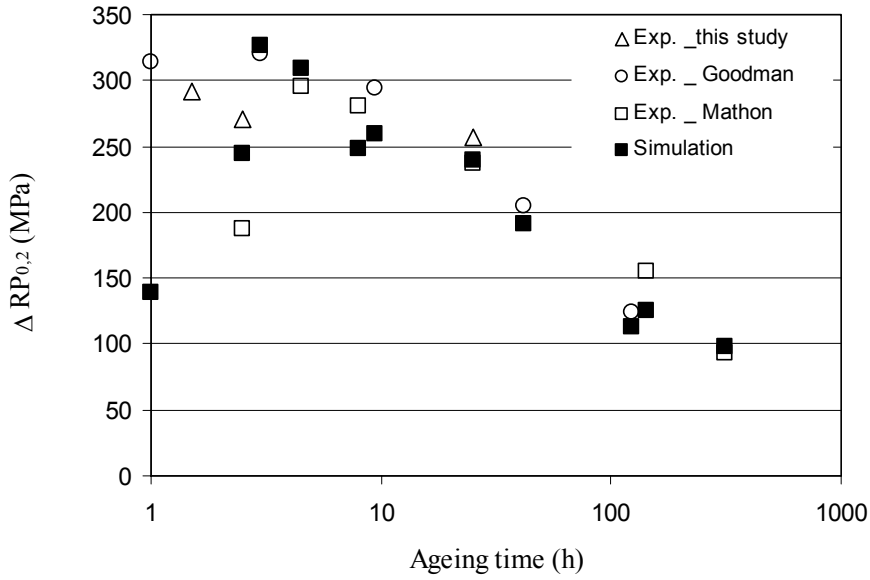

Figure 17: simulation of the evolution of the yield stress at 20°C of Fe-1.5%Cu alloys during ageing at 500°C. Comparison with experimental results from [49, 50].

Table IX: results of tensile tests, TEM experiments and Positron Annihilation experiments carried out by Eldrup et al on iron irradiated at 70°C in HFIR [51].

Dose (dpa)	Vacancy clusters		SIA loops (10^{22} m^{-3})	$\Delta R_{P0.2}$ at 70°C	
	Diameter (nm)	Number density (10^{24} m^{-3})		Measured (MPa)	Simulated (MPa)
0.009	0.35	≈ 0.5	1	≈ 80	30
	0.55	≈ 1.7			
	0.75	≈ 0.2			
	1	≈ 0.05			
0.23	0.55	≈ 3.4	5	≈ 180	45
	0.75	≈ 0.7			
	1	≈ 0.08			

IV - Conclusion

This Chapter described the simplified approach adopted to simulate the irradiation-induced hardening with RPV-1. This approach relies on the use of a Foreman and Makin type code, called DUPAIR, and on a characterization of the pinning forces exerted by the irradiation-induced defects on a screw dislocation. These forces were estimated from Molecular Dynamics simulations.

The relevance of the proposed approach was validated by the comparison with experimental results. However, this work has to be considered as an initial step to facilitate the development of a first tool to simulate irradiation effects. It can be improved by many ways (use of Dislocation Dynamics code, …).

References

1 Jumel, S, Ruste, J, Domain, C., van Duysen, J. C., “Interactions between dislocations and irradiation-induced defects in light water reactor pressure vessel steels”, accepted for publication in J. Nucl. Mater.
2 Foreman, A.J.E., Makin, M.J., Phil. Mag., vol. 14, (1964), p.911.
3 Odette, G., R., "Neutron Irradiation Effects in Reactor Pressure Vessel Steels and Weldments", IAEA report, ref IWG-LMNPP-98/3, chapter 10, (1998), p. 438.
4 Cottrell, A. H., Dislocation and Plastic Flow in Crystals (Oxford) (1953).
5 Friedel, J., Dislocation (Pergamon), 1964.
6 Wit, G., Koehler, J.S., Phys. Rev., vol.116, (1959), p. 1113.
7 Peach, M., Koehler, J. S., Phys. Rev., vol. 80, (1950), p. 436.
8 Foreman, A. J. E., Makin, M. J., Canadian Journal of Physics, vol. 45, (1967).
9 Brown, L. M., Ham, R. K., “Dislocation-particles interactions”, chapter 2 in Strengthening Methods in Crystals, edited by Kelly, A. and Nicholson, R. B., Applied Science Publisher LtD, London, (1971), p. 9.
10 Gerold, V., “Precipatation hardening”, chapter 15 part 3 in Dislocation in Solids, edited by Nabarro, F. R. N., North-Holland Publishing Company, (1979), p. 222.
11 Bacon, D. J., Kocks, R. O., Scattergood, Phil. Mag., vol.28, (1973), p.1241.
12 Ashby, M. F., The Theory of Critical Shear Stress and Work Hardening of Dispersion-Hardened Crystals, in Proc. Second Bolton Landing Conference on Oxide Dispersion Strengthening (Gordon and Breach), (1968), p. 143.
13 Orowan, E., 1948, discussion in the Symposium on Internal Stresses in Metals and Alloys, p. 451 (London, The Institute of Metals).
14 van Duysen, J.C., Thèse de doctorat, Université Paris Sud, Orsay, (1995).
15 Aono, Y., Kuramoto, E., and Kitajima, K., Report of Research Inst. For Applied Mechanics, vol. 29, Kyushu Univeristy, (1981), p. 127.
16 Farkas, D., and Rodriguez, P.L., Scripta Met. Mat., vol. 30, N°7, (1994), p. 921.
17 Marian, J., Cai, W., Bulatov, V., Nature materials, vol. 3, (2004).
18 Jumel, S., van Duysen, J. C., “Mechanisms Governing the Irradiation-Induced Embrittlement of Light Water Reactor Pressure Vessel Steels” , AIEA, To be published
19 Odette, G.R., Lucas, G.E., Radiation Effects and Defects in Solids, vol. 144, (1998), p. 189.
20 Odette, G.R., Lucas, G.E., ASTM-STP 909, (1986), p. 206.
21 Phythian, W.J., Foreman, A.J.E., English, C.A., Buswell, J.T., Hetherington, MG., Roberts, K. and Pizzini, S., Proc. 15th Int. Symp. On Effects of Radiation on Materials, ASTM-STP 1125, (1992), p.131.
22 Russell K.C., and Brown, L.M., Acta Metall., vol. 20, (1972), p.969.
23 Harry, T., Bacon, D. J., Acta Mater., vol. 50, (2002), p.195 and 209.
24 C.L. Liu, G.R. Odette, B.D. Wirth, G.E. Lucas, Materials Science and Engineering A 238 (1997) 202-209
25 Coulomb, P. and Friedel, J., “Dislocations and Mechanical Properties of Crystals, Wiley, New York, (1957), Lake Placid Conference, (1956), p. 555.
26 Osetsky, Y.N., Bacon, D.J., Modelling & Siml. in Mater. Sci. & Eng. , vol. 11, (2003), p. 247.
27 Bullough, T.B., and Newmann, T.J., Phil. Mag, vol. 7, (1962), p. 529.
28 Kroupa, F., Phil. Mag., vol. 7, (1962), p. 783.
29 Kroupa, F., Hirsch, P. B., Discussion at the Faraday Society, 38, (1964), p. 49.
30 Makin, M., Phil. Mag., vol. 10, N° 106, (1964), p. 695.
31 Hirth, J. P., Lothe, J., “Theory of Dislocations”, 2nd edition, (1982).
32 Rhee, M., Zbib, H. M., Hirth, J. P., Huang, H., de la Rubia, T., Model. Simul. Mater. Sci. Eng.,

6, (1998), p. 467.
33 Saada G., Washburn, J., Journal of the Physical Society of Japan, vol. 18, supplement I, (1963), p. 43.
34 Kimura, H., Maddin, R., "Lattice Defects in Quenched Metals", Academic Press, New York, (1969), p. 319.
35 Foreman, A., Sharp, J.V., Phil. Mag., vol. 19, (1969), p. 931.
36 Hirsch, P.B., "Point defect cluster hardening" in "Vacancies 76", (1976), Ed. Smallman, R.E., Haris J.E.
37 Eyre, B., L., Barlett, A., F., ibid, vol. 11, (1965), p.53.
38 Bacon, D. J., Osetsky Yu., N., J. Nucl. Mater., vol. 329-333, (2004), p.1233.
39 Kirk, M.T., Natishan, M.A.E., Wagenhofer, M., "Microstructural limits of applicability of the Master Curve", ASTM-STP 1406, (2001).
40 Jumel, S., Domain, C., Ruste, J., van Duysen, J.C., Becquart, C., Legris, A., Pareige, P., Barbu, A., Van Walle, E., Chaouadi, R., Hou, M., Odette, G.R., Stoller, R., Wirth, B.D., Journal of Testing and Evaluation, vol. 30, (2002), p. 37.
41 Shasstry, V., Diaz de la Rubia, T., Journal of Engineering Materials and Technology, vol. 121, (1999), p. 126.
42 Becquart, C.S., Decker, K.M., Domain, C., Ruste, J., Souffez, Y., Turbatte, J.C., Van Duysen, J.C., "Massively parallel Molecular Dynamics simulations with EAM potentials ", Radiation Effects and Defects in Solids, vol. 142, (1997), p. 9.
43 Ludwig, M., Farkas, D., Pedraza, D., Schmauder, S., Model. Simul. Mater. Sci. Eng., vol. 6, (1998), p. 19.
44 Suzuki, H., Rosenfield, A.R., Hahn, G.T., Bement, A.L. and Jaffee, R.I., "Dislocation Dynamics ", Eds. McGraw-Hill, (1968), p. 679.
45 Vitek, V., Perrin, R. C., Bowen, D. K., Philos. Mag., vol. 21, (1970), p. 1049.
46 Jumel, S. unpublished results.
47 Othen, P.J., Jenkins, M.L., Smith, G.D.W., and Phythian, W.J., Phil. Mag. Letters, vol. 64, (1991), p.383.
48 Marian, J., Wirth, B.D., Schaüblin, R., Odette, G.R., Perlado, J.M., J. Nucl. Mater., vol. 323, (2003), p. 181.
49 Goodman, S.R., Brenner, S., S, Low, J.R., Metall. Trans., vol. 4, (1973), p. 2363.
50 Mathon, M.H., "Etude de la précipitation et des mécanismes microscopiques de durcissement sous irradiation dans des alliages ferritiques dilués", Thèse de doctorat, Université Paris Sud, Orsay, (1995).
51 Eldrup, M., Singh, B. N., Zinkle, S. J., Byun, T. S., Farrell, K., J. Nucl. Mater., vol. 307-311, (2002), p. 912.
52 Akamatsu-Jousset, M., "Evolution microstructurale d'alliages ferritiques sous irradiation", Thèse de Doctorat, Université Paris-Sud, Orsay, (1994).

CHAPTER V

Quality of the simulations with RPV-1

As mentioned in the introduction, the main objective of the presented work was to build a first multi-scale tool to simulate irradiation effects. Chapter II showed that this objective was reached. It is now necessary to verify the quality of the simulations. This can be done by checking the sensitivity of RPV-1 to its input parameters, assessing the quantitative character of the results and discussing the errors and uncertainties.

I - Sensitivity to the input data

The development of VTRs can be impaired by an intrinsic weakness of the multi-scale approach required to build such tools. Indeed, this approach necessitates the homogenisation of results before each scaling up of time or space. Every homogenisation induces a loss of information which may alter the sensitivity of the tool to its input data. The main homogenisations done during a simulation with RPV-1 are described in Table I. Considerable efforts would be required to quantify their individual or collective "buffer" effects on the RPV-1 sensitivity. However, as presented in the following sections, it has been checked that the collective effect is low, even in a large range of irradiation conditions (flux, temperature,…).

It is mentioned that the results presented in this Chapter were obtained with the version 1.2.g of RPV-1.

1.1 - Sensitivity to the copper content

RPV-1 was run to simulate the irradiation-response of four steels containing 0.05, 0.10, 0.20 and 0.30% Cu (with 1.45% Mn, 0.2%Ni). The four simulations were performed at 250°C with a neutron spectrum representative of an irradiation channel of the British experimental reactor HERALD ($\Phi_{E>1MeV} = 5\ 10^{12}$ n.cm^{-2}.s^{-1}).

The simulated irradiation-induced increases of yield stress are plotted versus the dose in Figure 1a. It can be noticed that the hardening increases with the copper content, which shows that RPV-1 is sensitive to the copper content.

Table I : main homogenisations done during a simulation with RPV-1.

SPECMIN	• Homogenization of neutron's energies. The neutrons are listed according to groups of energy; all the neutrons belonging to a same group are considered to have the same energy: i.e. the middle-group energy. The width of the group is increasing with increasing energy. • Homogenization of the neutron's fates (elastic collisions with lattice atoms, …). All the neutrons having the same energy are considered to have the same fate: i.e. the average fate provided by the cross sections for the considered energy.
INCAS	• Homogenization of PKA's energies. The PKAs are listed according to groups of energy; all the PKAs belonging to a same group are considered to have the same energy: i.e. the middle-group energy. The width of the group is increasing with increasing energy. • Homogenization of PKA's fates (sub-cascade productions,…). All the PKAs with the same initial energy are considered to have the same fate: i.e. the average fate given by the collision cross sections for the considered energy. • Homogenization of the energies dissipated in (sub)-cascades. The (sub)-cascades are classified according to groups of dissipated energy (15-25 keV, 25-35 keV, ...); all the (sub)-cascades belonging to a same group are considered to spread the same energy: i.e. the middle-group energy (10 keV, 20 keV,...). • Homogenization of the size distribution of the surviving point defects left by the small damage zones produced between the (sub)-cascades: 60% of their SIAs are isolated, 20% are in clusters of size 2, 10% in clusters of size 3,...
CASCADE database	• Homogenization of the germs of hardening defects. All the (sub)-cascades with the same dissipated energy are considered to produce the same germs of hardening defects.
MFVISC	• Homogenization of the size distribution of hardening defects within a grain. • Homogenization of the behavior of all the defects having the same size and content (SIAs, vacancies and/or Cu atoms).
FORCE database	• Homogenization of the pinning forces of all the hardening defects having the same size and content (SIAs, vacancies and/or Cu, Mn and Ni atoms).
DUPAIR	• Homogenization of the irradiation response of all the steel grains.
Taylor Factor	• Homogenization of the distribution of the spatial orientation of grains.

For a dose of 0.1 dpa, the yield stress copper-dependence is about 240 MPa/%Cu which is within the scattering band of experimental results. Figure 1b and c show the final size distributions of the hardening defects in the 0.05% and 0.30%Cu steels for the dose of 0.1 dpa. The number density of defects containing copper clearly increases with the steel copper content.

1.2 - Sensitivity to nickel and manganese contents

RPV-1 is sensitive to nickel and manganese contents, but its dependence to both elements is not satisfactory. This issue is attributable to a weak parameterization of the DIFFG code. Work is in progress to improve it, meanwhile, we decided not to display any results concerning Ni or Mn effect.

1.3 - Sensitivity to the irradiation temperature

RPV-1 was run to simulate the irradiation-response of a 0.05%Cu-1.3%Mn-0.7%Ni steel, at four temperatures: T = 55, 200, 250 and 300°C. The simulations were performed with a neutron spectrum representative of an irradiation channel of the American experimental reactor HFIR ($\Phi_{E\geq 1MeV} = 7\ 10^{14}$ n.cm^{-2}.s^{-1}) up to a dose of 0.1 dpa.

The simulated irradiation-induced increases of yield stress are plotted versus the dose in Figure 2a. It can be noticed that the hardening increases as the irradiation temperature decreases, which shows that RPV-1 is sensitive to the irradiation temperature. For a dose of 0.1 dpa, the yield stress temperature dependence is about 0.6 MPa/°C, which is in agreement with experimental results (see Chapter I). Figure 2b and c show the final size distributions of the hardening defects for the irradiation carried out at 55 and 300°C with a dose of 0.1 dpa. The number densities of SIA loops and vacancy clusters clearly increase as the irradiation temperature decreases.

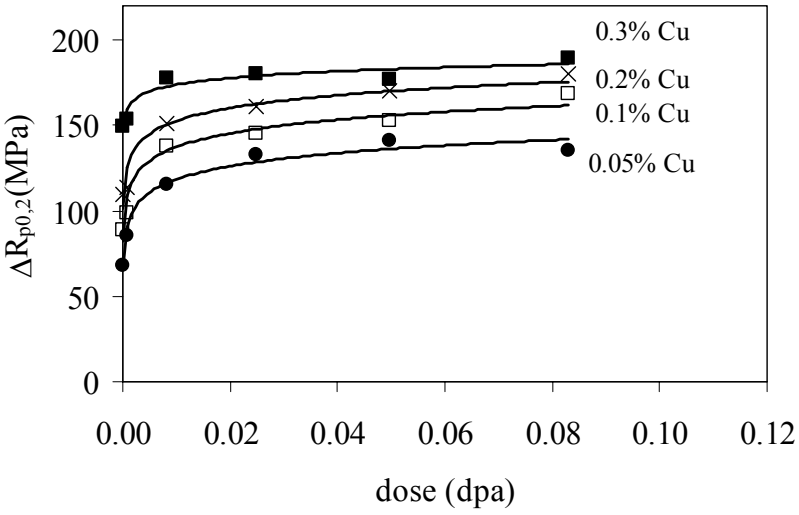

a)

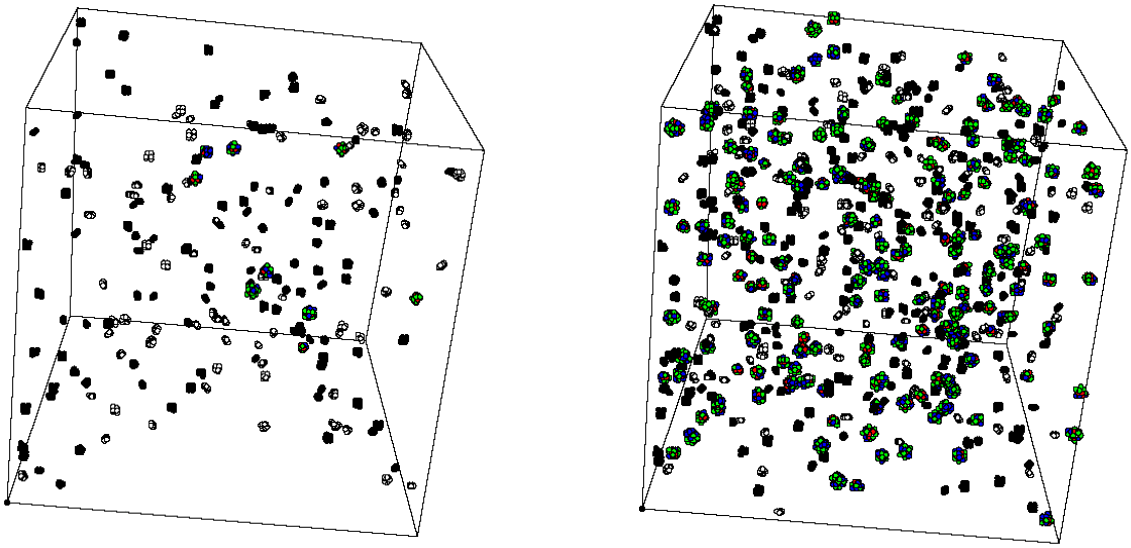

b) c)

Figure 1: sensitivity of RPV-1 to the copper content. Simulation at 250°C with a neutron spectrum representative of an irradiation channel of the reactor HERALD ($\Phi_{E>1MeV} = 10^{12}$ n.cm^{-2}.s^{-1}) - steel with 1.45%Mn and 0.2%Ni.

a) irradiation-induced increase of yield stress;

b) distribution of hardening defects for Cu = 0.05 % and a dose of 0.1 dpa;

c) distribution of hardening defects for Cu = 0.3 % and a dose of 0.1 dpa.

(vacancy: white, SIA: black; Cu: red, Mn: green, Ni: blue ; box size: 28.7 x 28.7 x 28.7 nm^3)

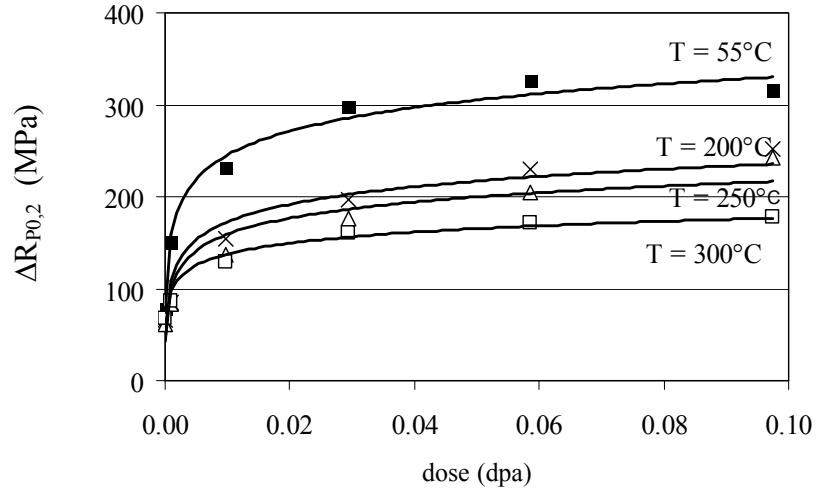

a)

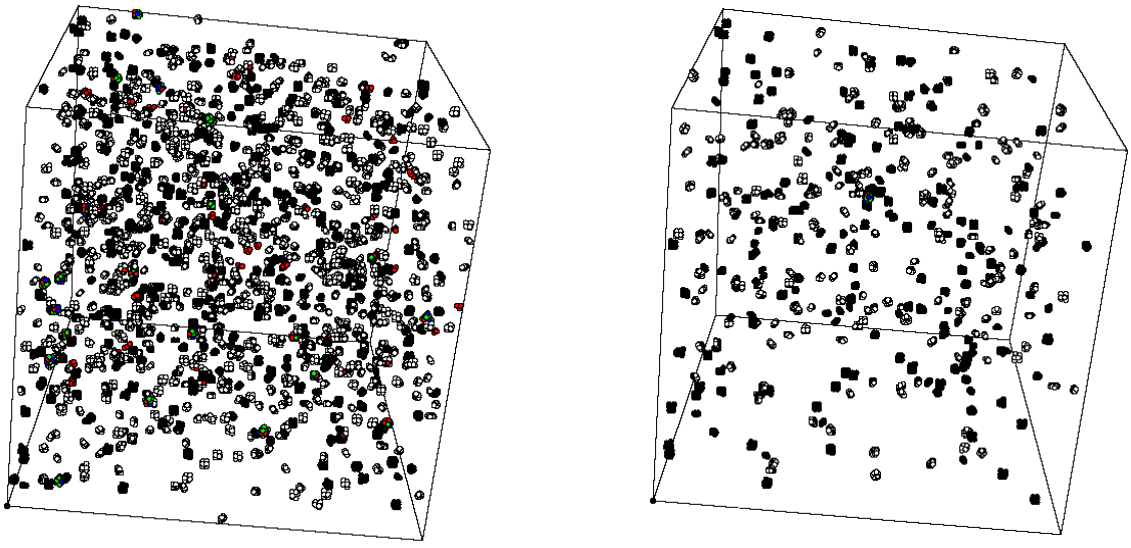

b) c)

Figure 2: sensitivity of RPV-1 to the irradiation temperature of a steel containing 0.3%Cu, 1.3%Mn and 0.7%Ni. Simulations performed at four temperatures (T=55, 200, 250 and 300°C) with a neutron spectrum representative of an irradiation channel of reactor HFIR ($\Phi_{E\geq 1MeV}$ = 7 10^{14} n.cm^{-2}.s^{-1}) up to a dose of 0.1 dpa.

a) irradiation-induced increase of yield stress;

b) distribution of hardening defects for T = 55 °C and a dose of 0.1 dpa;

c) distribution of hardening defects for T = 300 °C and a dose of 0.1 dpa.

(vacancy: white, SIA: black; Cu: red, Mn: green, Ni: blue ; box size: 28.7 x 28.7 x 28.7 nm^3)

1.4 - Sensitivity to the neutron flux

RPV-1 was run to simulate the irradiation-response of a 0.05%Cu-1.3%Mn-0.7%Ni steel under four neutron fluxes. The simulations were carried out at 55°C with a dose up to 0.1 dpa. A neutron spectrum representative of an irradiation channel of the reactor HFIR was used as reference ($\Phi_{E>1MeV}$ = 7 10^{14} n.cm^{-2}.s^{-1}). The other neutron spectra were obtained by multiplying this reference by 0.01, 0.1 and 10 (Figure 3a). The procedure enables to study the flux effect without any changes in the spectrum shape.

The simulated irradiation-induced increases of yield stress are plotted versus the dose in Figure 3b. It can be observed that RPV-1 is sensitive to the neutron flux: the hardening increases as the neutron flux increases. It can also be observed that the flux dependence tends to decrease with decreasing flux and to become negligible between 0.1 x HFIR and 0.01 x HFIR. This trend is coherent with results obtained by Odette et al. in the same range of temperatures [1]. Figure 3c and d provide the final size distributions of the hardening defects after irradiation with the highest and lowest neutron fluxes. The role played by the point defects clearly grows with increasing flux.

1.5 - Sensitivity to the neutron spectrum

RPV-1 was run to simulate the irradiation response of a 0.1% Cu-1.3% Mn-0.7% Ni alloy at 288°C under two neutron spectra corresponding to the same dpa rate. The simulations were performed at 150°C with a dose up to 0.1 dpa. A neutron spectrum representative of an irradiation channel of the French experimental reactor OSIRIS ($\Phi_{E>1MeV}$ = 4.7 10^{12} n.cm^{-2}.s^{-1}) was used as reference, the other one was obtained by modifying a neutron spectrum representative of an irradiation channel of the reactor HERALD ($\Phi_{E>1MeV}$ = 5 10^{12} n.cm^{-2}.s^{-1}) so as to get the same dpa rate (≈ 6 10^{-9} dpa.s^{-1}) as the OSIRIS spectrum (Figure 4a).

The simulated irradiation-induced increases of yield stress are plotted versus the total fluence in Figure 4b. The two spectra induce slightly different hardenings, which shows that RPV-1 is sensitive to the shape of the neutron spectrum. This trend is coherent with the ESTEREL program as described in Chapter VI.

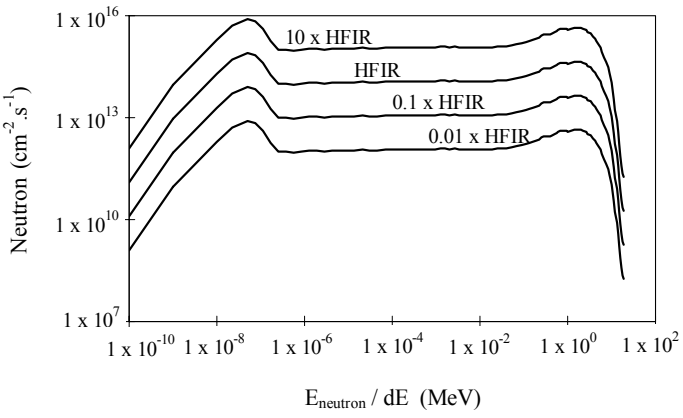

a)

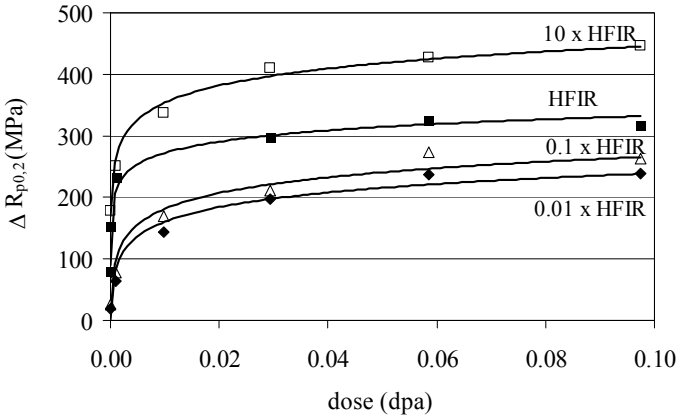

b)

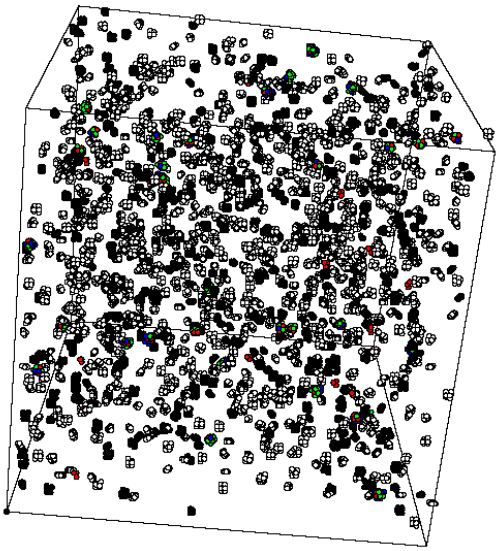

c)

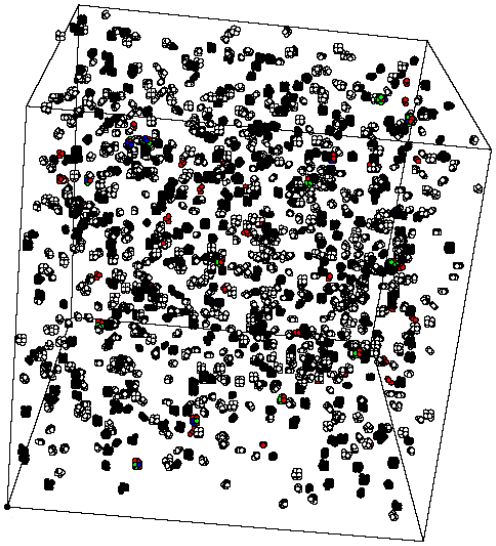

d)

Figure 3: sensitivity of RPV-1 to the neutron flux. Simulations performed at 55°C with the neutron spectrum representative of an irradiation channel of the reactor HFIR ($\Phi_{E>1MeV}$ = 7 10^{14} n.cm^{-2}.s^{-1}) and with three multiples of this neutron spectrum (steel: 0.05%Cu-1.3%Mn-0.7%Ni).

a) neutron spectra;

b) irradiation-induced increase of yield stress;

c) distribution of hardening defects for the 10 x HFIR spectrum and a dose of 0.1 dpa;

d) distribution of hardening defects for the 0.01 x HFIR spectrum and a dose of 0.1 dpa.

(vacancy: white, SIA: black; Cu: red, Mn: green, Ni: blue ; box size: 28.7 x 28.7 x 28.7 nm^3)

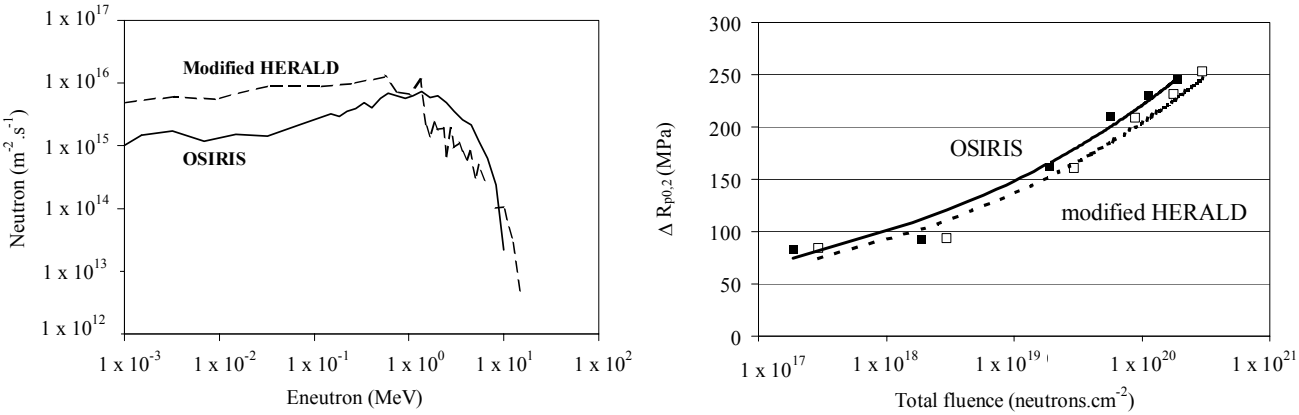

a) b)

Figure 4: sensitivity of RPV-1 to the neutron spectrum; simulations at 150°C with a neutron spectrum representative of an irradiation channel of the reactor OSIRIS ($\Phi_{E>1MeV}$ = 4.7 10^{12} n.cm^{-2}.s^{-1}) and one spectrum obtained by modifying a neutron spectrum representative of an irradiation channel of HERALD ($\Phi_{E>1MeV}$ = 5 10^{12} n.cm^{-2}.s^{-1}) so as to get the same dpa rate, namely 6.8 10^{-9} dpa.s^{-1} (steel : 0.1%Cu-1.3%Mn-0.7%Ni).

a) neutron spectra;

b) irradiation-induced increase of yield stress.

(vacancy: white, SIA: black; Cu: red, Mn: green, Ni: blue ; box size: 28.7 x 28.7 x 28.7 nm^3)

II - Quantitative character of the simulations

The quantitative character of the simulations was assessed with the version 1.3.b of RPV-1, by comparing experimental and simulation results obtained on pure iron, iron-copper model alloys and RPV steels. Several neutron spectra as well as large ranges of irradiation temperatures and fluxes were taken into account. A comparison with electron irradiation have also been performed. Only a part of this work is given here.

One should mention that all calculations were performed with the same “standard” parameterization (see Chapter II), which was not optimised in the framework of this thesis. The improvement of this parameterization is being done by the international community (e.g. [2]).

2.1 Electron irradiations

RPV-1 was run to reproduce an electron irradiation program carried out at 288°C by Akamatsu on Fe-0.1%Cu, Fe-0.7%Cu and Fe-1.4%Cu alloys [3]. Akamatsu used 3 MeV electrons at a dose rate of 4.8 10^{14} $cm^{-3}.s^{-1}$ and followed up the irradiation effects by hardness measurements. The electron irradiations were simulated with RPV-1 by creating single Frenkel pairs at rate of 4.8 10^{14} $cm^{-3}.s^{-1}$, which corresponds to a dose rate of 5.6 10^{-9} $dpa.s^{-1}$.

The simulated increases of yield stress of the three alloys are plotted versus the dose in Figure 5, where they are compared to the hardness measurements. The kinetics of hardening and the sensitivity to the Cu content are very well reproduced by RPV-1 The simulation results are quantitatively in agreement with the experimental ones if the experimental increase of yield stress is deduced from the hardness measurements by using the expression $\Delta R_{P0.2} = k\ \Delta H_V$ with $2 \leq k \leq 3$, such values of k are en agreement with published results [4, 5].

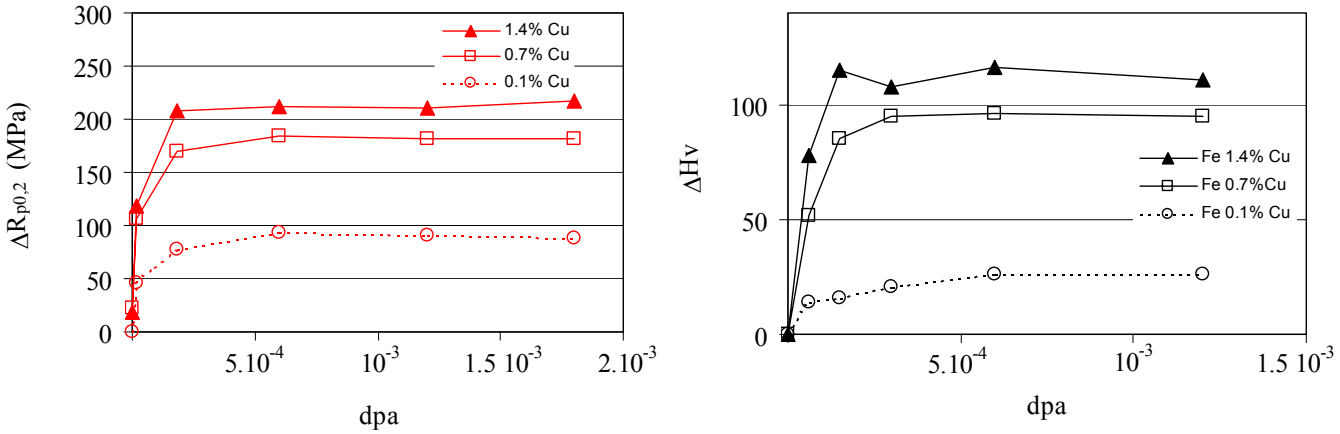

a) simulated evolution of yield stress b) experimental evolution of hardness [3]

Figure 5: simulation of electron irradiations at 288°C on Fe-0.1%Cu, Fe-0.7%Cu and Fe-1.4%Cu alloys with a dose rate of 5.6 10^{-9} $dpa.s^{-1}$, comparison with hardness measurements.

2.1 Neutrons irradiations

a) Pure iron

The conditions used to assess the quantitative character of RPV-1 on pure iron are summarized in Table II. Neutron spectra representative of irradiation channels of two experimental reactors were used: HFIR and OSIRIS. The simulation results and available experimental results are compared from Figure 6 to Figure 8. In all cases, simulation results fall

at about ± 20 MPa of the experimental ones, which is rather satisfactory (± 20 MPa can be considered as the statistical dispersion of experimental measurements of yield stress).

Eldrup et al. [6, 7] carried out TEM[1] and PA[2] microstructural characterizations on iron irradiated at about 60°C in HFIR. They were able to quantify the evolution of the density of dislocation loops (of radius higher than 0.5 nm) and vacancy clusters versus the dose. Their results are given in Figure 7 where they are compared to the simulation results obtained with RPV-1 for the same conditions. For both types of defect, experimental and simulation results exhibit the same dependence on the dose. The simulation correctly reproduces the number densities of vacancy clusters but overestimates those of SIA loops for doses higher than 10^{-3} dpa.

Table II: conditions used to assess the quantitative character of RPV-1 on pure iron.

Reactor	Flux (E > 1MeV) (10^{12} n.cm^{-2}.s^{-1})	Irradiation temperature (°C)	Ref.
HFIR	7 10^2	≈ 60	[6, 7, 8]
		150	
		300	
OSIRIS	4.7	288	[3]

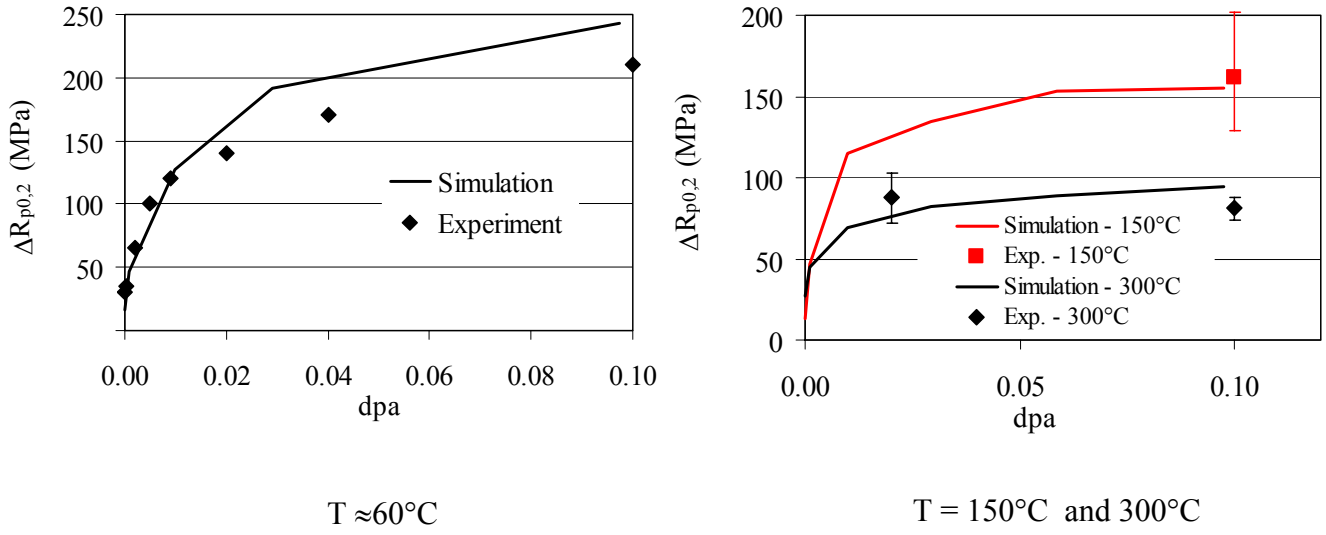

T ≈60°C T = 150°C and 300°C

Figure 6: simulated evolution of the yield stress of pure iron irradiated in a channel of HFIR ($\Phi_{E>1MeV}$ = 7 10^{14} n.cm^{-2}.s^{-1}) - comparison of experimental results [6, 7, 8].

[1] Transmission Electron Microscopy.
[2] Positron Annihilation.

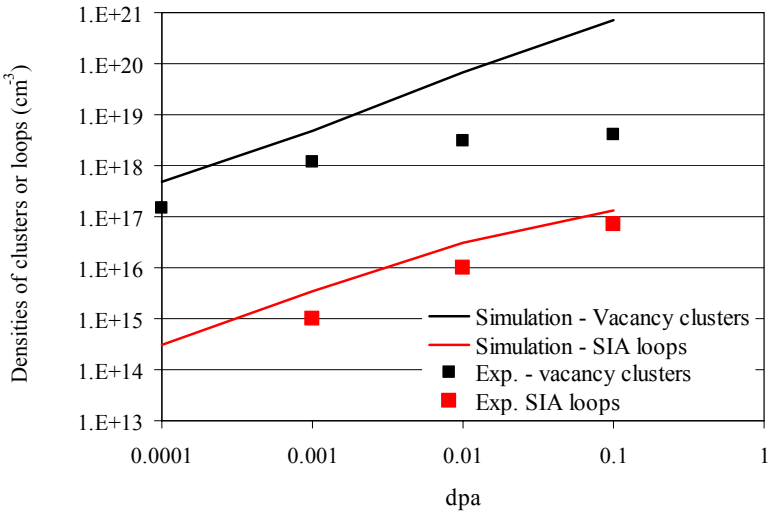

Figure 7: simulated evolution of the number densities of SIA-loops and vacancy-clusters in pure iron irradiated at 60°C in a channel of the reactor HFIR ($\Phi_{E>1MeV}$ = 7 10^{14} n.cm^{-2}.s^{-1}); comparison with experimental results [6].

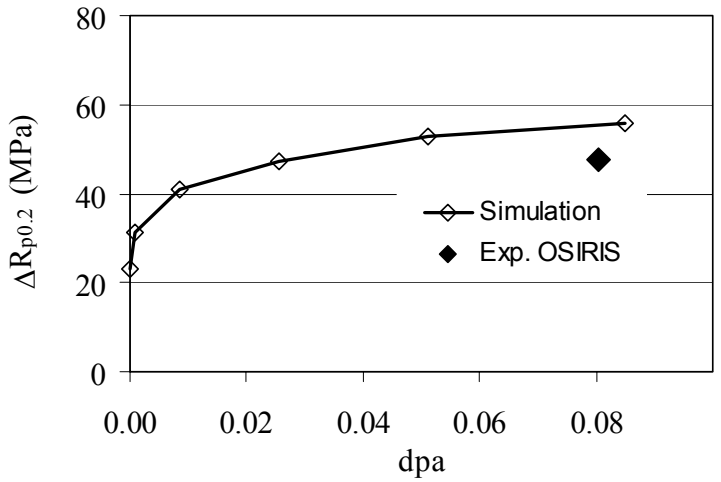

Figure 8 : simulated evolution of the yield stress of pure iron irradiated at 288°C in a channel of OSIRIS ($\Phi_{E>1MeV}$ = 4.7 10^{12} n.cm^{-2}.s^{-1}); comparison of experimental results [3] deduced from hardness measurements using the expression : $\Delta R_{P0.2} \approx 2.5\ \Delta Hv$ (cf. chapter IV).

b) Fe-Cu model alloys

The quantitative character of RPV-1 on model Fe-Cu alloys was assessed with a neutron spectrum representative of one irradiation channel of the experimental reactor HFIR; the irradiation conditions are summarized in Table III.

The simulation and experimental results are compared in Figure 9 and Figure 10. In all cases, the simulation results are in agreement with experimental ones and fall within the usual statistical dispersion of experimental irradiation programs ≈ ± 20 MPa.

Table III : conditions used to assess the quantitative character of RPV-1 on Fe-Cu alloys.

	Cu content	Irradiation Temperature	Ref
HFIR (experimental) 7 10^{14} n.cm^{-2}.s^{-1}	0.1	150 300	[9]
	0.3	60 300	[8]

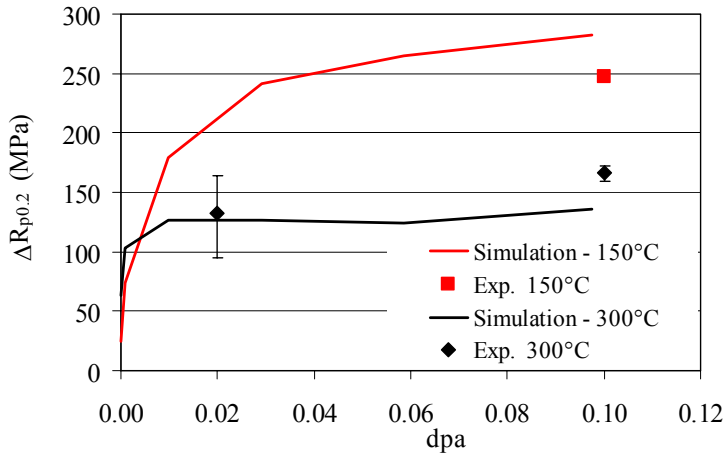

Figure 9: simulated evolution of the yield stress of an Fe-0.1%Cu model alloy, irradiated at 60 and 150°C in a channel of HFIR ($\Phi_{E>1MeV}$ = 7 10^{14} n.cm^{-2}.s^{-1}). Comparison with experimental results [8].

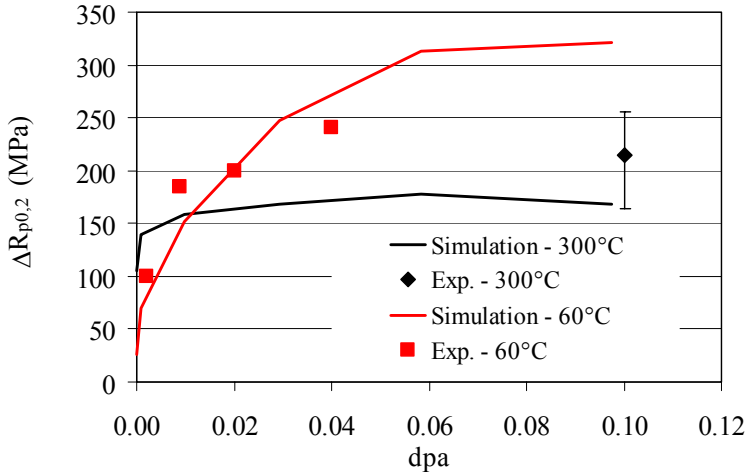

Figure 10: simulated evolution of the yield stress of an Fe-0.3%Cu model alloy, irradiated at 150°C and 300°C in a channel of HFIR ($\Phi_{E>1MeV}$ = 7 10^{14} n.cm^{-2}.s^{-1}). Comparison with experimental results [9].

c) RPV steels

The quantitative character of RPV-1 on RPV steels was assessed with neutron spectra representative of the irradiation channels of two experimental reactors: HFIR and HERALD ; the irradiation conditions are summarized in Table IV.

The simulated and available experimental results are compared Figure 11 and Figure 12. In any cases simulation results are in agreement with experimental ones and fall within the usual statistical dispersion of experimental irradiation programs ≈ ± 20 MPa.

Other examples of validation on RPV steels are given in Chapter VI.

Table IV: conditions used to assess the quantitative character of RPV-1 on RPV steels.

Reactor	Steel			Flux (E ≥ 1MeV)	Irradiation	Ref.
	Cu (%)	Mn (%)	Ni (%)	10^{12} n.cm^{-2}.s^{-1}	temperature (°C)	
HFIR	0.14	1.30	0.87	$7\ 10^{2}$	55	[8]
					300	[9]
HERALD	0.10	1.65	0.08	5	225	
	0.20	1.45	0.22	5		[10]

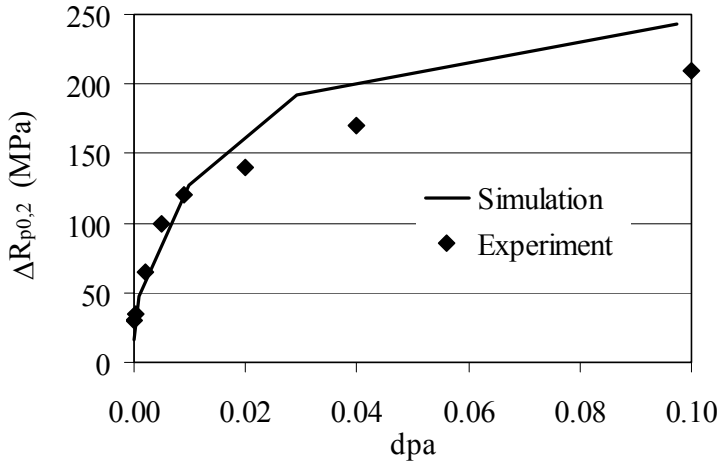

Figure 11: simulated evolution of the yield stress of a RPV steel irradiated at 55°C in a channel of HFIR ($\Phi_{E>1MeV}$ = $7\ 10^{14}$ n.cm^{-2}.s^{-1}), Cu = 0.14%, Mn = 1.30%, Ni=0.87%. Comparison with experimental results [8].

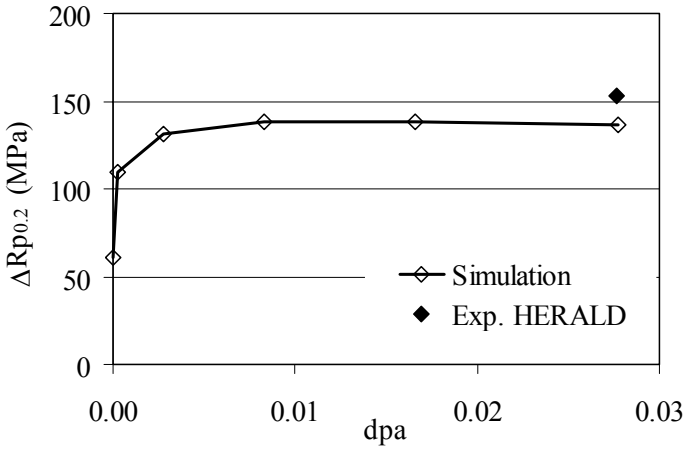

Figure 12: simulated evolution of the yield stress of a RPV steels irradiated in a channel of HERALD ($\Phi_{E>1MeV}$ = 5 10^{12} n.cm^{-2}.s^{-1}). Comparison with experimental results [10].

III - Errors and uncertainties

As described in previous chapters, RPV-1 relies on many hypotheses and contains errors as well as uncertainties which may alter the quantitative character of the simulations. It is noteworthy that these weaknesses are not critical for the development of VTRs. Indeed, continuous improvement of computer power and understanding of irradiation effects will help introduce more and more precise physical descriptions of the involved phenomena in the simulation. Concerning RPV-1, Table V summarizes some errors (in addition to the already described homogenizations) and uncertainties in the codes used to build it. A considerable effort would be required to quantify the effects of these errors and uncertainties on the simulation results. However, the previous section shows that these errors and uncertainties do not push the simulations results outside the usual statistical dispersion of experimental results.

Table V (part 1): some errors and uncertainties of the codes used to build RPV-1.

Code	Errors and uncertainties	Impact
SPECMIN	**Model errors**	
	BCA approximation	Not significant in PWR's range of neutron energies
	Neglecting alloying elements	Not significant in PWR's range of vessel compositions
	Lindhard model to calculate T_{damage}	Not significant in PWR's range of PKA energies
	Dpa definition	Not crucial if used to compare neutron spectra
	Numerical errors	Related to computer precision
	Programming errors	No
	Uncertainties	
	From the nuclear cross-sections	≈ 10% uncertainties on the results
	From neutron spectrum	Probably the main issue
INCAS	**Model errors**	
	BCA approximation	Not significant in the PWR's range of PKA energies
	Neglecting alloying elements	Not significant in the PWR's range of vessel compositions
	(Sub)-cascades definition	Not crucial if used to compare neutron spectra
	Imposed distribution of point defects produced between sub-cascades	Small effect on the results
	Numerical errors	Related to computer precision
	Programming errors	Still subject of attention
	Uncertainties	
	From the collision cross-section	≈ 10-20% uncertainties on the results
MFVISC	**Model errors**	
	Simplified capture radius	One of the main issues
	Neglecting the interactions between copper atoms and SIAs	May be an important source of error
	Use of continuous equation for larger clusters	Probably a weak effect
	Neglecting the multi-sink effect	May be an important source of error
	Neglecting the mobility of vacancy-copper clusters	Probably a weak effect
	Numerical errors	Related to computer precision
	Programming errors	Still possible (young code)
	Uncertainties	
	Bad knowledge of parameters (mobility of clusters, binding energies,..)	One of the main issues

Table V (part 2): some errors and uncertainties of the codes used to build RPV-1.

Code	Errors and uncertainties	Impact
DIFFG	**Model errors**	
	Cu, Mn and Ni activities calculated from binary mixtures, within an extended regular solution model	
	Interface energy calculated within a pair bond (nearest neighbour) regular solution model	
	Numerical errors	Related to computer precision
	Programming errors	No
	Uncertainties	
	Mixing enthalpies, entropies and free energies to describe bcc binary mixtures	Probably a weak effect - correction factors have been introduced
DUPAIR	**Model errors**	
	Constant line tension along the bowed dislocation segment	Probably a small effect when the number density of defects is high or when the obstacles are weak.
	No effect of the irradiation-induced damage on the Peierls friction stress	Probably a weak effect
	No possibility of cross-slip	Probably a weak effect
	Possibility to pass of small defects by thermal activation processes	Probably a weak effect
	Simulation with only one dislocation	Probably a weak effect
	Numerical errors	Related to computer precision
	Programming errors	Still subject of attention
	Uncertainties	
	Pinning forces of the obstacles	One of the main issues
DYMOKA	**Model errors**	
	Neglecting relativist effects	Probably no significant effect
	Neglecting electron-phonon interactions	Possible effect in the simulation of displacement cascades
	Numerical errors	Related to computer precision
	Programming errors	May still contain some minor errors
	Uncertainties	
	Inter-atomic potentials	Probably the main issue

Table V (part 3): some errors and uncertainties of the codes used to build RPV-1.

Code	Errors and uncertainties	Impact
LAKIMOCA	**Model errors**	
	Choice of the events accounted for in OKMC	Can be mastered
	Model for migration energies of vacancies in VKMC	One of the main sources of error
	Numerical errors	Related to computer precision
	Programming errors	May still contain some minor errors
	Uncertainties	
	Frequency of occurrence of events for OKMC	One of the main issues
	Inter-atomic potentials for VKMC	One of the main issues

IV - Conclusion

The results presented in this Chapter shows that RPV-1 is sensitive to most of its input parameters. The main issue is a bad dependence to nickel and manganese contents. Work is in progress to solve it.

It was also demonstrated that in a large range of irradiation conditions, RPV-1 provides results with a pretty good quantitative character: in most of the cases, the simulations results fall at about ± 20 MPa of the experimental ones (± 20 MPa can be considered as the statistical dispersion of experimental measurements of yield stress).

However, RPV-1 cannot strictly be considered as predictive tools due to many errors and uncertainties related to its codes. Work is in progress to rapidly solve the more penalizing ones.

References

1 Odette, G.R., "On the Effect of Flux and composition on Irradiation Hardening at 60°C", ASTM-STP 1270, (1996), p. 547.

2 Hardouin-Duparc, A., Mointgeon, C., Smetniansky-de-Grande, N., Barbu, A., J. Nucl. Mater., vol. 302, (2002) p. 143-155.

3 Akamatsu-Jousset, M., "Evolution Structurale d'Alliages Ferritiques sous Irradiation", PhD thesis, Université d'Orsay, (1994).

4 Pythian, W.J., Foreman, A.J.E., English, C.A., Buswell, J.T., Hetferington, M., Roberts, K., Pizzini, S., ASTM-STP 1125, (1992), p. 131.

5 Lucas, G.E., Odette, G.R., Maiti, R., Scheckerd, J.W., ASTM-STP 956, (1987), p. 379.

6 Eldrup, M., Singh, B.N., Zinkle, S.J., Byun, T.S, Farrell, K., J. Nucl. Mater., vol. 307-311, (2002), p. 912.

7 Eldrup, M., Singh, B.N., J. Nucl. Mater., vol. 323, (2003), p. 346.

8 Farrell, K., Mahmood , S.T., Stoller, R.E., Mansur, L.K., J. Nucl. Mater., vol. 210, (1994), p. 268.

9 Toloczko, M.B., Kumar, A. S., Hamilton, M.L., Jumel, S., van Duysen, J.C., Snead, L.L., Unpublished results.

10 Private communication.

CHAPTER VI

Answers to some questions of interest to the "RPV community"

As aforementioned, RPV-1 is still suffering from many weaknesses: poor parameterisation of the MFVISC Rate Theory code and DIFFG kinetic-thermodynamic code, rough approximation of the pinning forces, etc. However, it may already be used to reinforce or complement experimental irradiation programs. This chapter is aimed at demonstrating this capability by treating two examples of interest to the "RPV community":

- the determination of the best parameter to characterize the irradiation exposure of the pressure vessels and surveillance capsules of the French nuclear reactors;
- the understanding of the temperature effect on the irradiation-induced hardening.

The first example is treated by reproducing the French ESTEREL program and the second one by simulating irradiation effects at six temperatures on the same RPV steel. The presentation of these selected examples is preceded by some bibliography elements.

Due to the current weaknesses of RPV-1, we decided not to present any predictive results (even it was tempting to do so), but to focus on simulation results obtained in the range of irradiation conditions used in the experimental programs. The simulations were carried out with the version 1.3.c of RPV-1.

Results concerning the evolution of the irradiation-induced damage are illustrated in paragraph II, and III. For the sake of understanding, number densities of irradiation-induced defects have been plotted according to the following rules:

- number densities of SIA loops, vacancy clusters, copper precipitates and copper-rich precipitates are represented with solid lines;
- densities of copper-vacancy clusters are represented with dots. For a given number N of copper atoms in the cluster, the first dot of highest density corresponds to the density of clusters containing N copper atoms and 1 vacancy, the second one to the density of clusters containing N copper atoms and 2 vacancies, etc, ….

I - Bibliography elements

1.1 - Characterization of irradiation exposure

To compare results of irradiation programs on materials, it is necessary to characterize the irradiation exposures with a parameter well correlated to the damage induced by the neutron, and thus to the concomitant evolution of the mechanical properties. Several exposure parameters have been proposed, for example a survey can be found in [1]. The currently used parameters are mostly: the fluence and the number of displacements per atom (dpa).

The fluence is the number of neutrons received per surface unit of the irradiated material (neutrons.cm^{-2}); it is called flux when expressed per time unit (neutrons.cm^{-2}.s^{-1}). Usually, only neutrons of energy higher than a threshold value are considered, supposing that the others have a negligible effect on the irradiated material. For LWR pressure vessels, threshold values of 1, 0.5, 0.68 or 0.1 MeV have firstly been proposed, depending on the country [2, 3, 4, 5]. In particular, Serpan et al. [2] showed that a threshold of 1MeV is acceptable for fission spectra with a ratio thermal to fast (E > 1MeV) neutron fluxes smaller than about 10. Currently, threshold values of 1 and 0.5 MeV are used in Western and Eastern countries, respectively. In the following sections, the fluences will be noted $\phi_{E>1MeV}$, $\phi_{0.1MeV,}$ etc.

The number of dpa (also called dose) was put forward to characterize the irradiation exposure with a better description of the irradiation-induced damage than the fluence. It is equal to the total number of Frenkel pairs (one vacancy + one self-interstitial atom) created in a given volume by the irradiating particles (neutrons but also electrons or ions,…), divided by the number of atoms in this volume. Several models have been set forth to calculate the number of produced Frenkel pairs depending on the energy of the incident particle (e.g. [6, 7, 8]); the most commonly used is that proposed by Norgett, Robinson and Torrens leading to the so-called NRT-dpa (e.g. [9, 10, 11, 12]). In the following sections, the number of NRT-dpa will be noted ϕ_{dpa}. This number is usually called dose rate when expressed by time unit (dpa.s^{-1}).

ϕ_{dpa} appeared to be a relevant quantity to characterize irradiation exposure of iron-based alloys (stainless steels, ferritic steels,…), independently of the type of irradiating particles (neutron, electrons, ions) [13, 14] and of the shape of their spectra [5, 15]. For

example, it was successfully used to interpret the responses of RPV-steels irradiated with strongly thermalized neutron spectra[1] [16, 17, 18] or in presence of intense γ flux[2] [19, 20, 21].

1.2 - French pressure vessel surveillance program

As most utilities, Electricité de France is running a surveillance program for all its nuclear power plant pressure vessels (e.g. [22]). This program is based on the use of 4 capsules which are installed in each reactor before the commissioning, and then removed periodically during the lifetime of the reactor. The capsules contain mechanical test specimens (Charpy, tensile and CT specimens), machined in materials representative of the vessel (i.e. base metal, weld and heat affected zone), and are monitored in terms of dosimetry and temperature. They are located along the core barrel and are closer to the fuel assemblies than the vessel. Consequently, small neutron spectrum differences between the vessel and the capsules are observed: i) the shape of the neutron spectrum in the capsule is degraded to the lower energies compared to the spectrum on the vessel (Figure 1) and ii) the neutron flux is higher in the capsule than on the vessel. Due to the difference of flux, the results of the mechanical tests carried out on the surveillance test specimens allow to anticipate the behaviour of the vessel.

The flux factor between the capsules and the vessel, also called the lead factor, depends on the threshold energy considered to calculate the fluence. It is worth about 3 for E ≥ 1MeV and 4.8 for E ≥ 0.1 MeV. Regarding the dose rate, the lead factor is about 3.3. The anticipation character of the surveillance program therefore strongly depends on the selected irradiation exposure parameter, e.g.: 10 years of irradiation in a surveillance capsule may represent respectively 32 or 48 years of service for the vessel if $\phi_{E>1MeV}$ or $\phi_{0.1MeV}$ is considered. This is why it is of paramount importance to determine the relevant irradiation exposure parameter.

One of the objectives of the ESTEREL program was to confirm that the $\phi_{E>1MeV}$ is the best exposure parameter to assess the behaviour of pressure vessels from the results of the surveillance programs.

---

1 Thermal neutrons induce atomic displacements from their collisions with atoms but also from lower energy recoils (of about 500 eV) associated with the Fe^{56} (n, γ) reaction as well as from the B^{10} (n, α) reaction producing Li^7 and He^4 transmutation products with energies 0.87 MeV and 1.53 MeV respectively. For strongly a, the determination of the irradiation dose may require to take into account the three contributions : dpa = dpa_{NRT} + dpa $_{Fe56\,(n,\gamma)}$ dpa $_{B10\,(n,\alpha)}$.

2 γ rays with energies ≤ 10MeV can produce damage in metals via several mechanisms. The most important source of damage for reactor pressure vessels are likely to be the Compton scattering of free electrons and the production of electron.-positron pairs. The energetic electrons produced by these processes internally bombard the material and create atomic displacements.

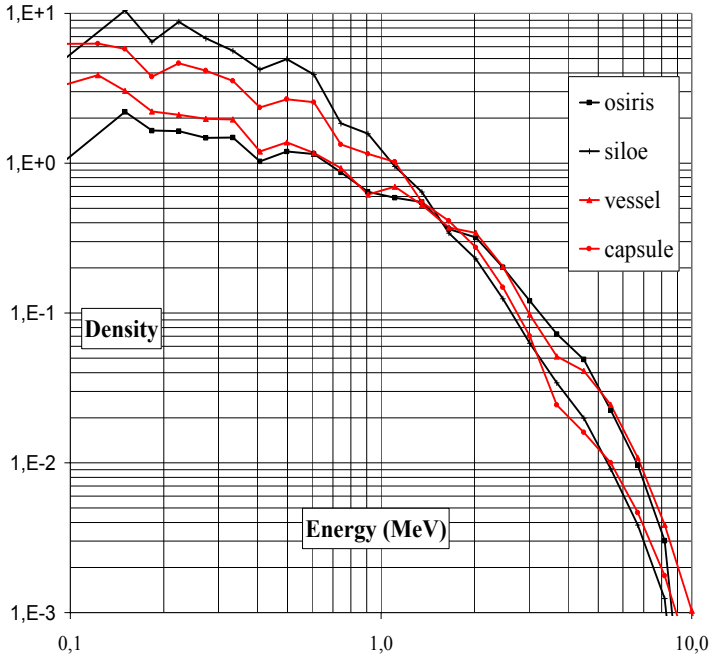

Figure 1: normalized neutron spectra in the surveillance capsules and on the inner side of the French pressure vessels as well as in the irradiation channels of OSIRIS and SILOE used in the ESTEREL program.

II -The ESTEREL program

The ESTEREL program was carried out between 1989 and 1995 by the Commissariat à l'Energie Atomique (CEA) and Electricité de France (EDF) [23]. Its aim was twofold :

- to quantify the neutron spectrum effect between the surveillance capsules and the pressure vessel;
- to define which is the most appropriate irradiation exposure parameter ($\phi_{E>1MeV}$, $\phi_{0.1MeV}$, ϕ_{dpa}) to assess the behaviour of pressure vessels from the results of surveillance program.

The experimental conditions had to be as close as possible to the in-service conditions, so as to ensure that the results are as representative as possible.

In order to meet these objectives, special devices (IRMA rigs, …) were developed and all experimental parameters were controlled with an extreme care: irradiation temperature (288±5°C), neutron environment as well as materials to be irradiated (two welds were specifically manufactured). The ESTEREL program was a large technical and financial effort for the "French RPV community". In order to support its conclusions, we reproduced it with RPV-1.

In this paragraph, we firstly remind the experimental work and the main conclusions of ESTEREL and then we describe the simulation work and the main results it provided.

2.1 - The experimental program

To meet the ESTEREL objectives, two low-alloyed welds were irradiated in two different neutron conditions.

a) Description of the irradiated materials

Two low-alloyed Mn Ni Mo welds, named M1 and M2, were prepared with a manufacturing process (welding conditions, heat treatments,…) similar to that undergone by the French pressure vessel welds. Welds were preferred to base metals for their better metallurgical and mechanical homogeneities.

The chemical compositions of M1 and M2 are given in Table I. The two materials are low copper steels and have a small difference of copper content Cu = 0.048 % for M1 and Cu = 0.095 % for M2 . Their irradiation-responses were studied in terms of:

- Charpy Ductile Brittle Temperature Transition (DBTT) shifts. For each condition (materials and reactor), transition curves were determined with 30 specimens; 15 of them were broken in the transition zone so as to determine precisely the DBTT;
- Yield stress increases. For each condition (material and reactor), 2 specimens were tested at -80°C, -40°C, 20°C, 100°C, 290°C. Only the results obtained at 20°C will be used in the following sections.

Table I: chemical compositions of materials M1 and M2 (weight %).

	C	Si	Mn	P	S	Ni	Cr	Mo	Co	Cu	V
RCC-M ed. 95	<.100	.15-.60	.80-1.80	<.010	<.025	<1.20	<.30	.35-.65	<.03	<.07	<.02
M1	.073	.43	1.59	.008	.008	.76	.16	.58	.010	.048	.003
M2	.058	.49	1.48	.020	.009	.68	.04	.54	.017	.095	.001

b) Description of the irradiation conditions

Two experimental French reactors were used to carry out the ESTEREL program:

- the OSIRIS reactor (CEA-Saclay), using an irradiation channel with a neutron spectrum representative of that on the inner side of the French vessel;

- the SILOE reactor (CEA-Grenoble), using an irradiation channel equipped with a steel shield aimed at "distorting" the neutron spectrum to get: i) a neutron spectrum representative of that in the French surveillance capsules and ii) a dpa rate similar that of the OSIRIS spectrum.

The spectra in both locations are shown in Figure 1 where they are compared to those of the French power reactors. Spectra on the vessel and in OSIRIS, on the one hand, as well as spectra in the surveillance capsules and in SILOE, on the other hand, have very similar shapes. For neutrons with energy lower then 1 MeV, the OSIRIS and SILOE spectra accentuate the difference between the spectra in the capsules and on the vessel.

The irradiations of the rigs lasted 185 and 187 Effective Full Power Days (EFPD) in SILOE and OSIRIS, respectively. It was expected that these time spans and the stacks of samples in the irradiation rigs would allow each weld to be irradiated with the same number of dpa in both reactors.

c) Results of the ESTEREL program

Due to the slight difference of copper content between M1 and M2 and the slight difference between the two spectra, very small discrepancies between the measured irradiation-responses were expected. The challenge of the ESTEREL program was to reveal and to quantify them.

Table II gives the DBTT shifts [measured at 56 joules (ΔTK7) and at 0.9 mm of lateral expansion (ΔT0.9)] and the yield stress increases of M1 and M2 after irradiation in each reactor, versus several exposure parameters. It can be noticed that :

- in spite of the extreme care in the control of the irradiation conditions, the fluence E > 1MeV and the number of dpa received by each weld is about 18% higher in OSIRIS than in SILOE;
- for each condition (material and reactor), the two methods of measurement of the DBTT shift lead to similar results;
- the embrittlement of each weld is higher after the OSIRIS irradiation than after the SILOE one.

For both materials, the higher embrittlement obtained in OSIRIS than in SILOE complies with the difference of fluence E > 1 MeV and number of dpa obtained in both reactors. However, the fluence E > 0.1MeV is 20% lower for OSIRIS than for SILOE, which indicates that this fluence is totally inadequate to assess the behaviour of pressure vessels from the surveillance program.

Table II: increase of yield stress and DBTT shifts (at 56 joules and 0.9 mm of lateral expansion) of materials M1 and M2, versus irradiation exposure parameters in OSIRIS and SILOE.

Weld	Reactor	$\Delta R_{P0.2}$ (MPa)	ΔTK7 (°C)	ΔT0.9 (°C)	mdpa	$\phi \geq 1$ MeV (10^{19} n. cm^{-2})	$\phi \geq 0.1$ MeV (10^{19} n. cm^{-2})
M1	SILOE	79.0	45.0	49.0	70.0	3.51	18.20
	OSIRIS	86.0	54.0	59.0	87.0	5.98	14.50
	Difference OSIRIS-SILOE	+ 7	+ 9	+ 10	+ 17	+ 2.47	- 3.70
M2	SILOE	110.0	59.1	71.3	81.5	4.09	21.20
	OSIRIS	130.0	72.7	87.6	100.0	6.86	16.70
	Difference OSIRIS-SILOE	+ 20	+ 13.6	+ 16.3	+ 18.5	+ 2.77	-4.5

TK7 : ductile brittle transition temperature measured at 57 joules.
ΔT0.9 : ductile brittle transition temperature measured at 0.9 mm of lateral expansion.

d) Analysis of the experimental results

As mentioned in the previous section, $\phi_{E>0.1MeV}$ could be easily discarded but a more refined analysis was needed to determine whether $\phi_{E>1MeV}$ or ϕ_{dpa} is the most appropriate exposure parameter.

The initial aim of the project was a direct comparison of the embrittlement levels induced by the irradiations in OSIRIS and SILOE, at the same number of dpa. As this number was about 18 % lower in the SILOE irradiation, this direct comparison was not possible. To overcome this difficulty, the embrittlement levels produced in SILOE were extrapolated at the same number of dpa as in OSIRIS (from 70 to 87 mdpa for M1 and from 81.5 to 100 mdpa for M2) using the expression $\Delta DBTT_{Average} = K (\phi_{dpa})^{0.4}$, where $\Delta DBTT_{Average}$ is the average of the ΔDBTTs determined at 56 joules and at 0.9mm of lateral expansion, K is a material-dependant constant. Similar derivation was made to compare the embrittlement levels at the same $\phi_{E>1MeV}$. Results are given in Table III. For both materials, it can be noticed that the same ϕ_{dpa} leads to a slightly larger embrittlement in OSIRIS than in SILOE, while $\phi_{E>1MeV}$ gives very similar results. This suggests that $\phi_{E>1MeV}$ is the best exposure indicator to assess the behaviour of the pressure vessels from the results of their surveillance program. In all the cases, the spectrum effect between both locations is rather low (some degrees on the ΔDBTT).

Table III : comparison between the ΔDBTT induced by the OSIRIS irradiation and the ΔDBTT extrapolated at the same dose and fluence from the results of the SILOE irradiation.

	OSIRIS	SILOE	
Materials	$\Delta DBTT^*_{Average}$ ($\Phi_{dpa}/\Phi_{E>1MeV}$)	$\Delta DBTT^*_{Average}$ extrapolated to the same Φ_{dpa} and $\Phi_{E>1\ MeV}$ as in OSIRIS	
		Same Φ_{dpa}	Same $\Phi_{E>1\ MeV}$
M1	56.5 °C (87 mdpa/5.98 10^{19} n.cm^{-2})	51.3°C	58.2°C
M2	80.2 °C (100 mdpa/6.86 10^{19} n.cm^{-2*})	70.8°C	80.2°C

* average of the ΔDBTTs determined at 56 joules and at 0.9mm of lateral expansion.

2.2 A simulated version of the ESTEREL program

The ESTEREL program was reproduced with RPV-1. As for the experimental program, the challenge was to reveal and to quantify the very small discrepancies between the irradiation-responses of M1 and M2 in both reactors and to interpret them. This section gives the conditions of the simulations and the obtained results.

a) Simulations carried out

RPV-1 was run using the OSIRIS and SILOE neutron spectra (Figure 1) and the chemical compositions of M1 and M2. The simulations were carried at out 288°C with a dose up to 110 mdpa.

b) Results of the simulations

The simulated increases of yield stress of both materials after irradiation are reported in Figure 2 (versus the number of dpa), where they are compared to the increases of yield stress measured at 20°C and calculated from the DBTT shifts with the expression $\Delta DBTT = 0.6\ \Delta R_{P0.2}$. [24]. All these results are summarized in Figure 3.

It can be noticed that :

- in spite of the small difference of copper contents between both materials, RPV-1 correctly reproduces the higher irradiation-sensitivity of M2 compared to M1 for both neutron spectra, as observed experimentally.
- the quantitative character of the simulations is acceptable. The simulated results fall at most at 30 MPa of the experimental ones (Figure 2).
- for both materials, the simulation with the OSIRIS spectrum induces an slightly larger increase of yield stress than with the SILOE one at the same dpa, as observed experimentally (Figure 3).
- the simulation confirms that the spectrum effect is weak.

c) Determination of the best exposure parameter

The increases of yield stress of M1 and M2 simulated from both spectra are plotted versus $\phi_{E>1MeV}$, $\phi_{E>0.5MeV}$, $\phi_{E>0.1MeV}$ or ϕ_{dpa} in Figure 4 and Figure 5. For a given material, the most appropriate exposure parameter is the one for which the trend curves drawn for both spectra are the closest. It can be observed that this condition is reached when $\Delta R_{P0,2}$ is plotted versus $\phi_{E>1MeV}$. The visual impression can be confirmed by calculating the regression coefficients (R^2) of the trend curve relying on all the simulated results obtained from both spectra (see as an example Figure 4e and f as well as Figure 5e and f). Table IV shows that R^2 is the largest (thus the results obtained from the two spectra are the most consistent) when $\Delta R_{P0,2}$ is plotted versus $\phi_{E>1MeV}$. The result obtained with the dpa is very good as well.

Despite the small differences between the two materials and between the two spectra, the simulations carried out with RPV-1 confirmed the results of the ESTEREL program. In particular, they showed that the fluence E > 1 MeV is a more appropriate exposure parameter than $\phi_{E>0.1MeV}$ and ϕ_{dpa} to compare the irradiations between the surveillance capsule and the pressure vessel of the French nuclear reactors.

Table IV : effect of the exposure parameter on the regression coefficient of the trend curve relying on all the simulation results obtained from the OSIRIS and SILOE neutron spectra.

	$\phi_{E>1MeV}$	$\phi_{E>0.5MeV}$	$\phi_{E>0.1MeV}$	ϕ_{dpa}
M1	0.993	0.964	0.908	0.986
M2	0.988	0.955	0.903	0.979

d) Interpretation of the simulation results

An analysis of the irradiation-induced defects "produced" by RPV-1 in each material has been carried out by comparing their distributions, for a same $\phi_{E>1MeV}$, $\phi_{E>0.1MeV}$ or ϕ_{dpa}. Examples concerning the materials M1 and M2 are given in Figure 6 and Figure 7. For both materials, it has been noticed that :

- the distributions of copper precipitates induced by both species are the closest when considering $\phi_{E>1MeV}$ as exposure parameter.
- the OSIRIS spectrum leads to a larger number density of vacancy clusters than the SILOE one. The difference between the two distributions of these clusters is almost independent of the exposure parameters.
- the distributions of SIA loops induced by the two spectra are almost similar, whatever the exposure parameter.
- the copper precipitates have the major contribution in the increase of yield stress. Indeed, their number density is always significantly larger than that of the other defects, in the size range in which they have a hardening effect (i.e. loops containing more than 19 SIAs, etc).

In conclusion, it appears that $\phi_{E>1MeV}$ is a much more appropriate exposure parameter than $\phi_{E>0.1MeV}$ because it is better correlated to the irradiation-induced precipitation of copper. The ϕ_{dpa} is also a quite good parameter. The small difference of hardening noticed for a same $\phi_{E>1MeV}$ results from a larger number density of vacancy clusters after the irradiation in OSIRIS than in SILOE. According to these conclusions, the relevance of $\phi_{E>1MeV}$ as the best exposure parameter should increase with the copper content.

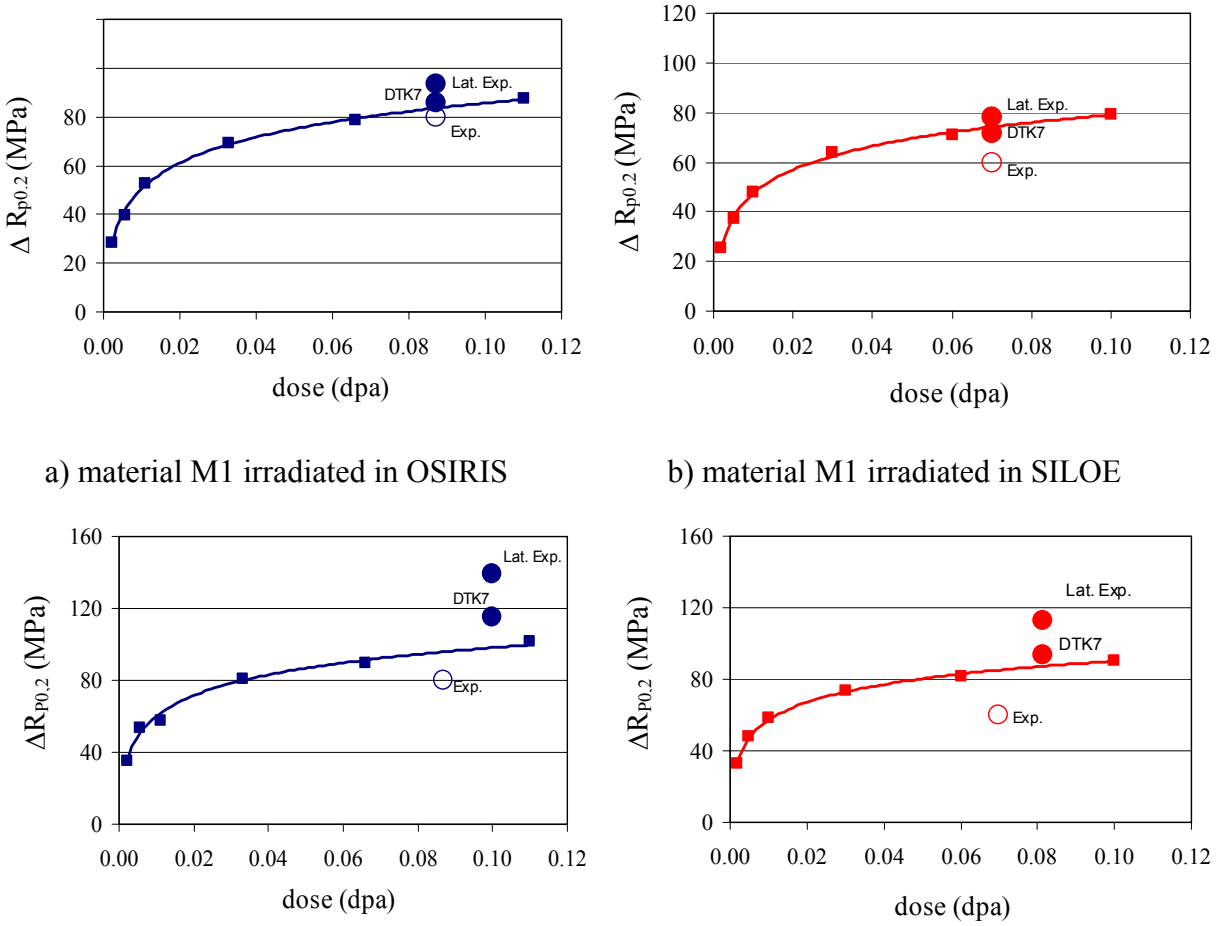

a) material M1 irradiated in OSIRIS

b) material M1 irradiated in SILOE

c) material M2 irradiated in OSIRIS

d) material M2 irradiated in SILOE

Figure 2 : comparison of simulation (squares and curves) and experimental (circles) results.

Lat. Exp.: increase of yield stress deduced from the DBBT shift measured at 0.9mm of lateral expansion.

DTK7 : increase of yield stress deduced from the DBBT shift measured at 56 joules.

Exp : increase of yield stress measured by tensile test.

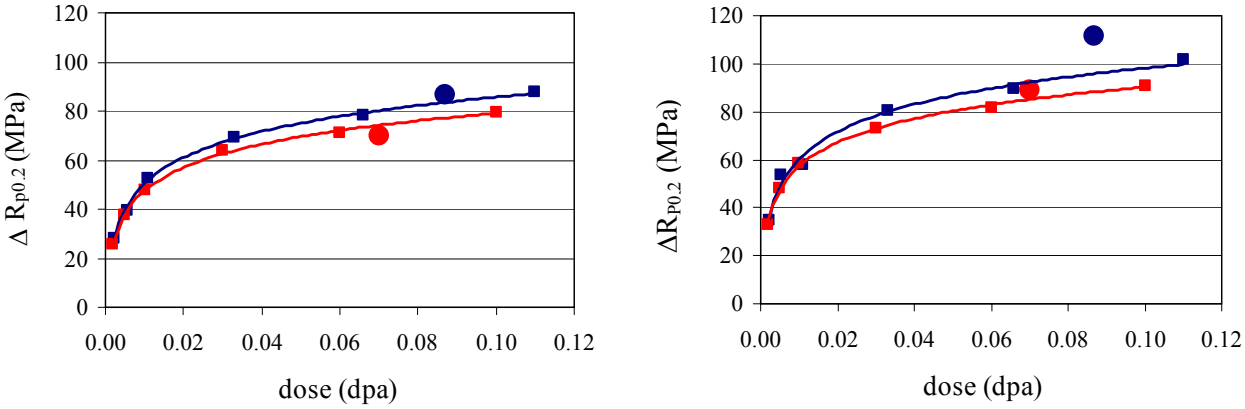

a) material M1 b) material M2

Figure 3: summary of the comparison between the simulation (squares and curves) and experimental results (circles).
Blue: OSIRIS - Red: SILOE. Circle: average of the increases of yield stress measured experimentally or determined from the DBTT shifts measured at 56 joules and at 0.9mm of lateral expansion.

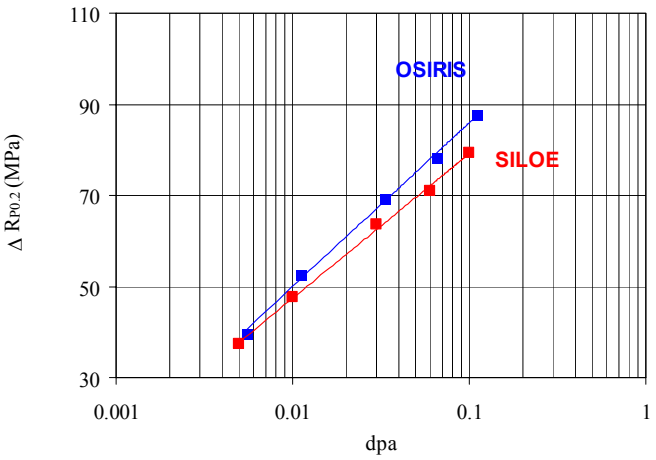

a) same number of dpa

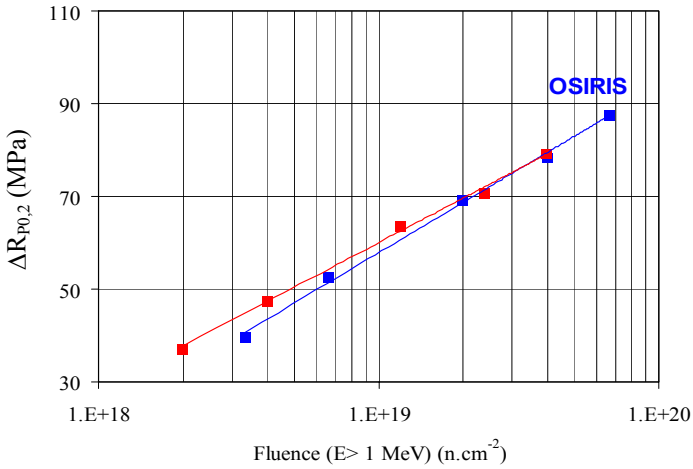

b) same fluence E> 1MeV

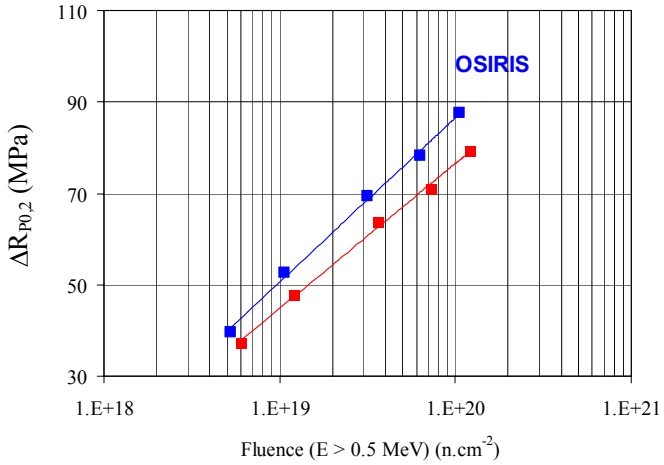

c) same fluence E > 0.5 MeV

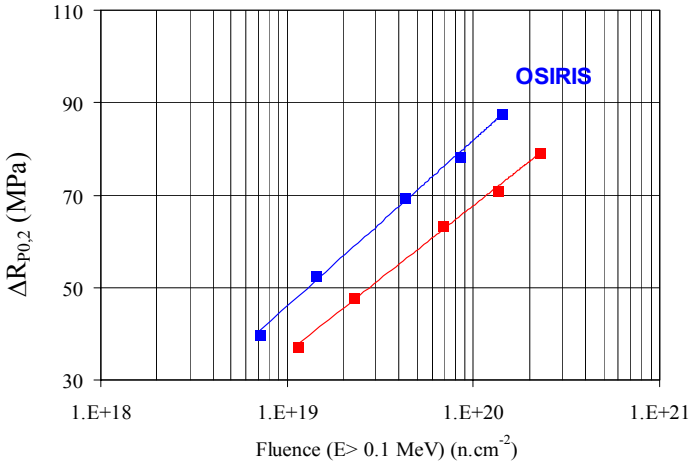

d) same fluence E > 0.1 MeV

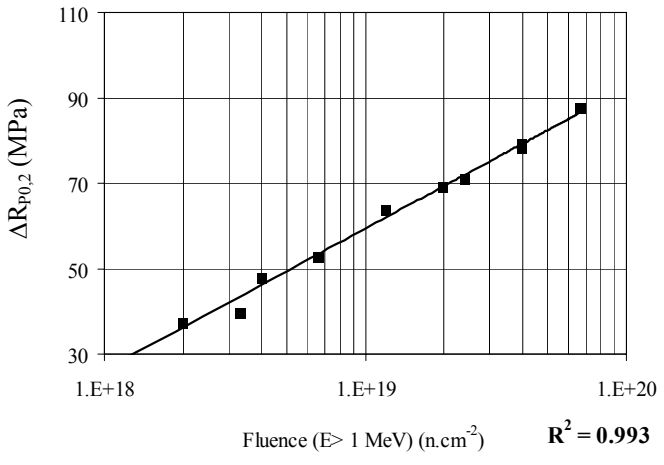

e) trend curve relying on all simulation results obtained form the OSIRIS and SILOE spectra and plotted versus $\phi_{E>1MeV}$

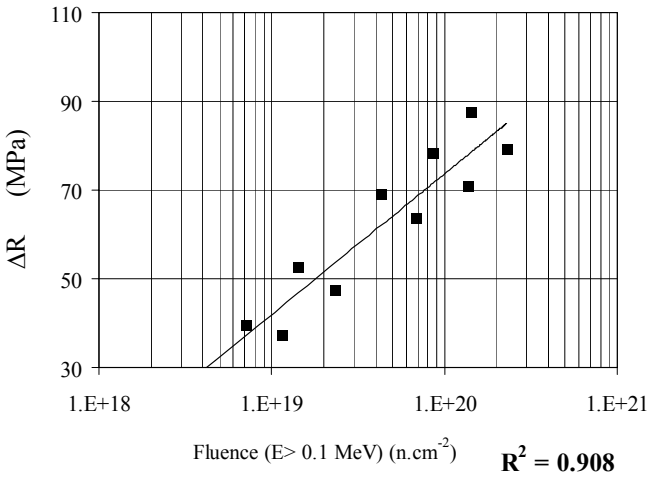

f) trend curve relying on all simulation results obtained form the OSIRIS and SILOE spectra and plotted versus $\phi_{E>0.1MeV}$

Figure 4: simulated increase of yield stress of material M1 after irradiation in OSIRIS or SILOE, versus several exposure parameters.

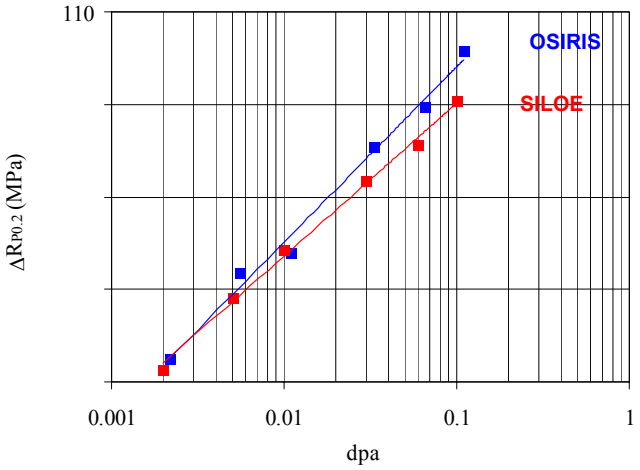

a) same number of dpa

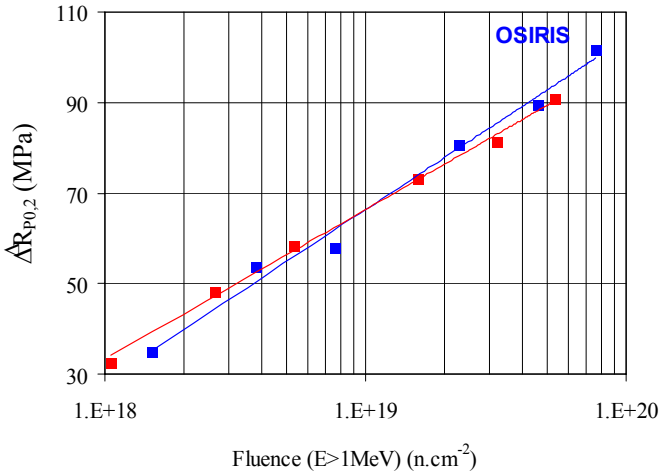

b) same fluence E> 1MeV

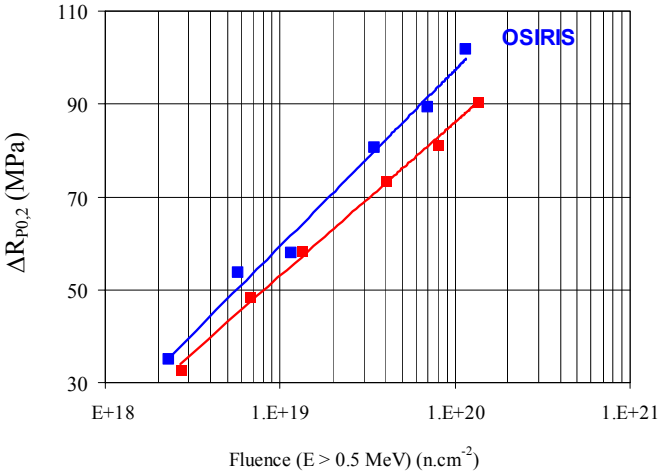

c) same fluence E > 0.5 MeV

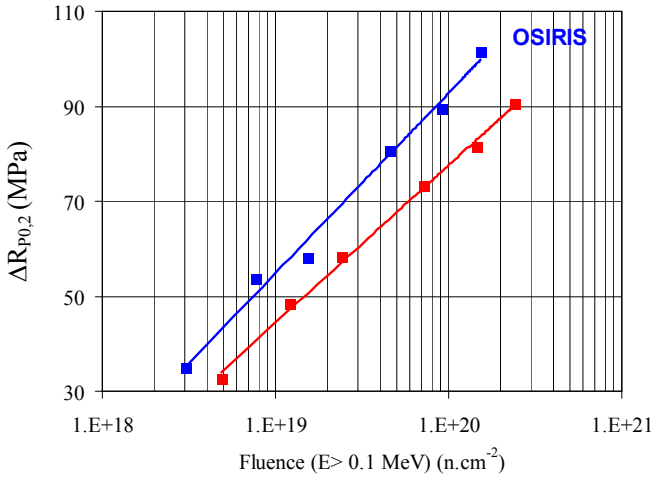

d) same fluence E > 0.1 MeV

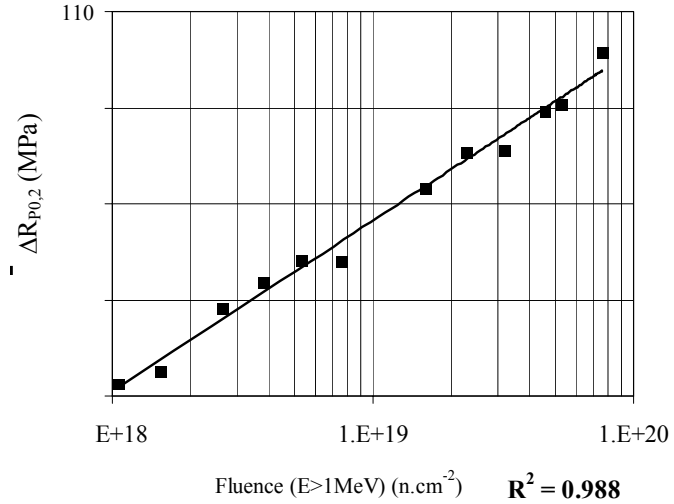

e) trend curve relying on all simulation results obtained form the OSIRIS and SILOE spectra and plotted versus $\phi_{E>1MeV}$

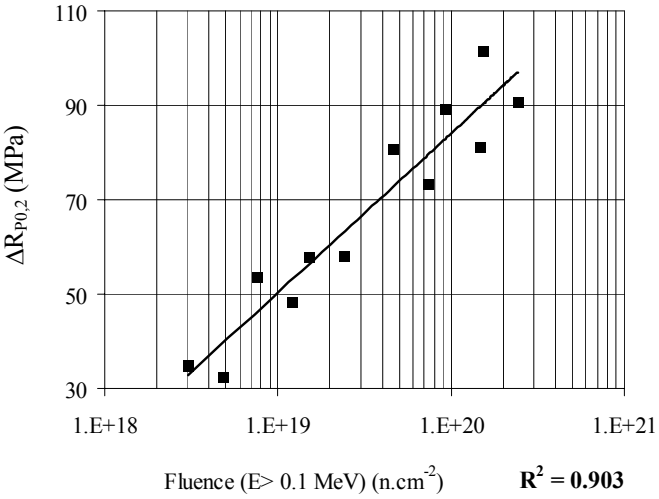

e) trend curve relying on all simulation results obtained form the OSIRIS and SILOE spectra and plotted versus $\phi_{E>0.1MeV}$

Figure 5: simulated increase of yield stress of material M2 after irradiation in OSIRIS or SILOE, versus several exposure parameters.

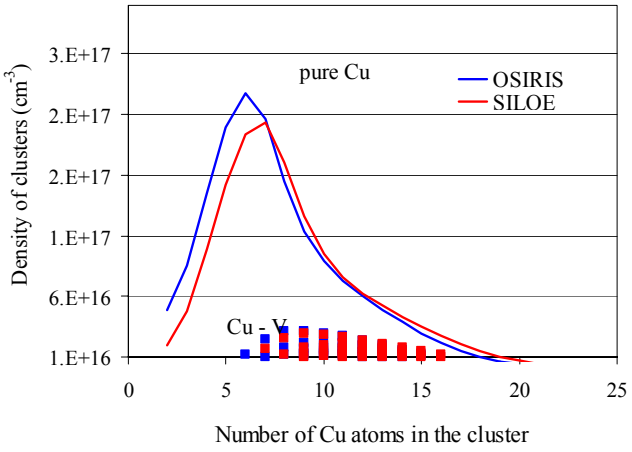

a) copper precipitates and vacancy-solute atoms

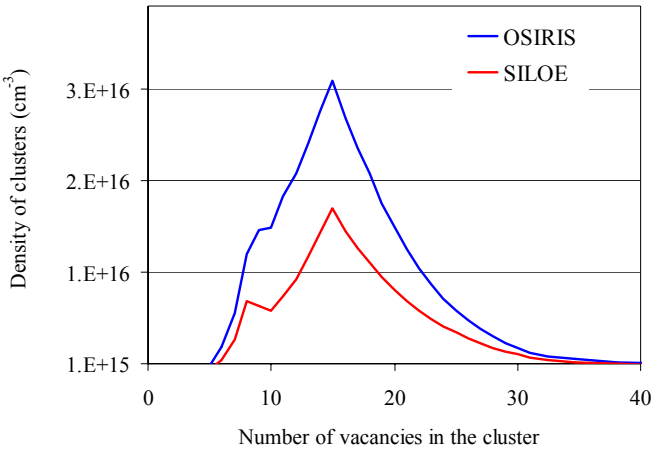

b) vacancy clusters

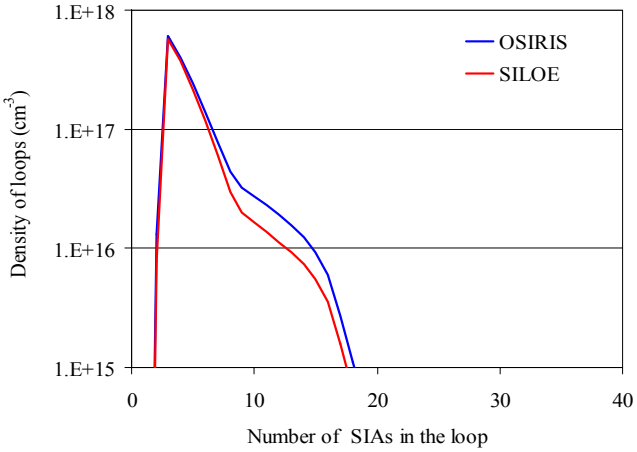

c) SIA loops

Figure 6: material M1 - comparison of the irradiation-induced defects simulated from the OSIRIS (blue) and SILOE (red) spectra for a same exposure parameter ϕ (E>1MeV) = 4.4 10^{19} n.cm^{-2}.s^{-1}. The copper-rich precipitates and the vacancy-solute clusters are described by their number of copper atoms.

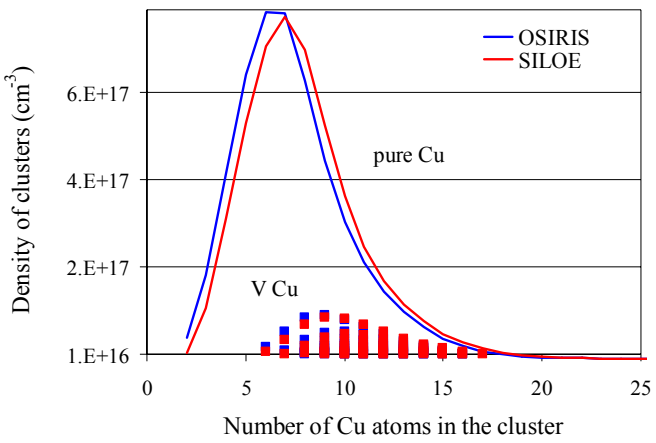

a) copper precipitates and vacancy-solute atoms

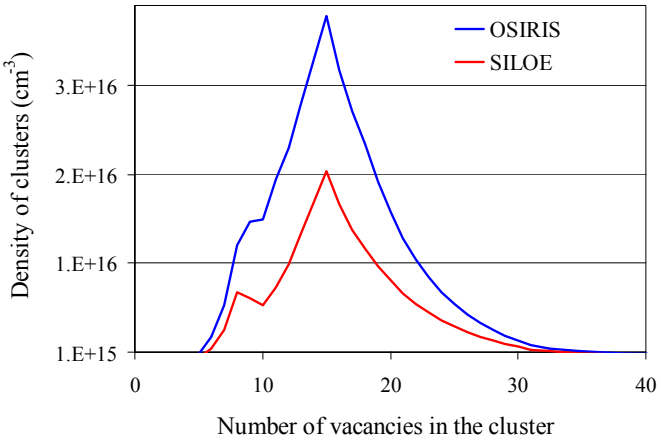

b) vacancy clusters

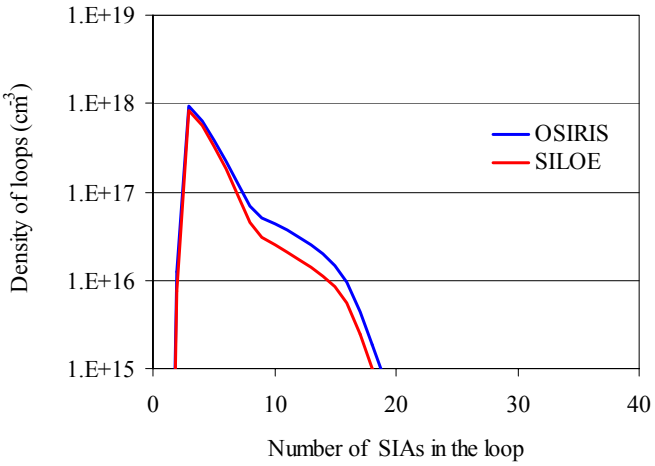

c) SIA loops

Figure 7: material M2 - comparison of the irradiation-induced defects simulated from the OSIRIS (blue) and SILOE (red) spectra for a same exposure parameter ϕ (E>1MeV) = 4.4 10^{19} n.cm^{-2}.s^{-1}. The copper-rich precipitates and the vacancy-solute clusters are described by their number of copper atoms.

III - Analysis of the irradiation temperature effect

Many experimental programs [25, 26, 27] were carried out to assess the effect of the irradiation temperature on the irradiation-induced response of RPV steels. As explained in Chapter I, the obtained results showed that the temperature dependence of DBTT shift and of the increase of yield stress are around 1.0 ± 0.6 °C/°C and 1.5 ± 1.0 MPa/°C respectively [25, 26, 27, 28]. However, very few descriptions of the mechanisms controlling this temperature effect have been proposed. RPV-1 was used to analyze these mechanisms.

3.1 - Simulations carried out

RPV-1 was run to simulate the irradiation-response of a 0.065%Cu-1.3%Mn-0.7%Ni steel, at six temperatures: T = 55, 100, 150, 200, 288 and 350°C. The simulations were performed with a neutron spectrum representative of an irradiation channel of the reactor OSIRIS ($\Phi_{E\geq 1MeV} = 4.7\ 10^{12}$ n.cm^{-2}.s^{-1}) up to a dose of 0.11 dpa.

3.2 - Results of the simulations

The increases of the yield stress have been plotted versus the number of dpa in Figure 8a for the six irradiation temperatures. They have also been plotted versus the temperature in Figure 8b for doses of 0.06 and 0.11 dpa. In the 55-350°C range, the temperature dependence averages about 1 MPa/°C, which is in good agreement with experimental results. However, three regimes can be observed in Figure 8b :

- between about 50 and 100°C, where the temperature dependence is weak ≈ 0.4 MPa/°C;
- between about 100 and about 250°C, where the steel response is more temperature dependent ≈ 1.8 MPa/°C;
- between about 250 and 300°C where the temperature dependence is weak again ≈ 0.3 MPa/°C.

3.3 - Interpretation of the simulation results

Figure 9 presents an analysis of the irradiation-induced defects produced in the steel at 55, 100, 200 and 350°C for a dose of 0.1 dpa. For all temperatures, the SIA loops have a very small contribution to the simulated hardening, since the number density of loops containing more than 19 SIAs is pretty low (in the current version of RPV-1, SIA loops containing less 19 SIAs are considered to have no hardening effect). It can also be noticed that :

-between about 50 and 100°C, the hardening is mainly controlled by the vacancy clusters. Indeed, their number density is much higher than those of the copper-rich precipitates and of the vacancy-solute clusters. The temperature effect in this temperature range seems to be associated with a decrease of the number density of vacancy clusters as the temperature increases.

-between about 100 and 250°C, the steel response is controlled by a sharp decrease of the number densities of vacancy clusters, copper-rich precipitates and vacancy-solute clusters.

-between about 250 and 300°C, the hardening is mainly controlled by the copper-rich precipitates and the vacancy-solute clusters. Indeed, their number densities are much higher than those of the vacancy clusters. The temperature effect in this temperature range seems to be mainly associated with a decrease of the number density of vacancy-solute clusters as the temperature increases.

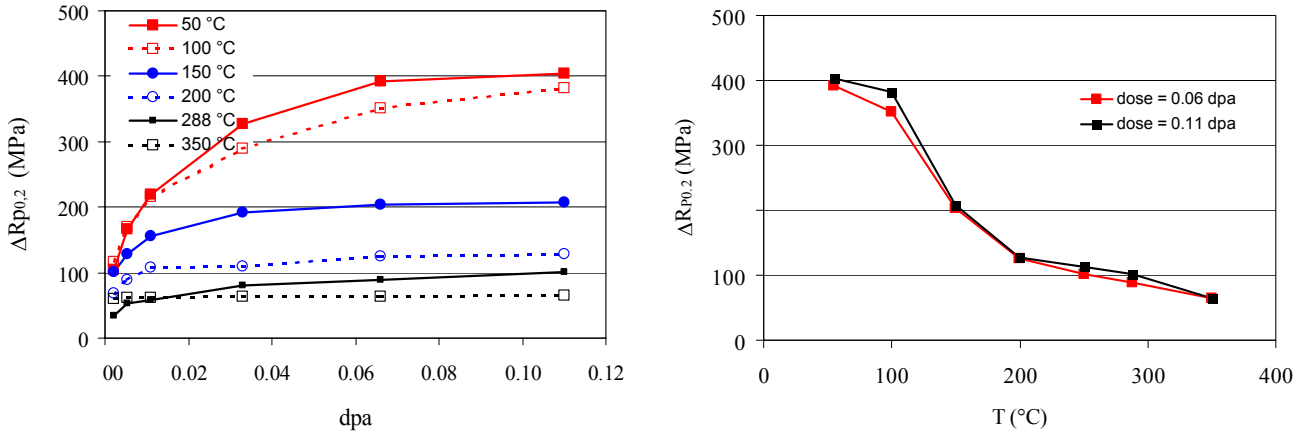

a) versus the dose

b) versus the temperature

Figure 8 : effect of the irradiation temperature on the irradiation-induced increase of yield stress ; simulation results obtained with the OSIRIS neutron spectrum (($\Phi_{E>1MeV}$ = 4.7 10^{12} $n.cm^{-2}.s^{-1}$), Cu = 0.065%, Mn = 1.3%Mn, Ni = 0.7%Ni)

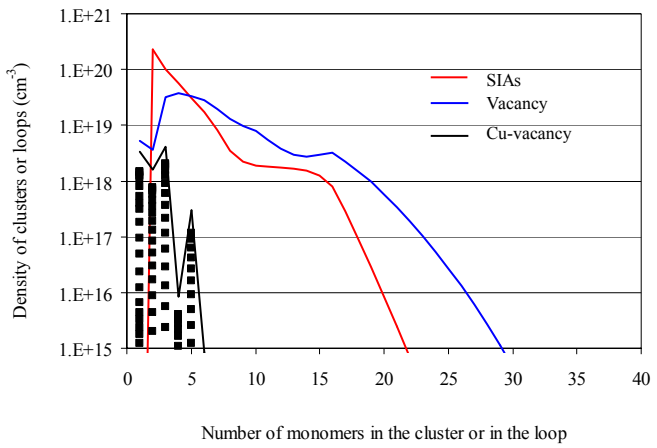

a) irradiation temperature : 55°C

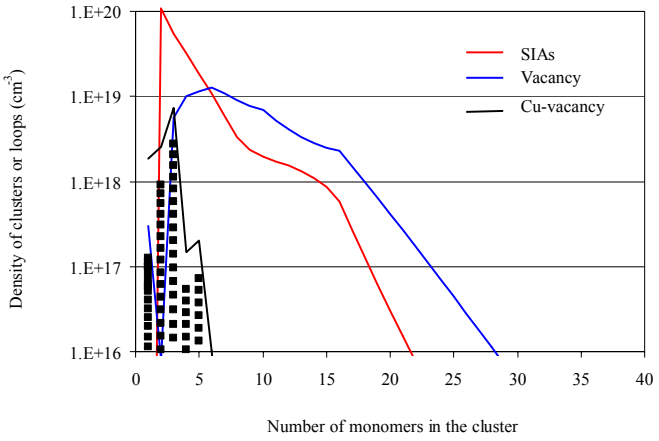

b) irradiation temperature : 100°C

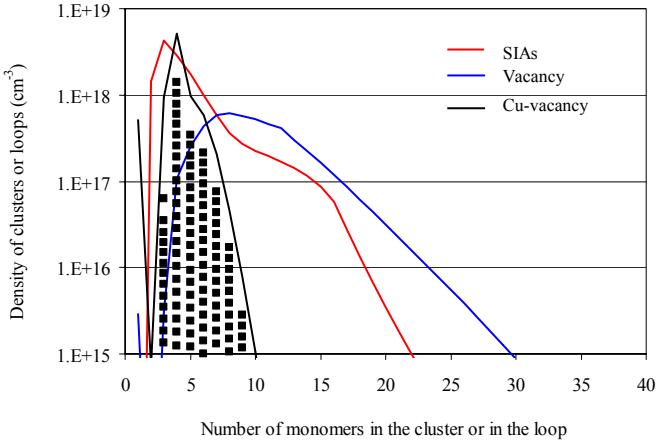

c) irradiation temperature : 200°C

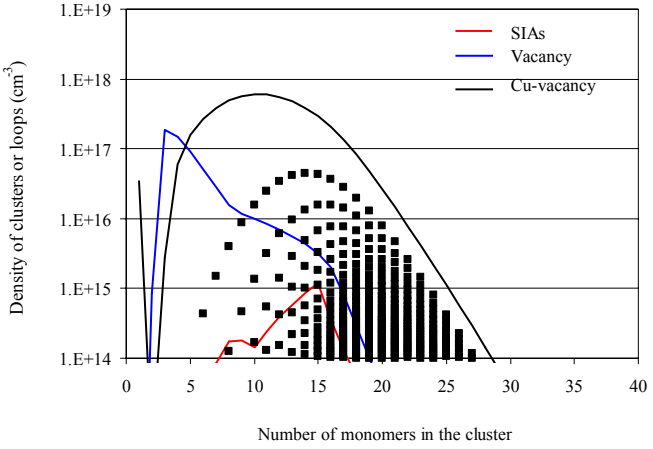

d) irradiation temperature : 350°C

Figure 9: effect of the irradiation temperature on the irradiation-induced increase of yield stress - distribution of hardening defects densities of defects for a dose of 0.1 dpa; simulations performed with the OSIRIS neutron spectrum (ϕ (E>1MeV) = 4.7 10^{12} n.cm^{-2}.s^{-1}), Cu = 0.065%, Mn = 1.3%Mn, Ni = 0.7%Ni. The copper-rich precipitates and the vacancy-solute clusters are described by their number of copper atoms.

IV - Conclusion

In the previous Chapters, the weaknesses and flaws of RPV-1 have been pointed out. Nevertheless, this Chapter demonstrated that RPV-1 can already be used to reinforce or complement experimental programs. For the two studied cases, RPV-1 reproduced the experimental results almost quantitatively and provided additional understanding through an analysis of the simulated irradiation-induced damage.

References

1 Tran Dai Phuc, "Influence du spectre de neutrons sur la Fragilisation des Aciers de Cuve de Réacteurs", Note CEA N. 2077, (Janvier 1979).

2 Serpan, C.Z., McElroy, W.N., "Radiation Damage in Materials", (Proc. Symp. Vienna, 1969), vol. 2, IAEA, Vienna, (1969), p.33

3 Steele, L.E., Hawthorne, J.R., ASTM-STP 286, (1961), p. 11.

4 Steele, L.E., Atomic Energy Review, vol. 7.2, (1969).

5 Pichon, C., Brillaud, C., Deylier, D., Alberman, A., Soulat, P., ASTM-STP 1366, (2000), P. 87 and Alberman, A., CEA Note technique n°95 123 - Affaire 2326, (1996).

6 Kinchin, G. H. Pease, R. S., Rep. Prog. Phys., vol. 18, (1955).

7 Lindhard, J., Nielsen, V., Scharff, M., Thomsem, P. V., Matematik-fysiske Meddedelser, Kongelige Danske Videnskabernes Selskab, vol. 33, n°10, (1963).

8 Nelson, R. S., Etheringthon, E. W., Smith, M. F. "Recommended Iron Atomic, Displacement Cross-Sections and Displacement Rates for Fast reactors", TRG. Report-2152 (D), (1972).

9 Norgett, M. J., Robinson, M. T., Torrens, I. M., "Une méthode de Calcul du Nombre de Déplacement Atomiques dans les Métaux Irradiés", CEA report CEA-R-4389, (1972).

10 Norgett, M. J., Robinson, M. T., Torrens, I. M., Nucl. Eng. Des., vol. 33, (1975), p. 50.

11 ASTM E693, "Standard Practice for Characterizing Neutron Exposures in Ferritics Steels in Terms of Displacements per Atom (dpa)", (1979, reapproved 1985).

12 Doran, D. G., Odette, G. R., Mansur, L. K., Simons, R. l., in "Radiation Effects in Breeder Reactor Structural Materials", Bleibert M. L. and Bennett J. W. eds, AIME, New York, (1977), p. 591.

13 Akamatsu-Jousset, M., "Evolution Structurale d'Alliages Ferritiques sous Irradiation", PhD thesis,, Université d'Orsay, (1994).

14 Alexander, D., E., Rehn, L. E., Farrell, K., Stoller, R.E., J. Nucl. Mater., vol. 228, (1996), p. 76.

15 Stoller, R.E., Farrell, K., Mansur, L.K., "The Effect of Thermal Neutrons and Fast Flux on Tensile Properties of Ferritic Steels Irradiated at Low Temperatures", ORNL Letter Report, ORNL/NRC/LTR-96/3, (1996).

16 Jones, R. B., Derek, J. E., Woottom, M. R.., ASTM-STP 1366, (2000), p. 366.

17 Mansur, L. K., Farrell, K., J. Nucl. Mater., vol. 170, (1990), p. 236.

18 Heinisch, H. L., J. Nucl. Mater., vol. 178, (1991), p. 19.

19 Rehn, L. E., Birtcher, R., C. J. Nucl. Mater., vol. 205, (1993), p. 31.

20 Alexander, D., E., Rehn, L., E., J. Nucl. Mater., vol. 209, (1994), p. 212.

21 Farrell, K., Mahmood, S. T., Stoller, R. E., Mansur, J. Nucl. Mater., vol. 210, (1994), p. 268.

22 Pichon, C., Soulat, P., Houssin B. et al., "Radiation embrittlement of EDF pressure vessels steel", Fontevraud III - Contribution of materials investigation to the resolution of problems encountered in PWR, Fontevraud, vol. 2, (1994), p. 616.

23 Pichon, C., Brillaud, C., Deydier, D., Alberman, A., Soulat, P., ASTM-STP 1366, (1999).

24 Meannay, O., Dussarte, D., Soulat, P., ASTM-STP 1046, (1990), p. 294.

25 Odette, G.R., Lucas, G.E., EPRI Report NP 6114, Electric Power Research Institute, (1989).

26 Houssin, B., "Réévaluation des Marges à la Rupture de Cuve. Prévisison de la Fragilisation par Irradiation des viroles et Soudures de Cuves Basée sur les Teneurs en Cu, P et Ni", Note d'étude Framatome, EEM DC 0328, (Novembre 1983).

27 Suzuki, M., Onizawa, K., Kizzaki, M., ASTM-STP 1270, (1996), p. 351.
28 Ahlf, J. Schmitt, F. J., J. Nucl. Mater., vol. 105, (1982), p. 48.

CONCLUSION

Many key components in commercial nuclear reactors are subject to neutron irradiation which modifies their mechanical properties. So far, the prediction of the in-service behavior and the lifetime of these components has required irradiations in so-called "Experimental Test Reactors". This predominantly empirical approach can now be supplemented by the development of physically-based computer tools to simulate irradiation effects numerically. Such tools are called Virtual Test Reactors (VTRs).

The presented work was aimed at building a first VTR to simulate irradiation effects in pressure vessel steels of nuclear reactor. It mainly consisted in :

- modeling the formation of the irradiation induced damage in such steels, as well as the their plasticity behavior;
- selecting codes and models to carry out the simulations of the involved mechanisms. Since the main focus was to build a first tool (rather than a perfect tool), it was decided to use, as much as possible, existing codes and models in spite of their imperfections.
- developing and parameterizing two missing codes: INCAS and DUPAIR.
- proposing an architecture to link the selected codes and models.
- constructing and validating the tool.

RPV-1 is made of five codes and two databases which are linked up so as to receive, treat and/or transmit data. A user friendly Python interface facilitates the running of the simulations and the visualization of the results.

RPV-1 relies on many simplifications and approximations and has to be considered as a prototype aimed at clearing the way. Long-term efforts will be required to complete it and to build successive generations of more and more sophisticated versions. Nevertheless, RPV-1 is sensitive to its input data (neutron spectrum, temperature,...) and provides results in conformity with experimental ones. According to the functionalities targeted for RPV-1, the main weakness is a bad Ni and Mn sensitivity. However, the tool can already be used for many applications (understanding of experimental results, assessment of effects of material and irradiation conditions,…).

This first step led 40 European organizations to start developing RPV-2 an advanced version of RPV-1, as well as INTERN-1, a VTR devised to simulate irradiation effects in stainless steels, in a large effort (the PERFECT project) supported by the European Commission in the framework of the 6th Framework Program.